

Freie Universität



Berlin

---

Im Fachbereich Physik der Freien Universität  
Berlin eingereichte Dissertation

---

Assessment of kesterite electronic and chemical  
surface properties

(Dr. rer. nat.)

---

Tetiana Olar

2017



Gutachter: Prof. Dr. Martha Ch. Lux-Steiner

Prof. Dr. Christina Roth

Tag der Disputation 09.05.2017



## Statement

I hereby declare that this submission is my own work and that, to the best of my knowledge and belief, it contains no material previously published or written by other person, except where due acknowledgment is made in the text. I also declare that the intellectual content of this thesis is the product of my own work, even though I may have received assistance from others on style, presentation and language expression.

## Erklärung

Hiermit versichere ich, dass ich diese Arbeit selbstständig verfasst und keine anderen als die angegebenen Hilfsmittel verwendet habe. Die Arbeit enthält, nach meinem besten Wissen und Gewissen, weder bereits von anderen Personen veröffentlichte Materialien noch wurden jegliche Teile dieser Arbeit bereits einer anderen Universität oder ähnlichen Bildungsstätte zur Erlangung eines Abschlusses oder Titels vorgelegt, außer entsprechendes Material ist als solches gekennzeichnet.

Berlin, 6. Februar 2017

---



# Acknowledgement

I would like to express my deep gratitude to Dr. Iver Lauermann, my research supervisor, for his patient guidance, enthusiastic discussions and useful critiques of my research. I would also like to express my thanks to Prof. Dr. M. Ch. Lux-Steiner and Prof. Dr. C. Roth for their support and leadership at the Free University of Berlin. A special thank you to all members of the CISSY group who have helped me perform countless experiments in the lab and at the synchrotron.

I would like to thank the KESTCELL team for the great experience I've received and for numerous interesting workshops, presentations and secondments I've participated in. The most enjoyable part of this research experience was working with the brilliant people involved in the project. Thank you all for that!

This work was funded by the Marie Curie Foundation and I am grateful to have been selected as the PhD student for this project.

I would like to express my thanks to my parents and sister, my friends all over the world for their endless encouragement and mental support throughout my studies. Thank you for always being by my side and providing continuous back up!



# Contents

I.	Zusammenfassung	11
II.	Abstract	12
III.	Abbreviation and symbols	13
1.	Introduction	15
2.	Kesterite material	17
2.1.	Bulk properties	17
2.2.	Chemical etchings and surface chemistry	19
2.3.	Fabrication process of the kesterite absorbers	20
2.4.	Electronic properties of chalcopyrites	21
2.5.	Summary of the chapter	23
3.	Heterojunction and solar cell basics	25
3.1.	p-n homojunction	25
3.1.1.	Band diagram	25
3.1.2.	the principles of the p-n-junction	26
3.2.	Heterojunction	28
3.2.1.	Anderson rule	29
3.2.2.	Common anion rule	30
3.3.	Solar cell basics	31
3.4.	Kesterite based devices	32
3.4.1.	Band line-up	33
3.5.	Summary of the chapter	35
4.	Experimental methods	37
4.1.	Photoelectron spectroscopies	37
4.1.1.	X-ray photoelectron spectroscopies	37
4.1.2.	The CISSY	38
4.1.3.	The work function	39
4.1.4.	Quantitative evaluation of the XPS data	40
4.1.5.	Ultraviolet photoelectron spectroscopy	41
4.1.6.	Analysis of the UPS spectra	42
4.2.	Synchrotron radiation at BESSY II	43
4.2.1.	NEXAFS	44
4.2.2.	NEXAFS spectra	45
4.3.	Theoretical methods for the conduction band evaluation	46
4.3.1.	Ab-initio calculations of the conduction band states using the <i>exciting</i> code	47
4.3.1.1.	First principle approach to the X-ray absorption	47
4.3.1.2.	Calculation of the band gap using GW approximation	48
4.3.2.	FDMNES package	49
4.3.2.1.	Applying the FDMNES to the X-ray absorption spectra	50
4.4.	Summary of the chapter	51
5.	Surface electronic and chemical properties of kesterite	53
5.1.	Samples with different $[S]/([S]+[Se])$ ratio	53
5.2.	Influence of etching on the surface chemical composition	56
5.2.1.	Surface vs bulk $[S]/([S]+[Se])$	56
5.2.2.	Cation surface composition	59
5.3.	Depth-dependent composition studied by high energy XPS	61
5.4.	Determination of valence band edges by UPS	62
5.4.1.	The valence band edge study by high energy synchrotron radiation	63
5.5.	Band line-up with CdS buffer layer	66
5.5.1.	Influence of the CdS deposition method	67

5.5.2.	Post deposition low temperature annealing of kesterite absorbers	69
5.6.	Summary of the chapter	74
6.	Conduction band edges of kesterite absorbers with different [S]/([S]+[Se]) ratios	77
6.1.	NEXAFS experiments of CZTS and CZTSe absorbers	77
6.1.1.	Off-stoichiometric kesterite powder samples	77
6.1.2.	NEXAFS spectra at BESSY II	78
6.1.3.	Fine structure of the Cu L <sub>3</sub> absorption edge	81
6.1.4.	Discussion of the NEXAFS spectra. Limitations of the method	83
6.1.5.	Tetragonal distortion and the atomic-scale properties	84
6.1.6.	Summary of the NEXAFS results	85
6.2.	Theoretical approaches for the conduction band assessment	85
6.2.1.1.	GW approximation calculations of the VBM and CBM relative positions	86
6.2.1.2.	Density of states in conduction band	86
6.2.1.3.	Local electronic properties of CZTS and CZTSe	87
6.2.2.	Summing up the results of ab-initio calculations	89
6.2.3.	FDMNES simulations of the kesterite absorption spectra	89
6.2.3.1.	Important computational parameters	89
6.2.3.2.	Simulated vs experimental spectra	91
6.2.3.3.	Determination of the shifts between the simulated spectra	93
6.2.3.4.	Summing up the results of FDMNES simulations	95
7.	Conclusions	97
8.	Outlook	101
9.	Author's contributions	103
10.	Appendix	105
a)	<i>exciting</i> code for the simulation of the electronic states in the CB. Using the GW approximation	105
b)	FDMNES package for absorption spectra simulations. The finite difference method	106
c)	Experimentally derived NEXAFS spectra	108
d)	Ab-initio calculation of kesterite crystal geometry	109
e)	pDOS of CZTS and CZTSe calculated using <i>exciting</i> code	110
11.	CV	111
12.	References	113

# Zusammenfassung

Kesterit-basierte Dünnschicht-Solarzellen mit der allgemeinen Zusammensetzung  $\text{Cu}_2\text{ZnSn}(\text{Se},\text{S})_4$  sind in den letzten Jahren Gegenstand intensiver Forschungs- und Entwicklungsarbeiten gewesen. Kesterit kann wegen der ungiftigen und in der Erdkruste häufig vorkommenden Bestandteile und einer vergleichbaren Bandlücke ein guter Ersatz für Chalkopyrit ( $\text{Cu}(\text{In},\text{Ga})(\text{Se},\text{S})_2$ ) sein. Beim Übergang von der reinen Sulfid- zur reinen Selenidzusammensetzung verändert sich die Kesteritbandlücke von 1.5 auf 1 eV. In dieser Arbeit wurden die folgenden Fragen untersucht: wie ändern sich die elektronischen und chemischen Oberflächeneigenschaften von Kesterit, wenn wir das  $[\text{S}]/([\text{S}]+[\text{Se}])$ -Verhältnis ändern? Wie ändert sich die Bandanpassung mit der Pufferschicht? Was sind die relativen Valenzband- und Leitungsbandpositionen, wenn man von CZTS zu CZTSe geht?

Um die elektronischen Eigenschaften von Kesterit zu untersuchen, wurden umfassende Analysen von Dünnschicht-Kesteritabsorbern unter Verwendung von oberflächensensitiven Techniken wie Röntgen-Photoelectronenspektroskopie (XPS) und Ultraviolett-Photoelektronenspektroskopie (UPS) sowie synchrotronbasierter Spektroskopie erfolgreich durchgeführt. Proben mit unterschiedlichen Konzentrationsverhältnissen von  $[\text{S}]/([\text{S}]+[\text{Se}])$  wurden vor und nach der Anwendung spezieller nasschemischer Ätzverfahren untersucht. Es wurden starke Abweichungen zwischen der chemischen Zusammensetzung von unbehandelten und geätzten Oberflächen beobachtet. Generell unterscheiden sich Oberflächen und Volumenzusammensetzung.

Die relativen Positionen der Valenzbandkante wurden mit UPS ausführlich untersucht. Die dabei mit der Laborquelle erzielten Ergebnisse konnten mit Messungen mit unterschiedlichen Anregungsenergien am Synchrotron bestätigt werden. Die experimentellen Ergebnisse stimmen gut mit theoretischen Werten zusammen, die in der Literatur verfügbar sind.

Die Änderungen in der Anionenzusammensetzung bewirken eine Verschiebung nicht nur im Valenzbandmaximum (VBM), sondern auch im Leitungsbandminimum (LBM). Dies wurde mit Röntgennahkanten-Absorptionsspektroskopie (NEXAFS) gezeigt. Eine Serie von Absorptionskanten wurde für CZTS- und CZTSe-Proben erhalten: Cu, Zn K- and L-Kanten und die Sn L-Kante. Die relativen Verschiebungen zwischen den Spektren wurden der Verschiebung im LBM zugeschrieben. Der Wert der Verschiebung war für alle Kanten innerhalb der Fehlergrenze gleich. Neben den polykristallinen Dünnschichtproben wurden einphasige Pulverproben als Referenzen verwendet.

Wir haben experimentelle Ergebnisse mit theoretischen Berechnungen korreliert und eine gute Übereinstimmung zwischen ihnen gefunden. Dichtefunktionaltheorie-Berechnungen der Leitungsbandzustände haben die in den Experimenten gesehene Tendenz bestätigt: Die relativen Positionen der unbesetzten-Zustände an der LB-Kante liegen in den Seleniden bei niedrigeren Energien als die des Schwefels. Unter Verwendung einer sogenannten GW-Annäherung wurden die Werte der Verschiebung von VBM und LBM erhalten. Sie stimmen innerhalb der Fehlergrenzen mit den experimentellen Ergebnissen überein. Die beobachteten Verschiebungen in den Absorptionsspektren und in den berechneten Zuständen wurden mit den Änderungen in der Kesteritkristallstruktur korreliert.

Mit dem Simulationspaket FDMNES konnten wir die NEXAFS-Kanten wiedergeben. Cu, Zn K- und L-Kanten und Sn L-Kante wurden berechnet. Alle wesentlichen Spektraleigenschaften wurden zusammen mit den Verschiebungen zwischen den Spektren gut nachgebildet.

Die erhaltenen Informationen wurden eingesetzt, um den Einfluss der Bandanpassung und der Grenzflächen auf die Solarzeleigenschaften zu erklären.

# Abstract

Kesterite-based thin-film solar cells are of great interest due to non-toxic, earth-abundant constituents. Kesterite can be a good substitute for chalcopyrite with a band gap in the same range of values. When going from pure sulfide to pure selenide composition, the band gap of kesterite is changing from 1.5 to 1 eV, respectively. Several questions arose for us: how do the electronic and chemical surface properties of kesterite change when we change the  $[S]/([S]+[Se])$  ratio? How does the band alignment change with a change in the buffer layer? What are the relative positions of conduction (CB) and valence band (VB) when going from CZTS to CZTSe?

A comprehensive study of the kesterite absorbers was done using surface-sensitive techniques such as X-ray Photoelectron Spectroscopy (XPS) and synchrotron-based spectroscopies, to investigate the chemical composition of kesterite surfaces. Samples with different  $[S]/([S]+[Se])$  ratios were examined before and after special etching procedures. A strong deviation of the relative chemical composition of the as-received and etched surfaces was observed. Surfaces also differ strongly from the bulk.

The detailed investigation of the relative positions of the valence band edge was done using Ultraviolet Photoelectron Spectroscopy (UPS). The results obtained with a laboratory source were confirmed using different excitation energies at the synchrotron. The well-reproduced shift value is in good agreement with theoretical values available in literature.

The changes in anion composition cause a shift not only in the VBM, but also in the CBM. We have proven that using X-ray absorption spectroscopy, namely its special case- NEXAFS. A large set of absorption edges were obtained for CZTS and CZTSe samples: Cu, Zn K- and L-edges, and the Sn L-edge. The relative shifts between the spectra of one type were attributed to the shift in CBM. The value of the shift was the same within the error margin for all measured edges of polycrystalline thin film samples. The value of the shift was confirmed by the powdered samples used as references, due to their well-defined composition and the single phase nature.

We have correlated experimental results with theoretical calculations and found a good agreement between them. Thus, the DFT calculations of the conduction band states have confirmed the trend seen in the experiments: the relative positions of the unoccupied states the CBM of selenides are shifted to lower energies compared to those of the sulfides. Using a so called GW approximation, the values of the shift of VBM and CBM were obtained, which overlap within the error with experimental findings. The observed shifts in the absorption spectra and in the calculated states have been correlated with the changes in the atomic-scale structure of the kesterite samples when substituting S atoms with bigger Se.

The simulation package FDMNES allowed us to reproduce the NEXAFS edges. Cu, Zn K- and L-edges and Sn L-edge were calculated and all essential spectral features were well reproduced together with the shifts between the CZTS- and CZTSe-related spectra. The values of the shifts between simulated spectra are in the same range as the experimental values.

The obtained knowledge was implemented to explain the influence of the surface and interface physics on the complete device performance.

# Abbreviation and symbols

<b>Abbreviation</b>	<b>Explanation</b>
CB	conduction band
CBO	conduction band offset
CBM	conduction band minimum
CIGS	Cu(In,Ga)S <sub>2</sub> , chalcopyrite
CIGSe	Cu(In,Ga)Se <sub>2</sub> , chalcopyrite
CZTS	Cu <sub>2</sub> ZnSnS <sub>4</sub> , kesterite
CZTSe	Cu <sub>2</sub> ZnSnSe <sub>4</sub> , kesterite
DFT	density functional theory
DOS	density of states
EBIC	electron beam induced current
EDX	energy-dispersive X-ray spectroscopy
$E_{\text{bin}}$	binding energy
$E_{\text{kin}}$	kinetic energy
$E_{\text{g}}$	band gap
EXAFS	extended X-ray absorption fine structure
FF	fill factor
FDMNES	simulation package name
GW	GW approximation
$h\nu$	excitation energy
HAXPES	hard X-ray photoelectron spectroscopy
HIKE	high energy photoelectron spectroscopy
IMFP	inelastic mean free path
IPES	inverse photoelectron spectroscopy
$I_0$	dark current
$I_L$	light generated current
$I_{\text{sc}}$	short circuit current
I-V curve	current-voltage curve
LDOS	local density of states
LAPW	linearized augmented plane waves
NEXAFS	near edge X-ray absorption fine structure
PV	photovoltaics
pDOS	partial density of states
$R_s$	series resistance
UV	ultraviolet
UPS	ultraviolet photoelectron spectroscopy
$V_{\text{bi}}$	built-in potential
$V_i$	bend bending
$V_{\text{oc}}$	open circuit voltage
VB	valence band
VBM	valence band maximum
VBO	valence band offset
XAS	X-ray absorption spectroscopy
XPS	X-ray photoelectron spectroscopy
$\Delta E_c$	conduction band offset
$\Delta E_v$	valence band offset
$\chi$	electron affinity
$\Phi$	work function
$\phi_s$	work function of spectrometer



# 1. Introduction

Photovoltaics devices (PV) are alternative sources of non-polluting renewable power. PV directly converts the sunlight into electrical energy and has been of great interest for scientists for many years. Historically the costs of the PV technologies have been relatively high in comparison to conventional power sources and their impact on the global energy sector has been relatively small. [5] The increasing concerns about the global warming and the understanding of the fact that current power sources are actually finite and polluting have encouraged changes. The PV technologies started to be developed rapidly and massively.

Nowadays, one of the newest PV market branches is the thin film solar cells composed of several functional layers with a thickness ranging from nm up to  $\mu\text{m}$ . [5] They have advantages compared to the crystalline silicon solar cells in several criteria. Due to their direct band gap, the absorption coefficient is much higher in thin film solar cells in comparison to the crystalline silicon. [5] Also, the amount of the used material is lower, which directly influences the production costs. The new popular materials for thin film PV application are chalcopyrite  $\text{Cu}(\text{In,Ga})\text{S}(\text{e})_2$  (CIGS(e)) and cadmium telluride CdTe materials.

This thesis focuses on a relatively new compound semiconductor suitable for the PV application. The kesterite material is a pentenary copper-zinc-tin-sulfur or/and selenium compound with the chemical formula  $\text{Cu}_2\text{ZnSnS}(\text{e})_4$  abbreviated to “CZTS(e)”. Kesterite is closely related to the commercially used CIGS(e) and was designed as a cheaper and non-toxic analogue for the thin-film solar cells absorbers. So far kesterite based solar cells have reached over 12% [1] efficiency, while chalcopyrites are already over 22%. [4] According to the Shockley-Queisser limit for the PV energy conversion, an efficiency over 30% can be achieved for solar cells based on an absorber material with a band gap in the range of 1.1-1.4 eV. [2], [3] The band gap energy of the kesterite compound can be tuned from 1 up to 1.5 eV depending on the  $[\text{S}]/([\text{S}]+[\text{Se}])$  anion compositional ratio, which is making it a promising material for the efficient solar cells usage. Despite the theoretical predictions, kesterite solar cells efficiencies and  $V_{\text{oc}}$  are nevertheless far below the theoretical limits. There are different reasons for such phenomena. It could be due to the segregation of secondary phases during the material growth [3], impurities or interface recombination.

This thesis is concerned with a study of the kesterite absorbers with different  $[\text{S}]/([\text{S}]+[\text{Se}])$  ratio using X-ray based spectroscopies. The surface sensitive techniques, such as XPS and UPS, allow studying the surface composition of the kesterite layer and the development of the electronic parameters with changes in the composition. Thus the kesterite samples ranging from pure sulphide to pure selenide composition were investigated in order to establish the relation between the anion composition and electronic properties of the absorber layer. The found dependence can be used for the future device tailoring, namely for the more accurate prediction of the band alignment between the kesterite layer and buffer layer, such as CdS, Zn(O,S) etc. The band offset at the absorber/buffer interface plays an important role for the final device performance and has a direct impact on the efficiency of the cell.

The work presented in this thesis was done within a European project “KESTCELLS” of the Marie Curie grand. The project had several objectives to gain. First, build an innovative network for the multidisciplinary training of young researches. [6] Secondly, the development of technologies for the efficient sustainable compatible kesterite based devices. For that purposes several research institutes,

universities and companies with a strong expertise in the advanced thin film PV field have been united in to a consortium, including Helmholtz Zentrum Berlin.

The scientific objectives of the project includes a deeper understanding of the fundamental properties of kesterite material, identifying the role of secondary phases in the device performance, obtaining knowledge about the main doping mechanisms in material in order to design kesterite baser solar cells with optimised characteristics and efficiency of more than 10%. Getting ahead, the objectives were fulfilled and results of the numerous studies were presented in papers and conferences. The 11.2% efficient solution processed kesterite solar cell with a low voltage deficit has been reported. [8]

## 2. Kesterite material

The main purpose of this chapter is to introduce the kesterite material – the semiconductor used for the absorber layer in thin film solar cells and studied throughout this work. Bulk properties as well as surface chemistry of kesterite will be discussed in this chapter. The preparation method of the studied samples is given in the last paragraph.

### 2.1. Bulk properties

$\text{Cu}_2\text{ZnSnS}_4$  (CZTS),  $\text{Cu}_2\text{ZnSnSe}_4$  (CZTSe) and  $\text{Cu}_2\text{ZnSn}(\text{S}_{1-x}\text{Se}_x)_4$   $0 \leq x \leq 1$  (CZTSSe) semiconductor compounds (Fig.2.1.), crystallize in the kesterite structure with space group  $I\bar{4}$ , which is a derivative of the chalcopyrite (CIGS) structure, which is itself a derivative of the zinc blende (or sphalerite) structure,  $(\text{Zn,Fe})\text{S}$ . However, there is evidence that CZTS tends to appear in the kesterite structure, while CZTSe is preferably found in the stannite structure. [9] Stannite (space group  $I\bar{4}2m$ ) differs from kesterite in the ordering of Cu and Zn cations (see Fig.2.1.).

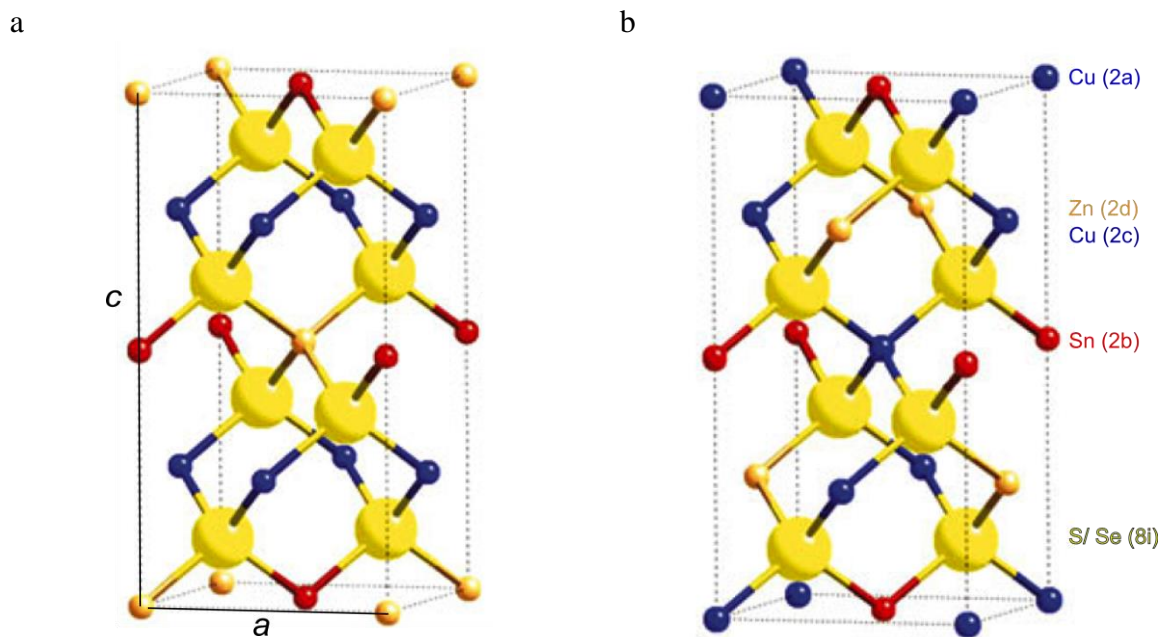


Fig.2.1. The stannite (a) and kesterite (b) type structure [10], where Cu atoms are shown in blue, red-Sn, orange-Zn, yellow-S or Se. (a) the crystal unit cell lattice parameters are indicated with  $a$  and  $c$  (see text)

Using neutron diffraction as a tool to distinguish Cu and Zn nuclei, a comprehensive study of powdered  $\text{Cu}_2\text{ZnSn}(\text{S}_{1-y}\text{Se}_y)_4$  ( $0 \leq y \leq 1$ ) samples has shown that both CZTS and CZTSe appear in the

kesterite structure, with some degree of disorder in Cu and Zn sites. [11] Recent theoretical calculations have provided the binding energies for the stannite and kesterite structures and it became clear that the kesterite is the more stable phase for both sulfide and selenide compounds. The energy difference between the two structures is quite small and probably the two phases coexist in the material. This can explain the fact that disorder in Cu and Zn sites is found experimentally. [11] Moreover, the stannite phase has a lower band gap than the kesterite phase – this can be one of the reasons for the lower than expected open circuit voltage in the kesterite-based solar cells in comparison with the band gap. [12], [13]

Another important structural parameter that governs the electronic structure of the material is the tetragonal distortion. [9] The tetragonal distortion is the deviation of the ratio  $c/2a=1$ , where  $c$  and  $a$  are the lengths of the edges of the crystal unit cell and called lattice parameters ( $a$  and  $c$  are shown schematically in Fig.2.1, a). Therefore if the ratio of the long length  $c$  over two times the short length  $a$  is not equal 1, a tetragonal distortion of the crystal occurs in the studied system. The experimental work done with powdered and a polycrystalline thin film CZTS samples has detected a tetragonal distortion which leads to strain in the bulk of the material. The ratio  $c/2a$  was found to be 1.0008, i.e. slightly above 1, for a CZTS powder samples using a combination of X-ray and neutron diffraction. [14] The dependence of the  $c/2a$  value on the cooling rate of the sample after the thermal annealing was detected. The slowest cooling rate is expected to provide the most stoichiometric sample. All single crystal samples have revealed a value  $c/2a>1$ : at a cooling rate of 1 K/h the ratio  $c/2a\sim 1.0015$ ; 10 K/h -  $c/2a\sim 1.0017$ . Thin film CZTS samples were studied as well and the  $c/2a$  ratio was found to be lower than 1. These results can be attributed to the fact, that thin film polycrystalline samples can contain secondary phases and are in general less stoichiometric than powder samples. A similar picture is observed for the selenide kesterite. [9] The tetragonal distortion is a powerful marker of the crystal quality of the differently prepared kesterite samples, that can be obtained experimentally, and can indirectly indicate the presence of secondary phases in kesterite absorbers, both sulfide and selenide.

Kesterite has a direct band gap and its value varies depending on anion composition. The band gap value can be experimentally derived from optical transmission or by measurements of the spectral quantum efficiency of solar cells. A wide range of experiments has shown that the band gap of  $\text{Cu}_2\text{ZnSnS}_4$  is  $1.5 \pm 0.01 \text{ eV}$  [15][15]. But for a long time no agreement was found for the selenide compound, until Ahn et al. [16] have shown experimentally why often the band gap of CZTSe is over estimated. According to them the presence of ZnSe secondary phases causes the discrepancy in the transmission measurements and the band gap of  $\text{Cu}_2\text{ZnSnSe}_4$  is  $1 \pm 0.01 \text{ eV}$ . Recent theoretical calculations based on density functional theory [17], hybrid functional [18] and GW calculations [19] have shown a good agreement with experimental data. Within the estimated error, the theoretical band gap value of  $\text{Cu}_2\text{ZnSnSe}_4$  in the kesterite crystal structure is comparable with experimentally derived values, a deviation of around 100 meV is found for the stannite structure.

Defects in the crystal structure of the semiconductor play an important role for its optical and electronic properties. They control the doping and the recombination rate in solar cells. The intrinsic point defects are differentiated into vacancies of Cu, Zn, Sn, S or Se building atoms, i.e. when the crystal site which would be occupied in a perfect crystal is vacant in the real system. They are named  $V_{\text{Cu}}$ ,  $V_{\text{Zn}}$ ,  $V_{\text{Sn}}$ ,  $V_{\text{S}}$  or  $V_{\text{Se}}$  respectively. Secondly, the interstitials ( $\text{Cu}_i$ ,  $\text{Zn}_i$ ,  $\text{Sn}_i$ ,  $\text{S}_i$ ,  $\text{Se}_i$ ) - the defects of crystal structure when an atom occupies a site where no atom should be; and lastly, the antisite defects  $A_B$  when element B is replaced with element A ( $\text{Cu}_{\text{Zn}}$ ,  $\text{Zn}_{\text{Cu}}$ ,  $\text{Zn}_{\text{Sn}}$ ,  $\text{Sn}_{\text{Zn}}$  etc.). And in addition antisite defects can form defect clusters which are electroneutral. Theoretical calculations of the stoichiometric kesterite have shown that the most energetically favorable defect clusters are  $[\text{Cu}_{\text{Zn}}+\text{Zn}_{\text{Cu}}]$ ,  $[\text{V}_{\text{Cu}}+\text{Zn}_{\text{Cu}}]$ ,

[ $2Zn_{Cu}+Zn_{Sn}$ ], and [ $2Cu+Sn_{Zn}$ ]. [20] Due to their low formation energy they are assigned as intrinsic defects and govern the p-doping of the semiconductor. [20], [21] However, most kesterite absorbers are grown under Cu-poor, Zn-rich conditions and therefore the  $Zn_{Cu}$  point defect is highly expected, which is an n-type defect. The formation of [ $Cu_{Zn}+Zn_{Cu}$ ] clusters can be a reason for the lower  $V_{OC}$  in kesterite-based solar cells compared to chalcopyrites with a similar band gap. [20] The comprehensive experimental study is of high importance. On the whole, it becomes clear that the kesterite, alike CIGS, exhibits p-type conductivity in the range of  $10^0-10^{-1}\Omega cm$  [13] due to the  $Cu_{Zn}$  or  $Cu_{Sn}$  antisite defects and Cu vacancies with compensation from the  $Zn_{Cu}$  antisite and S vacancies. [9]

Kesterite is a complex pentenary system, which is hard to obtain as single phase. The variety of possible point defects and secondary phases makes this task very challenging. The experimentally derived phase diagram of the kesterite predicts only a narrow single phase region with 1-2% deviation in composition at the growth temperature  $550^\circ C$ . [22] For comparison, the chalcopyrite existence region allows 4% deviation in the Cu content. [23] The theoretical equilibrium calculations confirm experimental findings that the existence area of the single phase of kesterite is narrower than for chalcopyrites. [21],[9] Moreover, high performing kesterite devices are grown with Cu-poor, Zn-rich composition, which are very favorable conditions for the  $Zn(S,Se)$  secondary phase formation.  $Zn(S,Se)$  has already been found in kesterite thin film cells. [12] It has a wider band gap and low conductivity and therefore it will not harm the open-circuit voltage of the solar cell. But it can be responsible for the observed high series resistance. [12]

Other secondary phases such as  $Cu-(S,Se)$  and  $Cu-Sn-(S,Se)$  have a stronger detrimental effect on kesterite solar cell performance due to their lower band gap:  $E_g(Cu_2S)=1.2 eV$ ,  $E_g(Cu_2SnS_3)=1.0 eV$ ,  $E_g(Cu_2SnSe_3)=0.8 eV$ . The secondary phases with lower band gap, then the kesterite phase, will limit the  $V_{oc}$  of corresponding solar cells. Secondary phase segregations with a band gap lower by only 100 meV compared to the kesterite cause an 8 % drop in efficiency of the complete cell. [24]

Secondary phases with higher band gap, such as  $ZnS$  ( $E_g=3.7 eV$ ),  $ZnSe$  ( $E_g=2.7 eV$ ), are less detrimental; however, there is evidence that they can block the carrier transport [25]: using electron beam induced current (EBIC) and microscopic IV characterization, it was shown that the areas with high  $ZnSe$  secondary phase segregations on the surface of a kesterite absorber have low EBIC response. These areas exhibit a current blocking behavior and can reduce the short-circuit current density for the complete devices. In contrast, kesterite surfaces without  $ZnSe$  secondary phases have a high EBIC signal and result in high-efficient devices.

Another negative effect of the high band gap secondary phases is the increase in the series resistance  $R_s$  [26]. Secondary ion mass spectroscopy measurements were used to gain more information about the physical nature of different device parameters, such as  $R_s$ . CZTS and CZTSSe based heterojunction samples were studied and the obtained results suggest that the presence of  $ZnS$  or/and  $ZnSe$  secondary phases is responsible for the high  $R_s$ .

## 2.2. Chemical etchings and surface chemistry

The presence of secondary phases at the interface of the absorber/buffer reduces the junction quality and consequently the device performance. Therefore, efficient etching of the secondary phases from the surface is very important for the solar cell tailoring. We followed three different procedures from

IREC (see quoted references for details and implications on solar cell performance), which depend on the sample composition:

- CZTS and S-rich CZTSSe: HCl + (NH<sub>4</sub>)<sub>2</sub>S. HCl removes ZnS secondary phases and (NH<sub>4</sub>)<sub>2</sub>S removes Sn<sub>x</sub>(Se,S) [27], [28]
- Se-rich CZTSSe: (NH<sub>4</sub>)<sub>2</sub>S (as above)
- CZTSe: KMnO<sub>4</sub>/H<sub>2</sub>SO<sub>4</sub> followed by a Na<sub>2</sub>S-solution. The first step oxidises ZnSe secondary phases while the Na<sub>2</sub>S-solution removes resulting elemental selenium in the second step. [29]

It was shown in [27] that, due to Zn-rich growth conditions, of the kesterite absorber layer, which results in highly efficient cells, the ZnS secondary phase accumulates on the surface of CZTS and can be removed by an HCl etching solution. This is not a closed overlayer of ZnS, but rather island-like growth of different thicknesses. The efficiency of the cell grows considerably after etching: from 2.7% to 5.2%. In CZTSe, ZnSe is the most frequently found secondary phase and it was successfully removed with a two-step procedure, first with potassium permanganate, and then sodium sulfide. [29]

One of the main challenges is to define the chemical surface composition of the etched absorber. The effect of such a complex treatment of the surface of the semiconductor can be studied with different approaches and techniques. For instance, this question can be answered with the help of photoelectron spectroscopy (XPS). This is a very surface sensitive tool that provides the surface concentrations of the main components, which can be compared with their bulk concentrations before and after applying a specific etching procedure. Therefore one can directly obtain the relative surface composition of any of the thin film solar cell layers under as-received (i.e. prior to any treatment), etched or after air-exposed conditions.

## 2.3. Fabrication process of the kesterite absorbers

Kesterite thin films can be deposited using different techniques: electron beam evaporation, sputtering, pulsed laser deposition, electroplating, and printing of nanoparticles. One of the most successful methods for the chalcopyrite was a co-evaporation of all elements on the heated substrate, which provided the best solar cell. [30] However, this technique didn't work as that well for the kesterite. The highest efficiency kesterite devices were produced by hydrazine solution processing (12.6%). [1]

Samples studied in this work were produced using sputter deposition and subsequent selenisation/sulfurisation. This is a physical vapor deposition method where energetic particles (typically argon ions) bombard a precursor target to remove material from it and deposit the vapor phase onto the substrate. The target material can be metallic or non-metallic. Sputtering is an attractive technique for industry because of good step coverage and process control.

The absorbers used in this work were produced in the Catalonia Institute for Energy Research-IREC- using sequentially sputtered metallic precursor stacks with metal ratios of [Cu]/([Zn]+[Sn])=0.80, [Zn]/[Sn]=1.20 on the Mo-coated soda-lime glass substrates.

The sputtered metallic precursor is "chalcogenised" and crystallized in order to form the desired kesterite compound. Therefore the preparation of the stacked layers was followed by reactive thermal annealing in a tubular furnace in a graphite box in the presence of solid S and/or Se and Sn. [31], [32] As a result of different amounts of S and Se in the furnace, the entire range of the [S]/([S]+[Se]) ratios

between a pure sulfide and a pure selenide in the product is covered. The sample numbers and their composition are shown in Table 2.3. It is necessary to optimize the annealing temperature. High temperatures improve the crystallinity of the thin film, but increase the loss of certain elements and seriously affect the final composition and properties.

*Table 2.3. Kesterite samples with different  $[S]/([S]+[Se])$  ratios. The number of the sample will be used throughout this thesis. The precursor cation composition is identical for all samples*

Number	Precursor		Absorber comp. by EDX			Etching
	Cu/(Zn+Sn)	Zn/Sn	Cu/(Zn+Sn)	Zn/Sn	S/(S+Se)	
1	0.8	1.2	0.84	1.18	1	HCl+(NH <sub>4</sub> ) <sub>2</sub> S
2			0.87	1.22	0.95	HCl+(NH <sub>4</sub> ) <sub>2</sub> S
3			0.87	1.27	0.64	HCl+(NH <sub>4</sub> ) <sub>2</sub> S
4			0.89	1.32	0.49	(NH <sub>4</sub> ) <sub>2</sub> S
5			0.85	1.17	0.24	(NH <sub>4</sub> ) <sub>2</sub> S
6			0.82	1.16	0.06	(NH <sub>4</sub> ) <sub>2</sub> S
7			0.81	1.09	0	KMnO <sub>4</sub> /H <sub>2</sub> SO <sub>4</sub> +Na <sub>2</sub> S

The kesterite phase is not the only phase that can form in the Cu-Zn-Sn-S(Se) material system. [22] Taking into account the discussion of the sections 2.1 and 2.2 about the bulk and surface properties of the kesterite phase and the detrimental effect of its most common secondary phases on the final device performance, it would be important to add, that the formation of the secondary phases became especially a big challenge when the absorber was grown under nonstoichiometric conditions. The phase stability region of kesterite is much narrower than for CIGSe, which increases the chances of secondary phase formation. The most expected secondary phase in case of Cu-poor and Zn-rich conditions for the Cu-Zn-Sn-S system is the ZnS compound. [21], [33] A similar phase behavior is expected for the Cu-Zn-Sn-Se system, and the picture seems to be more complicated for the Cu-Zn-Sn-S-Se pentenary system. The studies suggest that sulfur-containing binaries would form preferentially over selenium containing binaries because of lower free energy of formation. [34] The presence of secondary phases is generally undesirable and can lead to the reduction of the solar cell performance. Lower band gap phases, such as Cu<sub>2</sub>SnS(Se)<sub>3</sub> [35] can limit the open circuit voltage of the cell, the high resistive ZnS(Se) [27], [29] or conductive Cu<sub>x</sub>S(Se) can be detrimental for the cell as well. The presence of these secondary phases causes a challenge for the growth of the kesterite absorber under the Cu-poor, Zn-rich conditions, which provide the most efficient devices. Different strategies are used to minimize the impact of secondary phases on solar cell. One of the methods of removing unwanted secondary phases from the surface of the kesterite absorber layer is a wet chemical etching, studied in detail in this work. [27], [29]

## 2.4. Electronic properties of chalcopyrites

In order to better understand the electronic properties of kesterite, the chalcopyrite material as a first nearest “relative” will be discussed in perspective of how the local microscopic structures govern macroscopic electronic properties.

The electronic properties of the chalcopyrites with different cation composition were studied in details. [111], [123] B. Johnson et al. [73] have examined thin film absorbers  $\text{CuIn}_x\text{Ga}_{1-x}\text{S}_2$  with  $x=0, 0.7,$  and  $1,$  using NEXAFS at Cu, Ga and S K- and  $L_3$  and In  $L_{3-}$  and  $M_{4,5}$  edges. Here, the changes in the cation composition of the samples also cause changes in the chalcopyrite electronic properties. It is known that the band gap of the semiconductor varies from  $1.5 \text{ eV}$  for  $\text{CuInS}_2$  to  $2.4 \text{ eV}$  for  $\text{CuGaS}_2$  and the difference of  $0.9 \text{ eV}$  is mainly caused by a shift of the CBM. Thus, shifts in the measured X-ray absorption edges are expected.

Surprisingly, only S related absorption edges revealed a corresponding shift when going from CIS to CGS. No change was observed in the position of the Cu, Ga K- and  $L_3,$  In  $L_3$  and  $M_{4,5}$  edges.

To study in detail the origin of the shifts seen in the S K- and  $L_3$  edges and the absence of those in the cation-related edges, DFT calculations of the electronic states of  $\text{CuIn}_x\text{Ga}_{1-x}\text{S}_2$  with  $x=0, 0.7$  and  $1$  were done. Following the dipole transition rules, the pDOS of sulfur, copper, gallium and indium were calculated. It was shown by Sarmiento-Rérez et al [111] that S  $p$  states shift with changes of the cation composition, while in the position of Ga  $p$  states no changes were predicted. A similar full agreement of the experimental results with DFT calculations is observed for all other measured absorption edges and respectively calculated pDOS. Therefore, the DFT approach had confirmed that pDOS of sulfur change when going from  $\text{CuInS}_2$  to  $\text{CuGaS}_2,$  while in contrast all corresponding pDOS of cations, i.e. Cu, In and/or Ga revealed no shift.

The unexpected NEXAFS observations, supported with DFT results, were explained after a detailed investigation of the *local* electronic properties and related crystal structure (Fig.2.2) of the chalcopyrites.

After a closer look at the crystal structure of chalcopyrite, it became clear that each sulfur atom surrounded with four cations, and contrariwise, each cation is surrounded with four sulfur atoms. In the described above experiment, when going from CIS to CGS, the nearest neighbors of S will change drastically, which is not the case for cations. The cations first neighbors remain unchanged - four sulfur atoms. I.e. in other words, the substitution of the indium atoms with gallium will cause a strong modifications of the chemical environment of the sulfur atoms, whereas the first nearest neighbors of Cu, In and/or Ga will remain the same, because there was no change in the anion material composition.

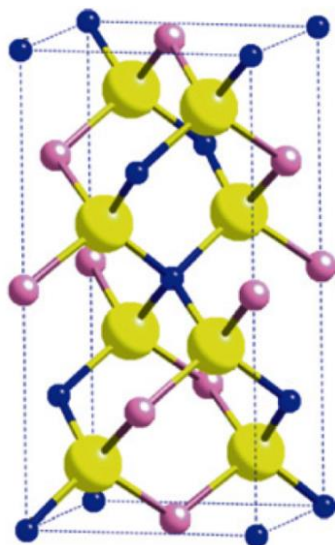


Fig.2.2. The crystal structure of chalcopyrite. Blue- Cu, yellow- S, purple- In or Ga atoms.

It was shown for chalcopyrites using extended X-ray absorption fine structure spectroscopy (EXAFS) that element-specific bond lengths remain nearly *constant* over the whole range of Cu(In,Ga)S<sub>2</sub> and Cu(In,Ga)Se<sub>2</sub> thin film absorbers with different In and Ga contents, ranging from CIS(e) to CGS(e) compositions. [123],[124] Similar observations are valid for the selenide containing Cu(In,Ga)Se<sub>2</sub> samples. [73] In addition, experimental results were confirmed by the simulations that had shown that the element-specific bond lengths deviate *slightly* when the *cation* composition of the material is changing.

The element specific bond lengths, obtained from the real absorption experiment, are shown in Table 2.4. Indeed, the deviation of the bond length, when the cation composition is varying, is small. The samples were measured using EXAFS at 17 K and Cu, Ga, and In K-edges were obtained. [123] The deviation of the  $d_{Cu-S}$  bond length is around  $\Delta \sim 0,01 \text{ \AA}$ , for  $d_{Ga-S}$   $\Delta \sim 0,01 \text{ \AA}$  and finally for  $d_{In-S}$   $\Delta \sim 0,007 \text{ \AA}$ .

Table 2.4. The element-specific bond lengths measured for chalcopyrite samples with different cation composition defined by the In/(In+Ga) ratio.

Sample	In/(In+Ga)	$d_{Cu-S}$ ( $\text{\AA}$ )	$d_{Ga-S}$ ( $\text{\AA}$ )	$d_{In-S}$ ( $\text{\AA}$ )
CuInS <sub>2</sub>	1.00	2.325	-	2.463
Cu(In,Ga)S <sub>2</sub>	0.64	2.323	2.297	2.456
CuGaS <sub>2</sub>	0.00	2.312	2.286	-

Now, having the information about the bond lengths in the chalcopyrite crystal structure, the results of the Johnson et al. [73] NEXAFS experiment can be explained. The unexpected behavior of the absorption edges and calculated pDOS were validated after a closer look into the atomic scale structure of Cu(In,Ga)S<sub>2</sub>.

## 2.5. Summary of the chapter

In this chapter the electronic and chemical properties of kesterite were introduced. The fundamental bulk properties, such as crystal structure and intrinsic point defects were discussed. The kesterite samples studied in this work were prepared by project partner IREC, via a sequential sputtering process followed by the selenization/sulfurization of the metal precursor. In order to remove unwanted secondary phases from the surface different chemical procedures were used, which were investigated in detail in this work. Finally, a short overview of the chemical and electronic properties of chalcopyrite is given in order to better understand the properties of kesterite. Similarities and differences between these two materials will be discussed later in chapter 6.



## 3. Heterojunction and solar cell basics

In this chapter the physical principles of the p-n homo- and heterojunctions will be presented for the better understanding of the solar cell device performance. A short overview of the p-n-junction formation, carrier transport across the interface and derived band diagram will be discussed. The second part of the chapter is devoted to kesterite-based solar cells, as the main object of the study in this work.

### 3.1. p-n-homojunction

In order to better understand the principles of the solar cell performance, we would like to start with the description of the p-n homojunction.

A p-n homojunction is formed when two differently doped pieces of the same material are in contact, i.e. it is an interface between a *p-type* and *n-type* semiconductor of the same material. The p-type semiconductor contains an excess of holes and the n-side has an excess of electrons, thus “p” stands for “positive” and “n” for “negative”. [36]

#### 3.1.1. Band diagram

First, we discuss the p-n-junction in equilibrium. In equilibrium there is no current flow and the Fermi level is flat. In the separate semiconductors, the Fermi level lies below the intrinsic level for the p-type material and above for the n-type (Fig. 3.1.a). As two parts of the junction are put in contact, the charge carriers start to move across the junction to equilibrate the Fermi level (Fig.3.1.b). As electrons from the n-type move to the p-type material, the Fermi level also moves away from the conduction band. Similarly in the p-type part of the junction, where  $E_F$  moves away from the valence band. Thus a new equilibrium position of the Fermi level is established.

It is worth noting that the Fermi level remains unchanged in the bulk of each material, far enough from the junction, because the doping level of the semiconductors is still the same.

The band diagram of the formed p-n-junction has been drawn following several rules:

- the Fermi level should be flat across the whole junction,
- far from the junction, the bulk properties of the semiconductors are valid,
- the energy bands are continuous across the junction. [37]

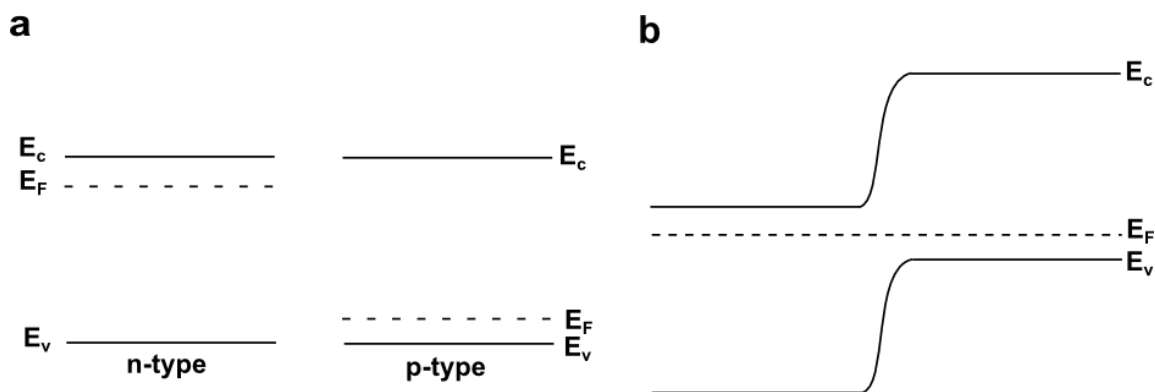


Fig.3.1.The formation of the band diagram in a homojunction. a: the p- and n-type semiconductor are apart, b: in contact.

The energy bands bend as they go through the charge separation region, since the relative position of the band with respect to the Fermi level changes. When we talk about the bend bending no spatial (physical) bending occurs, rather a local offset of the energy band is changing due to the space charge region effect. [38] The Poisson equation for the charge carriers in the depletion region brings the curvature to the bands because of the imbalance in the charge neutrality at the junction interface where differently doped materials meet each other.

### 3.1.2. The principles of the p-n-junction

The p-n junction is a building element for most electronic semiconductor devices, due to its rectifying properties: a p-n junction allows the current flow only in one and not in the opposite direction. Therefore a voltage applied to a junction is differentiated into forward bias- the easy current flow direction, and reverse bias- the direction of small or no current flow.

#### Zero bias

Without an external voltage applied, an equilibrium at the junction is reached, so that the potential difference across the junction is formed and called the *built-in potential*  $V_{bi}$ .

As the junction is formed, the electrons from the n-type material will follow the gradient in the electrochemical potential and move into the p-type part in the vicinity of the interface and recombine with the holes. Similarly, the holes from the p-type part of the junction tend to move into the n-type region, leaving behind the negatively charged ions in the p-type semiconductor and recombine with electrons in the n-type region. Thus, the region near the interface is depleted with charge carriers and a new equilibrium is reached. This region at the junction interface is called *space charge region* or *depletion layer*.

The electric field  $\epsilon$  in the charge separation region is directed opposite to the diffusion process of electrons and hole. Thus at the interface two competing phenomena happen (Fig.3.2): the flow of electrons and holes that generates even bigger depletion layer, and the electric field  $\epsilon$  made by this depletion region that counter-acts the charge carriers flow. [36]

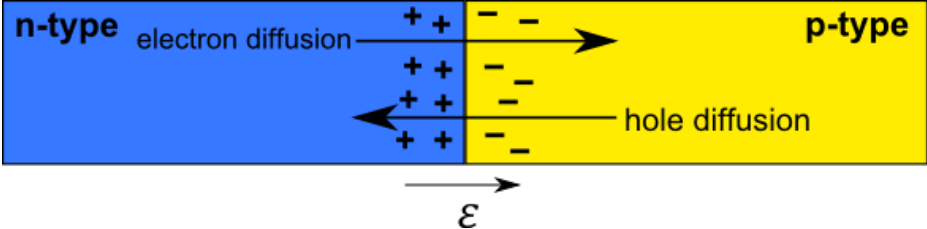


Fig.3.2. A p–n junction in thermal equilibrium with zero-bias voltage applied.

**Reverse bias**

In reverse bias a positive voltage is applied to the n-type material and a negative-voltage to p-type. Thus the positive voltage in the n-type material pushes electrons away from the junction interface, while the holes in the p-type material are attracted away from the junction towards the negative electrode. [39] Thus the depletion region becomes wider because of the lack of electrons and holes at the interface (Fig.3.3.a). The presence of the high impedance path for the charge carriers will turn the semiconductor junction almost in an insulator. A high potential barrier is built up, thus only a small current flows through the junction which is called a leakage current and which is often on the order of micro-amperes. [39]

If the applied reverse bias is increased, its value can reach a sufficiently-high enough value at the junction to cause a failure due to overheating of the junction and the occurrence of an avalanche effect around the junction. The diode will be shortened and this leads to a flow of a large current. In Fig 3.3.b this break-through is represented as the step down slope on the current-voltage characteristics of p-n-junction. The current-voltage characteristics or the I-V curve is the relationship between the electric current flowing through the diode and the corresponding voltage applied to it. [40] Normally it is shown as a graph, similarly to the one shown in Fig. 3.3.b.

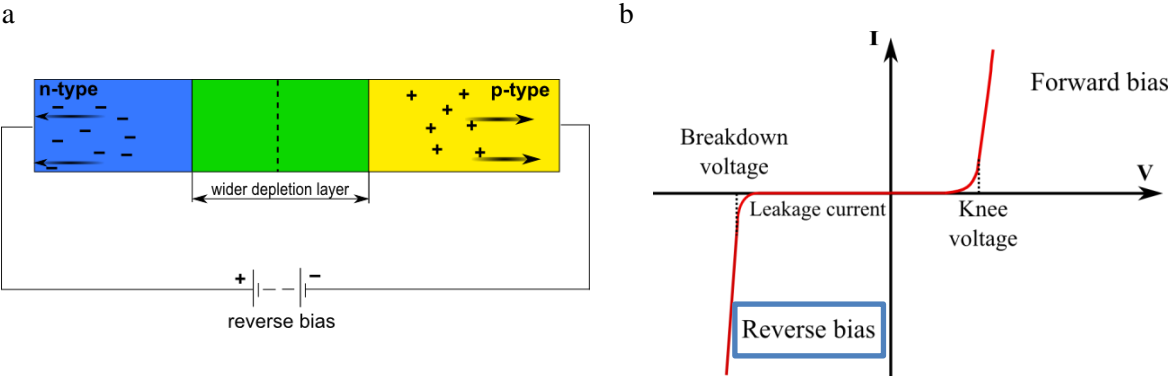


Fig. 3.3.a: The n-p-junction in reverse bias, b: the IV characteristics curve in reverse bias.

## Forward bias

When a current source is connected to the junction in forward bias, the p-type region of the junction is connected with the positive terminal and the n-type with the negative terminal, then the holes from p-type end and electrons from n-type part are driven towards the interface so that the depletion region will be reduced via the neutralization. The positive voltage is applied to the p-type region and repels the holes, and similarly, the negative voltage applied to n-type semiconductor repels electrons. [36] As the applied voltage grows, the depletion layer narrows and the potential barrier is overcome, the current starts to flow through the junction. This is due to the fact that the applied forward bias gives electrons enough energy to overpass the barrier, as well for holes that are repelled toward the junction too. The characteristic voltage showing the point of the potential barriers to be overcome is called “knee voltage” (Fig.2.4 a). Up to this voltage value no current is flowing.

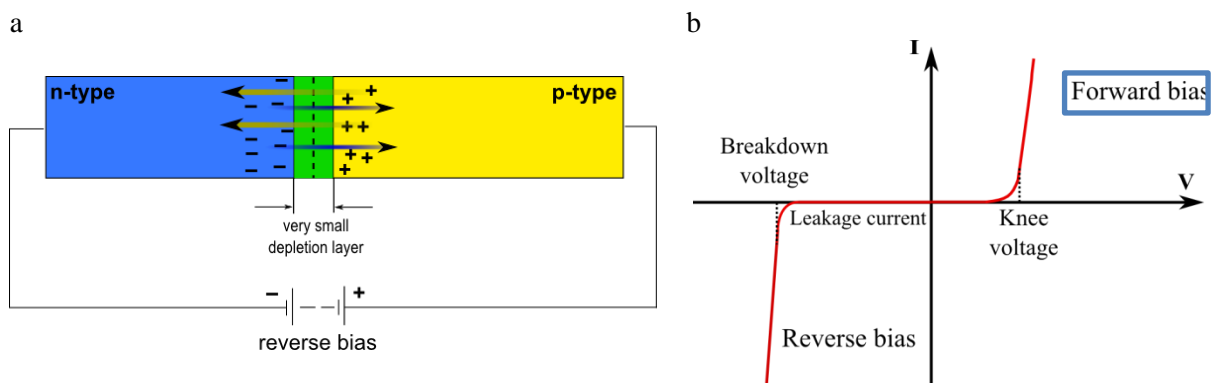


Fig.3.4 a: the p-n-junction in forward bias. The reduction of the depletion layer is shown, b: the I-V characteristics of the diode under forward bias applied.

In forward bias, the low resistance path through the junction because of the decreased depletion layer thickness allows a flow of a strong current with a relatively low applied voltage (Fig.3.4 b). After the knee point, the diode can conduct in principle an infinite current. In order to limit a current flow, a resistor in series is connected to the diode. The presence of a resistor prevents the diode device from overheating and eventual failure. [39]

## 3.2. Heterojunction

The p-n heterojunction follows the same physical principles as the homojunction. The main difference is that the constituent parts of the junction are different semiconductor materials. The heterojunction can be made via a metallurgical joint of p- and n-type semiconductors, so that the electrical contact is made and thus allowing a diffusion of electrons from n- to p-semiconductor and holes from p to n, respectively. To construct the band alignment for the heterojunction, a similar procedure as for the

homojunction is followed, i.e. the two materials are considered first apart and then in equilibrium as soon as junction is formed and the Fermi level is aligned. Taking into account that the material with a n-type doping has a wider band gap  $E_g^1$  than that with p-type doping  $E_g^2$ , and both materials also have different electron affinities ( $X_1, X_2$ ) and work functions ( $\Phi_1, \Phi_2$ ) the band alignment at the junction can be constructed (Fig. 3.5).

As far as materials have a different band gaps, a discontinuity of the conduction  $\Delta E_c$  and the valence bands  $\Delta E_v$  exist together with the respective amount of band bending  $V_1$  and  $V_2$ . [6]  $E_{g,eff}$  is the effective band gap seen by the charge carriers. The difference in the band gaps of two materials is equal to the sum of the conduction and valence band discontinuities [41]:

$$\Delta E_g = E_{g1} - E_{g2} = \Delta E_c + \Delta E_v \quad (3.1.)$$

Interestingly, the difference in the materials electron affinity equals the conduction band discontinuity. The so called electron affinity rule (or Anderson rule) predicts accurately the band diagram at the heterojunction only for limited amount of materials and will be discussed in detail in the following section.

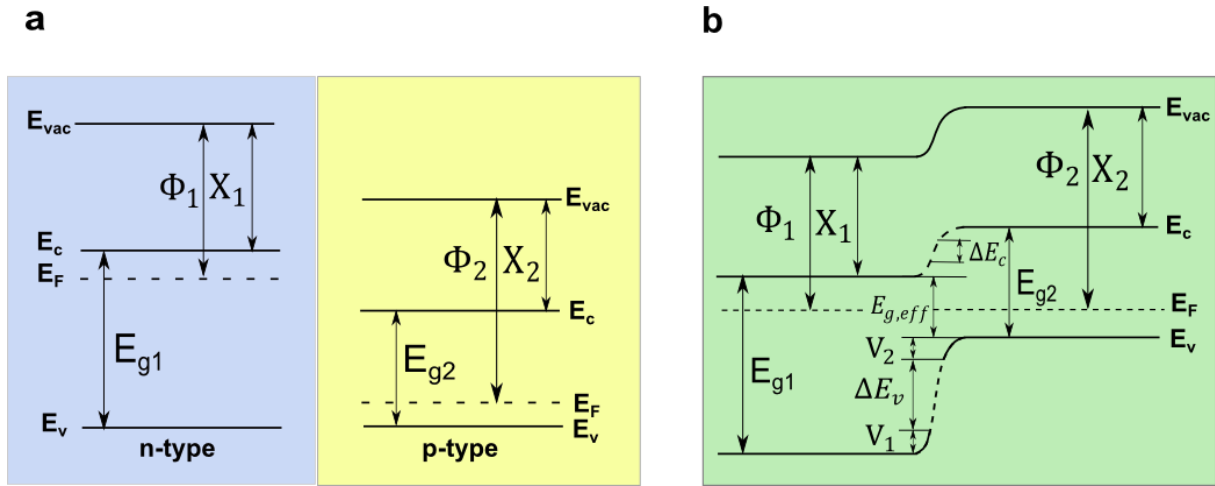


Fig.3.5. The heterojunction of two semiconductor materials, a: shown apart, b: in junction. [6] See text for the symbols explanation.

### 3.2.1. Anderson rule

The Anderson rule can be used to construct the band diagram in the semiconductor heterojunction. It was first described by Anderson in 1960 and is based on the electron affinity of the materials used to build the junction. [42] Assuming that the vacuum levels of both semiconductors that form a heterojunction should be aligned, one can build an energy band diagram of the heterojunction of two semiconductors. Using the electron affinity  $\chi$  and the band gap  $E_g$  values, known material parameters of the semiconductors, the conduction band offsets  $\Delta E_c$  can be obtained:

$$\Delta E_c = \chi_2 - \chi_1 \quad (3.2)$$

where  $\chi$  is the energetic distance from the lower edge of the conduction band to the vacuum level.

Unfortunately, the Anderson rule doesn't work in the real heterojunction. The idealized model and equation (3.2) of the conduction band offset  $\Delta E_c$  do not take into account interface and defect states of

the imperfect crystal structure of the real semiconductors. The assumption that only the electron affinity of the semiconductor will define the band offset in a junction failed due to the fact that the deposition method, substrate and processing temperature may influence the final material properties of a semiconductor.

### 3.2.2. Common Anion rule

The surface or interface states can have a very large impact on the final band alignment due to their large electrical polarization. To correct the Anderson model, the common anion rule was proposed. Assuming that the valance band of a semiconductor is formed with the  $s$  – and  $p$  –states of its anions, the valance band offset at the heterojunction will be very small, if the anion composition of the absorber and buffer is identical. The optical measurements of the alignment at the AlAs/GaAs interface have provided strong evidence for the common anion rule to be correct. [43] It was shown that the band gap difference between two compounds that formed the interface is mainly located in the conduction band  $\Delta E_c$  and to much less degree in the valance band  $\Delta E_v$  discontinuities. To be more precise, the  $\Delta E_c$  accommodates 85% of the band gap difference and  $\Delta E_v$  the remaining 15%.

However, later works in this field using different experimental techniques had shown that the common anion rule fails for many other systems such as  $Al_{1-x}Ga_xAs/GaAs$ . The results were contradictory to the predictions of the common anion rule: the difference in band gap was distributed more evenly between  $\Delta E_v$  and  $\Delta E_c$ . On average,  $\Delta E_v$  contains approximately 40% of the  $E_g$  difference.

The ambiguity between theoretical model and experimental results was puzzling and doubted the principle understanding of the nature of the electronic states in compound semiconductor. Wei and Zunger have proposed a new model to describe the electronic states important for the interface formation. [44] They have shown through all-electron first-principle calculations that not only anions but also in addition non-s-p-cation components contribute to the  $\Delta E_v$ . The so-called extravalence (e.g. Al 3d) and subvalance (e.g. Zn, Cd, Hg outer d orbitals) states of cations act as a main discriminating factor for the band offset at the interface of two semiconductors with common anions and lattice parameters. Previously the common anion rule has neglected cation d states and accounted them as unimportant in the vicinity of the valance band edge. [45]

Also Tersoff [46] has proposed to account for the interface dipole that defines the final line-up. In analogy to the Schottky metal-semiconductor junction, where metal-induced gap states pin the Fermi level, in the heterojunction of the two semiconductors, the induced mid-band gap states at the semiconductor surface form a dipole. This dipole can become neutral if the mid-gap energies of the contact surfaces are aligned.

Summing up, Anderson's as well as the common anion rule are the first attempts to better understand the band alignment nature at the heterojunction. Using the bulk properties of the semiconductor as the initial conditions, classical theoretical models don't take into account properties of surfaces that actually build the junction. However, experimentally it was found that for some systems, namely GaAs/AlGaAs, the Anderson's rule can work fairly well. Thus, for the  $0 \leq x \leq 1$  in  $Al_{1-x}Ga_xAs/GaAs$  system, the special case of Anderson rule, the so called *60:40 rule*, can be applied to calculate the conduction and valance band offsets [47]:  $\Delta E_c : \Delta E_v = 60 : 40$ .

### 3.3. Solar cell basics

A solar cell is an electronic device that converts sunlight into electric power. [48] The requirements are: the photovoltaic material, in which the absorption of the light excites electrons to a higher state, collection of the light-generated carriers and large enough voltage across the cell so that the excited electron moves from the cell into an external circuit, so that it can dissipate its energy and return to the cell.

The light-generated current is a two-step process, where firstly, the photon gets absorbed and the electron-hole pair is created. The lifetime of the carriers should be long enough, so that hole and electron get separated spatially by the electric field that exists in the p-n junction and they don't recombine. That is the second part of the process. The separated carriers flow through the external circuit, thus the current is generated.

Of course, there is a certain probability of the light-generated carriers to be separated by the p-n junction. It is called collection probability and depends on the distance the carrier must travel before they get separated. If the electron-hole pair was created within the depletion region, they are quickly driven away from each other by the junction. If the pair was created far away from the junction and more than the diffusion length, the collection probability of those carriers is quite low. [48]

The number of light-generated carriers alone doesn't determine the electric power in the cell. In order to generate power, a voltage must be generated together with current. Under illumination, the carriers are generated so that there is an increase of free electrons and holes in the junction. The increase of the light-generated respective minority carriers creates an electric field opposite to the one already existing in the p-n-junction. This light-induced field reduces the net field and therefore the barrier for the diffusion current. Under open circuit conditions, where no carriers are leaving the cell, the light-generated current increases till it gets balanced by the forward bias diffusion current. The voltage required to balance two currents is called "open-circuit voltage". Under short circuit conditions, the carriers can exit the device and no charge build-up happens. [48]

There are a few important parameters used to characterize a solar cell: the short-circuit current ( $I_{sc}$ ), the open open-circuit voltage ( $V_{oc}$ ), the fill factor (FF), efficiency.

The  $I_{sc}$  is the current across the cell under the zero voltage applied. In the ideal solar cell, the light-generated current and short-circuit current are identical, in case of the low resistive losses. Thus, the  $I_{sc}$  is the largest current that can be produced in the cell.

The  $V_{oc}$  is the maximum voltage possible in the cell, when the current is zero. The  $V_{oc}$  corresponds to the forward bias of the solar cell with the light-generated current. Equation for the  $V_{oc}$  is given by:

$$V_{oc} = \frac{nkT}{q} \ln\left(\frac{I_L}{I_0} + 1\right) \quad (3.3.)$$

where  $I_L$  light generated current,  $I_0$  dark current, ideality factor  $n$ , Boltzman constant  $k$ , temperature  $T$ ,  $q$  – absolute value of the electron charge. The value of the ideality factor depends on the recombination mechanism and location and can be derived from the slope of the dark-I-V curve. [48]

Therefore the  $V_{oc}$  depends on both, the dark and light-generated currents. The dark current in its turn, depends on the recombination in the cell and often the  $V_{oc}$  deficit (defined as  $E_g/q - V_{oc}$ , where  $E_g$  is the absorber band gap and  $q$  is the elementary charge [49]) becomes a big issue for the device

performance. Identifying the reasons of the low  $V_{oc}$  and overcoming those, is one of the main paths for the device improvement. Such reasons can be the secondary phases in the bulk and near surface region, defects, band tailing, and interface recombination. [50]

Thus, the  $V_{oc}$  and  $I_{sc}$  are the maximum voltage and current of the device, but there is no power outcome at both operating points. To characterize the maximum power obtained from the cell the fill factor FF is normally used. FF is the ratio of the maximum power of the cell to the product of the  $V_{oc}$  and  $I_{sc}$ .

$$FF = \frac{I_{mp}V_{mp}}{I_{sc}V_{oc}} \quad (3.4)$$

where  $I_{mp}$  and  $V_{mp}$  are the current and voltage and the maximum power point.

The most common parameter that used to evaluate the device performance is the efficiency  $\eta$ . Efficiency is the ratio of the cell's output  $P_{max}$  to the sun incident power  $P_{in}$ :

$$\eta = \frac{P_{max}}{P_{in}} = \frac{V_{oc}I_{sc}FF}{P_{in}} \quad (3.5)$$

Efficiency is the parameter that is not only describing the device performance, it also depends on the incident sunlight, i.e. spectrum and intensity of the light and temperature of the cell. Therefore, the condictions under which the  $\eta$  is measured have to be precisely controlled in order to be able to compare performances of different cells. Typically, solar cells are measured under AM1.5 (AM stands for the air mass coefficient, used to characterize the solar spectrum after the light has passed through the Earth's atmosphere [51] ) and 25°C temperature.

### 3.4. Kesterite based devices

Thin film solar cells consist of many different layers that interact with each other and need to be optimized. The kesterite absorber layer is only one of several layers that have their impact on the final device performance. The principle cell structure (Fig.3.6) was basically copied from CIGSe-based devices which allowed a rapid improvement of the kesterite-based solar cells. The typical cell consists of the CZTS(e) absorber, CdS buffer, intrinsic ZnO window and Mo back and ITO front contact.

A CdS buffer layer was deposited in HZB on top of each kesterite absorber by the chemical bath deposition method using 0.0189 M cadmium acetate dihydrate ( $Cd(C_2H_3O_2)_2 \cdot 2H_2O$ ) in 11.25 ml aqueous  $NH_3$  (25%) and 0.9565 M thiourea ( $H_2NCSNH_2$ ) in 100 ml water which were mixed together and filled up by distilled water to a total volume of 150 ml. The samples were simultaneously dipped into the chemical bath for 40 s at 60 °C leading to ultrathin and 60s for the thick CdS layers (as estimated from the standard CdS deposition process).

In order to compare the electronic properties of the CdS buffer layer, a series of experiments was done using Cd layers deposited by IREC project partner following different recipe: the CdS buffer layer was deposited by a chemical bath deposition, using a cadmium nitrate ( $Cd(NO_3)_2$ ) precursor source. The process was done with concentrations  $(Cd(NO_3)_2)=0.12$  M and  $[thiourea]=0.3$  M,  $pH=9.5$ ,  $T=70^\circ C$ . The process took 40 min to deposit a  $35 \pm 7$ nm thick CdS layer. Cadmium nitrate shows slower growth kinetics of CdS, allowing preparing a layer of higher quality with better incorporation of the sulfur atoms and better surface coverage of the kesterite (which is very relevant for the kesterite absorbers, due to their high roughness). [52]

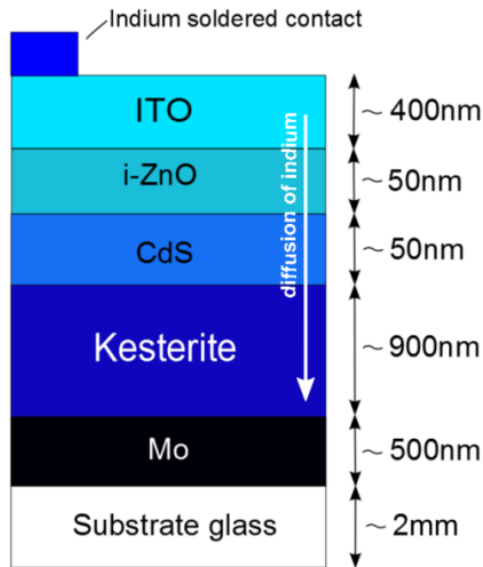


Figure 3.6. Schematic structure of the kesterite-based solar cell

### 3.4.1. Band line up

Interfaces play an important role in the thin film solar cell devices and especially the band alignment between absorber and buffer. If the conduction band minimum (CBM) of the buffer lies below the CBM of the absorber, that alignment is called “cliff”, and vice versa, if the CBM of the absorber lies below the buffer CBM, that will be positive “spike-like” offset. (Fig. 3.7) The influence of the band alignment at the absorber/buffer interface on the final device performance is of a great importance. And there is one more favorable band alignment at the interface that corresponds to the cells of higher efficiencies- the spike-like CBO. This kind of alignment prevents the drop of the  $V_{oc}$ . [52] Any cliff-like alignment leads to the drop in the  $V_{oc}$  due to reduction of the interface band gap and recombination of the majority carriers (Fig.3.7). [52]

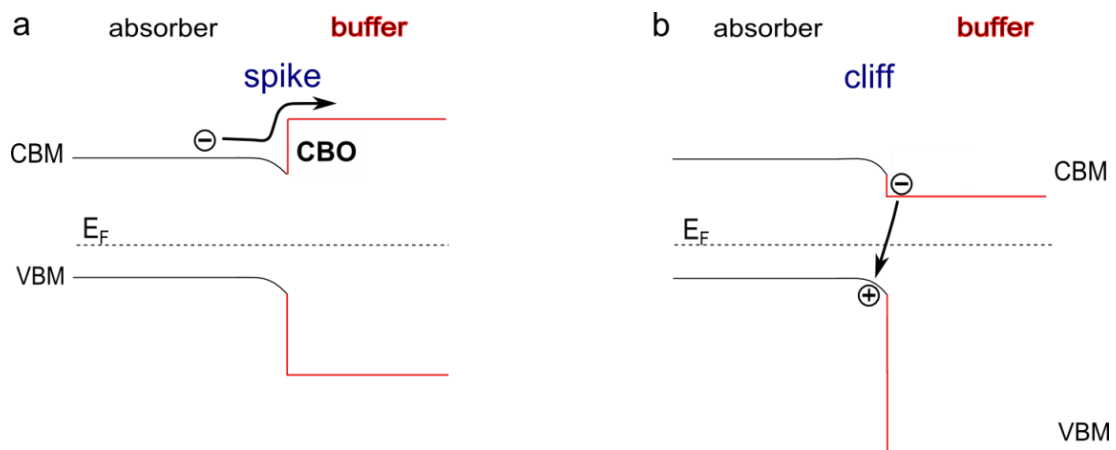


Fig.3.7. Band alignment of the buffer/absorber interface a: spike-like, b: cliff-like. Recombination of the majority carriers is shown schematically.

One of the most commonly used buffer layers and one that gives the highest efficiency of the cells is CdS. In the literature, so far there is no agreement about the type of CBO in the system CdS/kesterite. Santoni et al. [53] have used direct and indirect methods to obtain the VBO at the interface. The indirect method to obtain the VBO involves the measurements of the core levels energies:

$$VBO = [E_{VB}^{CdS} - E_{VB}^{CZTS} + V_{bb}] \quad (3.6)$$

where  $E_{VB}^{CZTS}$  and  $E_{VB}^{CdS}$  are the energy distances between valance band edge and Fermi level of the kesterite and CdS materials, respectively and the  $V_{bb}$  can be obtained from the formula:

$$V_{bb} = [(E_{CL}^{CZTS} - E_{CL}^{CZTS}(i)) + (E_{CL}^{CdS}(i) - E_{CL}^{CdS})] \quad (3.7)$$

where  $E_{CL}^{CZTS}$  and  $E_{CL}^{CdS}$  are the core level energies of the selected element measured in the bulk of the material, and then at the interface:  $E_{CL}^{CZTS}(i)$  and  $E_{CL}^{CdS}(i)$ . In the present heterojunction, Sn 3d<sub>5/2</sub>, Cu 2p<sub>3/2</sub>, Zn 2p<sub>3/2</sub> core level peaks originating from the kesterite layer and Cd 3d<sub>5/2</sub> from the CdS can be used to determine the band bending at the kesterite/CdS interface. The direct method involves the straightforward analysis of the XPS valance band edge spectra measured at the interface. Therefore, the obtained results suggest a cliff of -0.3 for the pure sulfide using the direct method of determining band offsets and -0.34eV for the indirect method. [53] This value was confirmed by Bär et al. [53].

Haight et al. [55] have determined band offsets at the interface CdS/CZT(S,Se) with three different [S]/([S]+[Se])-ratios. They found weak p-doping of their samples and a clear dependence of the VBM on composition and they calculated a spike-like CBO for all three samples. The CB offset they found was 0.48 eV for pure CZTSe and CZT(S,Se) with [S]/([S]+[Se]) = 0.45. For the pure CZTS they found a CBO of 0.41. However, their samples were prepared using thermal evaporation (pure sulfide) and a hydrazine-based chemical deposition (mixed sulfide/selenides). Also, in contrast to our standard UPS measurements they utilized femtosecond laser, pump/probe UPS, where surface/interface band bending can be avoided.

Tajima et al. [56] have measured band offsets using hard X-ray PES (HAXPES) and found a CBO of 0.0 eV, i.e. no conduction band offset for the pure sulfide kesterite.

However, the usage of the Cd is not permitted in several countries and it is registered as a hazardous material in many others. Therefore several alternative buffer layers were proposed such as ZnO, ZnS, Zn(O,S), In<sub>2</sub>S<sub>3</sub>, but the achieved efficiencies were always lower than that of CdS. [55], [57]

One of the methods to achieve the best band line-up between absorber and buffer, namely a small spike of less than 300 meV, is to tune the band gap of the absorber and therefore the resulting offset at the interface. For that purposes the anion composition of the kesterite can be varied and consequently the band gap of the absorber would be of the required value. The thermal processing of the metal precursor is the pathway to introduce in to the final material atoms of sulfur and selenium in different ratios so that the desired value of the band gap will be achieved. So far, it is known that the pure selenide kesterite band gap is around 1 eV and that of pure sulfide compound 1.5 eV. [58], [59]

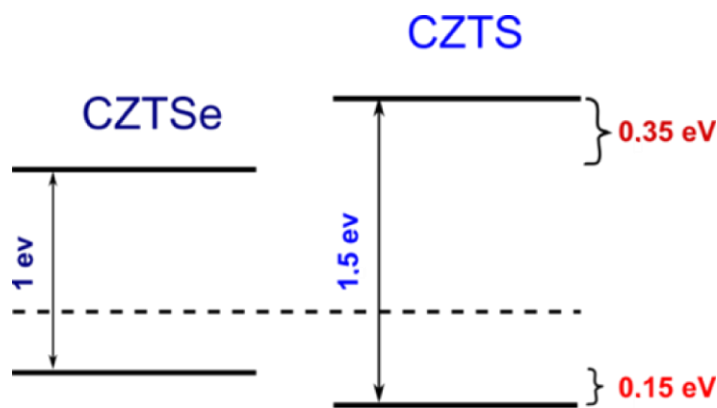


Fig.3.8. Schematic diagram shows the transition from pure sulphide to pure selenide composition. Consequent shifts in CB and VB are shown.

However, it has been not very clear how the conduction and valance band shift when the composition of the absorber is going from pure sulphide to pure selenide for some time in literature. The relevant theoretical calculations have provided positions of the conduction and valance bands to vacuum level as well as band gap values for different kesterite compositions. The calculations were made using density functional theory (DFT) implementing the *kesterite* crystal structure, as reported to be the most energetically favourable one, in comparison to the stannite crystal structure. [60] Therefore, it was shown, that the change in the band gap is due to both – conduction and valance bands shifts. The total change in the band gap of 0.5 eV when going from pure sulphide to pure selenide is distributed between a -0.15eV shift in the valance band and +0.35 eV in the conduction band. [58] (Fig.3.8) The offsets with the CdS buffer layer were also obtained: +0.26 eV spike for the CZTSe/CdS heterojunction and -0.09 eV cliff for the CZTS/CdS. The acceptable alignment at the kesterite/CdS interface can explain the advantage of CdS usage as a buffer material in the final devices. [58]

### 3.5. Summary of the chapter

The solar cell as one application of a p-n diode was introduced in this chapter. The physical principles of the band alignment formation and current flow were described. Bringing two different semiconductors in contact leads to formation of the heterojunction; the physical principles discussed for a p-n homojunction- are still valid. Solar cell parameters such as open circuit voltage and efficiency that are important for the performance characterization were described. Kesterite-based thin film solar cells consist of many different functional layers, such as CdS and i-ZnO. Kesterite absorbers with different S and Se content are the main object of study in this work.



## 4. Experimental methods

Different experimental methods have been used in this work to characterize the kesterite samples with different  $[S]/([S]+[Se])$  ratios. The relative composition as well the influence of different chemical etchings on the sample surface have been studied using X-ray photoelectron spectroscopy (XPS). The surface electronic properties, namely the VBM position was measured with ultraviolet photoelectron spectroscopy (UPS). Further investigations of the near-surface region have been done at the synchrotron BESSY II using different excitation energies. And finally the development of the conduction band edge when going from pure sulfide to pure selenide composition has been probed by the absorption spectroscopy. All these experimental techniques are described in chapter 4, including theoretical concepts and the practical application in frame of this work.

### 4.1. Photoelectron spectroscopies

#### 4.1.1. X-ray photoelectron spectroscopy

The analysis of material surfaces by XPS is performed by irradiating the sample with soft X-ray light and analysis of the emitted photoelectrons. For this purpose usually Al and/or Mg anodes are used. As electrons bombard the anodes, they emit soft X-rays: Al  $K\alpha$  (1486.6 eV) and Mg  $K\alpha$  (1253.6 eV). The X-ray light beam interacts with atoms of the matter via the *photoelectric effect* so the photoelectrons will be emitted (Fig.4.1, top picture). This physical phenomenon was reported first by H. Hertz [61] in 1887 and later theoretically described by A. Einstein [62] in 1905 via equation:

$$E_{kin} = h\nu - E_{bin} - \phi_s$$

where  $h\nu$  is the energy of the X-ray beam photons,  $E_{kin}$  is the kinetic energy of the emitted photoelectron and  $E_{bin}$  its binding energy, namely the atomic orbital from which its originates, and  $\phi_s$  is the work function of the spectrometer. The binding energy is also sometimes called ionization energy. Here it is referred to a specific atom shell that was involved in electron emission. The probability for each ionization process is called a cross-section.

In addition to the photoelectrons, Auger electrons get emitted from the sample surface due to the relaxation of the holes left after the photoelectron emission (Fig.4.1, bottom right picture). The Auger process is competing with the other possible relaxation mechanism- emission of the photon, i.e. fluorescence, schemically shown in Fig.4.1, bottom left picture.

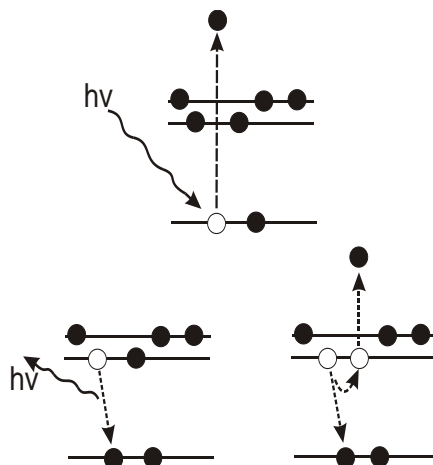


*Fig.4.1. The schematic diagram of the relevant processes under X-ray/UV radiation. Top picture: photoelectron emission, bottom left: radiative recombination (emission of the photon), bottom right: non-radiative recombination (Auger process).[116]*

The Auger emission is a two-stage process. First, the emitted photoelectron leaves a hole behind that can be filled with an outer electron that fills the formed vacancy. Afterwards, the second electron carries off the energy excess and gets emitted out of the sample's surface. The resulting Auger electron will have a kinetic energy equal to the difference between initial and final ion energies, thus independent from the initial excitation energy of the incoming beam.

The photoelectrons interact with matter much stronger than the photons. Therefore the mean free path of the photoelectrons is only in the order of tens of Angstroms, while for photons it is in the order of micrometers. Thus, only those of the photoelectrons will “escape” the solid that originate within tens of Angstroms below the surface. The emitted photoelectrons and Auger electrons are further separated in the analyzer by applying an electric field inside of it and finally, quantified by the electron multipliers (channeltrons). Electrons emitted without energy losses will produce the peaks in the spectra; the rest, also called secondary electrons, will form a background.

#### 4.1.2. The CISSY

The CISSY machine was built by PINK GmbH, Wertheim, Germany and was designed to be not only laboratory equipment but also a mobile endstation for the synchrotron experiments. The name CISSY is built from two words: CIS and Synchrotron.

The vast majority of the presented XPS and UPS experiments in this work were done at the CISSY machine. It consists of three main chambers: load-lock, preparation and analysis chambers. The studied samples get introduced to the system via the load-lock (Fig.4.2); afterwards the sample can be transferred into the preparation chamber and further into the third main chamber – the analytic chamber. In addition, several chambers are attached to the machine: a sputtering chamber where, Zn(O,S) buffer layers can be sputtered, and a freshly-developed preparation chamber for the KF and NaF deposition.

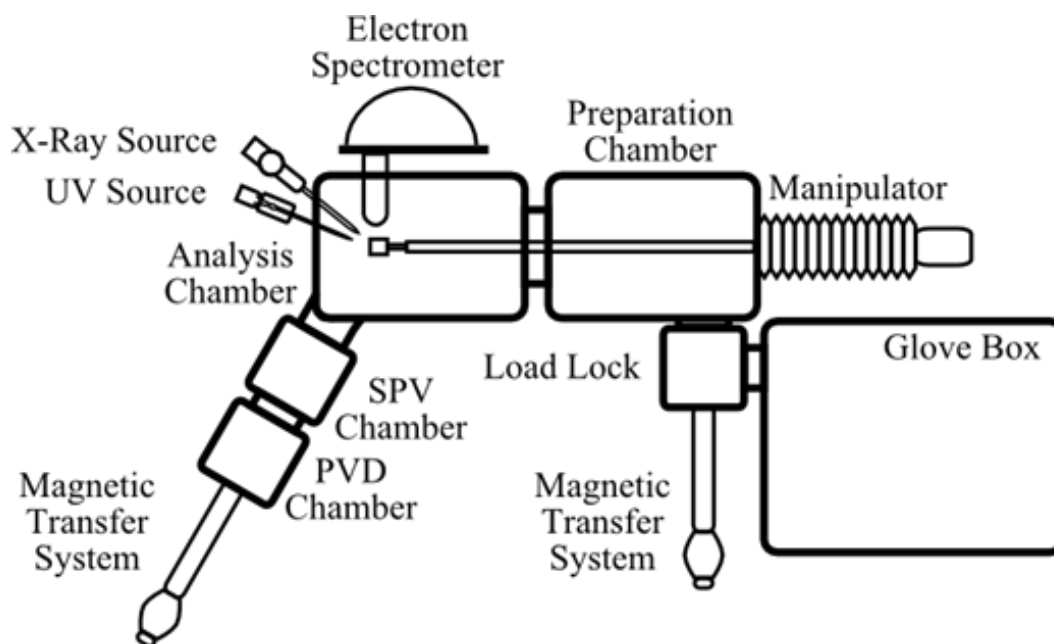


Fig.4.2. The schematic diagram of the CISSY machine [63]

All chambers are kept under ultra-high vacuum of about  $<10^{-8}$  mbar and equipped with shutters that separate them from each other to prevent them from leaks or unwanted ventilation. One of the reasons for this rather low pressure is that sample surface contamination and consequent signal attenuation happens extremely quickly. Even at a pressure of  $10^{-7}$  mbar the surface of the sample is contaminated with a 1.0 monolayer of gas molecules already after 10 sec, at  $10^{-8}$  mbar after 100 sec, assuming a sticking coefficient of 1.

Also, the CISSY machine is equipped with an XR-50 X-ray source from Specs that also requires an ultra-high vacuum to operate. And finally, to ensure a correct work of the photoelectron analyser from VG so that the dissipation of the photoelectrons via inelastic collision with the gas molecules will be minimized, a low pressure is kept inside the machine. [64]

There are several additional tools at CISSY:  $N_2$ -filled glove box for the various preoperational steps such as wet chemical etching, sample mounting etc.; the treated sample can be transferred into the analytic chamber without vacuum break for the further analysis using X-ray or UV light. The Argon gun allows sputtering and study depth-profiles of different functional layers of the thin film samples.

### 4.1.3. The work function

During the XPS measurements, an atom absorbs the photon  $h\nu$  and the core level electron gets ejected, detected and its kinetic energy is measured. In Fig.4.3 the schematic diagram of the energy levels relevant for the photoemission process is shown. Here the photoelectron is escaping from the sample into the spectrometer. It is important that the conductive specimen is in electric contact with the sample holder and spectrometer so that they have the same reference energy level – the Fermi level,  $E_F$ . As the reference Fermi level is valid for each measured sample and a particular spectrometer, the comparison of the spectra in binding energies becomes possible.

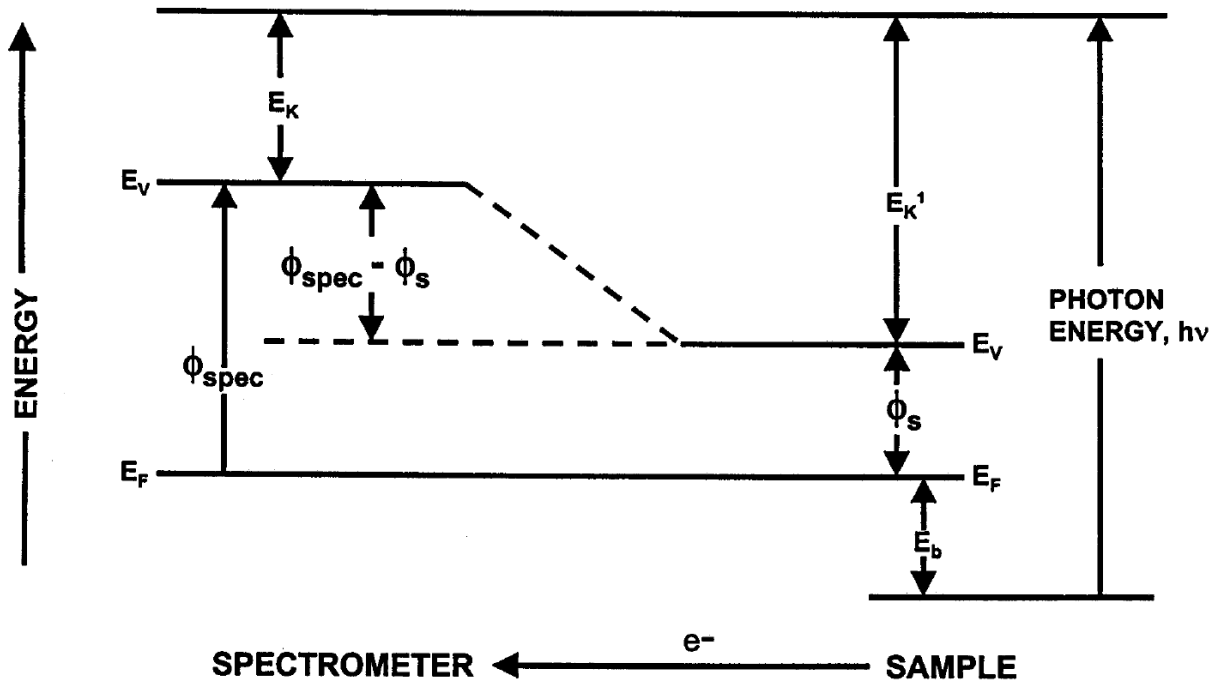


Fig.4.3. The schematic diagram for the XPS binding energy measurements [64]

The incoming photons create the photoelectrons with the kinetic energy  $E_k^1$  relative to the vacuum level of the sample  $E_{vac}$ . The kinetic energy of the photoelectron after entering the spectrometer surface will be determined using the relation:

$$E = E_k^1 + \phi_s - \phi_{spec} \quad (4.1)$$

where  $\phi_s$  and  $\phi_{spec}$  are the work functions (energy required to eject electron from the Fermi level to the vacuum level) of sample and spectrometer, respectively.

Those secondary electrons leaving the sample's surface with zero kinetic energy due to inelastic collisions form the secondary electron edge of the UPS spectra and are also affected by the difference in the spectrometer and sample work functions:

$$\phi_s = E_{cutoff} + h\nu - E_F - V_{bias} \quad (4.2)$$

where  $E_{cutoff}$  is the position of the secondary electron edge,  $V_{bias}$  the voltage that is usually applied to the sample to improve the signal to noise ratio, basically artificially accelerating low energetic photoelectrons towards the detector.

#### 4.1.4. Quantitative evaluation of the XPS data

As the kinetic energy  $E_{kin}$  of the collected photoelectrons has been determined, with the known excitation energy  $h\nu$  and work function  $\phi_s$ , the binding energy  $E_{bin}$  can be calculated for all photoelectron peaks in the spectrum. The spectral features can be used to identify the sample

composition, i.e. the binding energy of the photoelectron peak together with the energy of the corresponding Auger peaks can be used to determine the emitting element and its chemical state. For instance, higher binding energies in comparison to the reference will indicate the possible presence of oxides.

The absolute chemical composition of the sample is difficult to obtain due to some limitation of the technique. The relative chemical composition can be obtained with a much better accuracy. For that, the area under the peak can be integrated and the fraction of the respective element in the sample can be estimated. The integrated intensity of the peak derived from a core level X in an atom A from a homogeneous solid sample is given by:

$$S_A(X) = \sigma_A(h\nu, X)\beta_A(h\nu, X)N_A \cos\varphi \lambda_M(E_{kin})K(h\nu, E_{kin}) \quad (4.3)$$

where  $\sigma_A(h\nu, X)$  is the photoelectron cross-section which is different for each element A and for each atom sub-shell,  $\beta_A(h\nu, X)$  is an asymmetry parameter,  $N_A$  is the average element A concentration at the particular analysis depth,  $\cos\varphi$  is the cosine of the emission angle, which is defined as an angle between the surface normal and the angle of emission,  $\lambda_M(E_{kin})$  is an inelastic mean free path (IMFP) of the excited photoelectrons in matter,  $K(h\nu, E_{kin})$  is the normalization factor related to the incident X-ray flux, and  $T$  the transmission function of the analyser.  $T$  has to be determined for each analyser specifically, therefore it was obtained for the CISSY machine analyser by comparing peak intensities of different metal samples at different kinetic energies and described in detail by R. Tschöke. [65]

Other parameters can be obtained from available literature sources. The cross sections are given by Scofield [66], Trzhaskovskaya [67], and Yeh [68]. As cross sections strongly depend on the excitation energy, it is possible to tune it to gain more signal from one or another element. For that purpose the synchrotron radiation is the most appropriate and will be discussed in the following section.

The  $\beta_A(h\nu, X)$  asymmetry parameters are shown in Reilmann et al. [69]

To determine the  $\lambda_M(E_{kin})$  IMFP for a specific material, the QUASES-IMFP-TPP2M code [70] can be used. The intrinsic material parameters, such as bulk density, number of the valence electrons and band gap must be provided to calculate the IMFP for a particular kinetic energy of the photoelectrons in the studied sample.

Nevertheless, with all mentioned above parameters, the accuracy of the absolute composition determination is not higher than 10-20 %. To get a more precise picture of the studied surface, one can work in relative terms so that the unknown parameters can be neglected. Also a comparison of the peaks of the same kinetic energy will improve the precision of the calculations. In the following chapters *relative* chemical compositions of the different samples will be compared using the equation and procedure described here.

#### 4.1.5. Ultraviolet photoelectron spectroscopy

The excitation energies below the soft X-rays lie already in the ultraviolet (UV) range, therefore the photoemission spectroscopy using UV light is called ultraviolet photoelectron spectroscopy (UPS).

There are two commonly used excitation sources for UPS: He I (21.22 eV) and He II (40.82 eV). At the CISSY machine the UV lamp allows to tune the excitation energy, i.e. varying the ratio of the He I or He II component in the incoming beam. The resolution of the UPS is varying from 3 meV up to 17 meV depending on the excitation sources and is suitable for valence band measurements and precise depicting of the valence band edge, which is of a high interest in this work. [6]

#### 4.1.6. Analysis of the UPS spectra

The position of the valence band maximum (VBM) can be measured with UPS or photoemission using synchrotron radiation, but the procedure of the VBM determination is valid for both types of spectra. The method is based on the linear extrapolation of the leading edge of the measured spectra till its intersection with the base line. As an example, in Fig.4.4. the typical UPS spectra together with the extrapolated linear edge of the spectra and the value of the VBM are shown.

The curvature of the leading edge of the VB edge is often limits the precision of the graphical method described above. Due to the non-linearity of the VB spectra edge, the VBM value can be determined with the error margin of 0.1 eV.

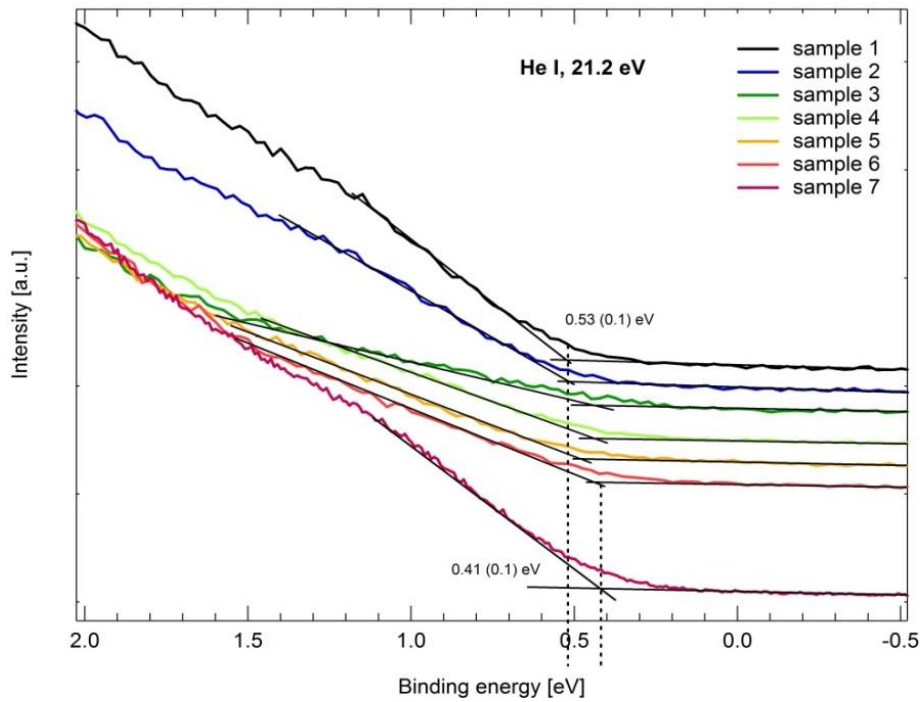
The described method of the VBM determination via the linear extrapolation of the VB spectra leading edge is often used in literature. The physical reasons behind this method can be nevertheless discussed in detail. The excitation source used for the UPS is a He lamp with  $E_{\text{ex}}(\text{He I})=21.2$  eV. The line width of this excitation is very narrow, namely 3 meV [6] and has practically no influence on the line shape. As well as the analyzer, which was set to 2.5 eV pass energy, will have minimal effect on the measured spectra.

So, the point of the VBM can be determined using a linear extrapolation of the VB edge. As was mentioned above, often, due to the non-linearity of the VB edge, the linear extrapolation cannot be done precisely enough and in this case additional knowledge about the studied system would help to localise the VBM in the specific region. That can be data about the band gap of the semiconductor, complementary experimental results and other information found in literature. In addition, several photoelectron experiments can be performed with same or similar samples, in order to observe differences and similarities in the spectra. The true VBM value will be reproducible and independent from contamination or impurities of the sample surface.

The valence band edge consists of many non-localized states, which overlap with each other. The sum of these states steadily approaches zero, so the edge of the valence band forms a cut-off that can be measured with UPS. If the density of the valence band states is broadened to account for the excitation energy and instrumental width, weighted to account for the respective ionization cross section, the linear extrapolation of VB edge can be justified as a method to determine the VBM.

Another method to determine the VBM from the VB spectra is to use the parabolic fit of the measured features. It was shown by B. Johnson [6], that the parabolic valence band edge approximation gives a similar result to the linear extrapolation method. Therefore, further in this work the VBM values will be determined using the linear edge extrapolation of UPS and synchrotron-derived data.

a



b

Sample number	[S]/([S]+[Se])
1	1
2	0.95
3	0.64
4	0.49
5	0.24
6	0.06
7	0

Fig.4.4. a: the UPS spectra of the VB edge of the kesterite samples with different  $[S]/([S]+[Se])$  ratios. b: the detailed sample anion composition is given. Sample 1 is a pure sulfide, sample 7 is a pure selenide. Valence band maxima are determined for all samples after etching. The leading edges of the valence band curves are extrapolated linearly and the intersection with the base line is taken as the value for the VBM

## 4.2. Synchrotron radiation at BESSY II

The photon energies that lie above the standard laboratory XPS refer to the hard X-ray photoelectron spectroscopy (HAXPES). Using these energies the experimentalist can achieve a lot more, then only with standard XPS. The mentioned energies above 2000 eV are available at the synchrotrons, such as BESSY II in Berlin, where all results presented here have been obtained. The experiments were performed at different end stations depending on the goals of the study and will be specified for the each set of results. What is so special about the synchrotron radiation that makes experiments done at such facility are so valuable? First of all, it is an increased information depth due to a higher kinetic

energy of the photoelectrons. The HAXPES regime is considered within the range of 2-12 keV kinetic energies and with the corresponding probing depth of 2-20 nm. [70]

Also, when using a laboratory X-ray gun, the cross-section for the different core levels differs a lot for different elements- for some it is at its maximum value, some are at the minimum at the same excitation energy. [64] To avoid these limitations, a continuously tunable source can be used, such as synchrotron radiation.

In the present work, the synchrotron radiation was used to examine the depth-dependent surface cation composition of the kesterite samples, the shift of the VB edge when going from pure sulfid to pure selenide anion composition. Also, we have applied a specific type of absorption spectroscopy – the near edge X-ray absorption fine structure (NEXAS) to study the conduction band edge of kesterites.

#### 4.2.1. NEXAFS

One of the most common methods for the CBM probing is the inverse photoelectron spectroscopy (IPES). We have chosen the absorption spectroscopy and its special case- NEXAS as an alternative tool for the conduction CBM study.

The detection of X-ray absorption depends on two-stage process. First, after interacting with electromagnetic radiation core electrons get excited into unoccupied states in the conduction band. Secondly, the core hole left behind relaxes via a radiant process. The emitted photon can be registered and contributes to the absorption spectra. Thus, the initial state of the absorption process is the ground state of the system, before the photon absorption and the final state is the excited atom ion after a transition. The transition probability  $\mu$  is given by the product of matrix element  $M_{if}$  for interaction and density of the final states  $\rho(E_f)$  and commonly called *Fermi's Golden rule*:

$$\mu \sim \frac{2\pi}{\hbar} |M_{if}|^2 \rho(E_f) \quad (4.4.)$$

where the index  $i$  stand for the initial state,  $f$  for the final;  $M_{if}$  shows the “strength” of the coupling between the initial and the final state of the system, and  $\rho(E_f)$  shows the number of the ways the transition can happen. [71]

As was already mentioned, absorption spectroscopy is a probe for the unoccupied states in the CB. The electron gets excited from the core level into the unoccupied state in CB in accordance with the *dipole selection rules*.

In order to better interpret the absorption process, we have to consider the following selection rules for the excitation of the core level electron to be allowed [72]:

$$\Delta l = \pm 1 \quad (4.5.)$$

where  $l$  is an angular momentum quantum number, i.e. the transition is allowed only if the difference between the initial and final states quantum numbers is +1 or -1.

To be precise, it is necessary to mention that NEXAFS contains information about the *partial* density of states in the conduction band seen by the already excited electron. As the excitation energy of the

beam is increasing, the core level electrons are getting excited into the final state in the conduction band, leaving behind a core hole after the absorption. Thus, we assume that the unexcited state, prior to X-ray absorption, is an initial state, and a core hole represents a final state of the studied system. This means that NEXAFS shows the density of unoccupied states in the conduction band in the ground state, before the absorption occurred, i.e. NEXAFS spectra contain information about the local density of states (LDOS) seen by the excited atom in the initial state. [6]

Interestingly, the local density of states (LDOS) of each of the studied groups of atoms may contribute differently to the conduction band minimum; therefore, the transition studied with NEXAFS also would be different for each atom. The measured energy distance between the core level and the final state in the CB is element-specific and can vary or not within the given stoichiometry of the sample. The local electronic environment of each atom of the material with a fixed composition and the measurable optical band gap becomes finally evident at the macroscopic level. [73] Therefore, the straightforward interpretation of the absolute position of the absorption edge is not possible, not only because of distortions caused by the core hole (i.e. the final state), but it also can happen that the LDOS measured by NEXAFS does not overlap with the bottom of the conduction band, as we expected. [6]

#### 4.2.2. NEXAFS spectra

In the NEXAFS experiment the sample is radiated with X-rays of defined energy. Some of the X-rays are absorbed and according to the photoelectric effect, will cause the excitation of the electron. There are several ways to quantify the absorption happening in the sample. First, one can measure the intensity of the incident beam before the sample and compare it to the intensity of the transmitted beam. That method will stand for the transmission detection mode.

The radiative recombination of the core hole left by the excited electron can also be used to quantify the absorption in the sample. The photon released during the hole's decay will therefore contribute to the spectra recorded in the fluorescence detection mode.

And finally, by measuring secondary electrons ejected from the sample surface, spectra can be obtained in the total electron yield mode.

After the absorption is detected for the specific energy of the incident beam, the energy is slightly changed and a process is repeated. [74] Stepwise, an absorption spectrum is created at the given range of energies.

A typical NEXAFS spectrum, shown in Figure 1, contains the absorption edge itself and a region of tens of eV just after the edge, and is therefore called *near edge* fine structure spectroscopy (marked with the blue box in Fig.4.5). The oscillations starting several tens of eV after the edge are known as extended absorption fine structure (EXAFS) and contain information about the crystal structure. The intervals between the propagating oscillations depend on the distance between the absorbing and scattering atoms. [74]

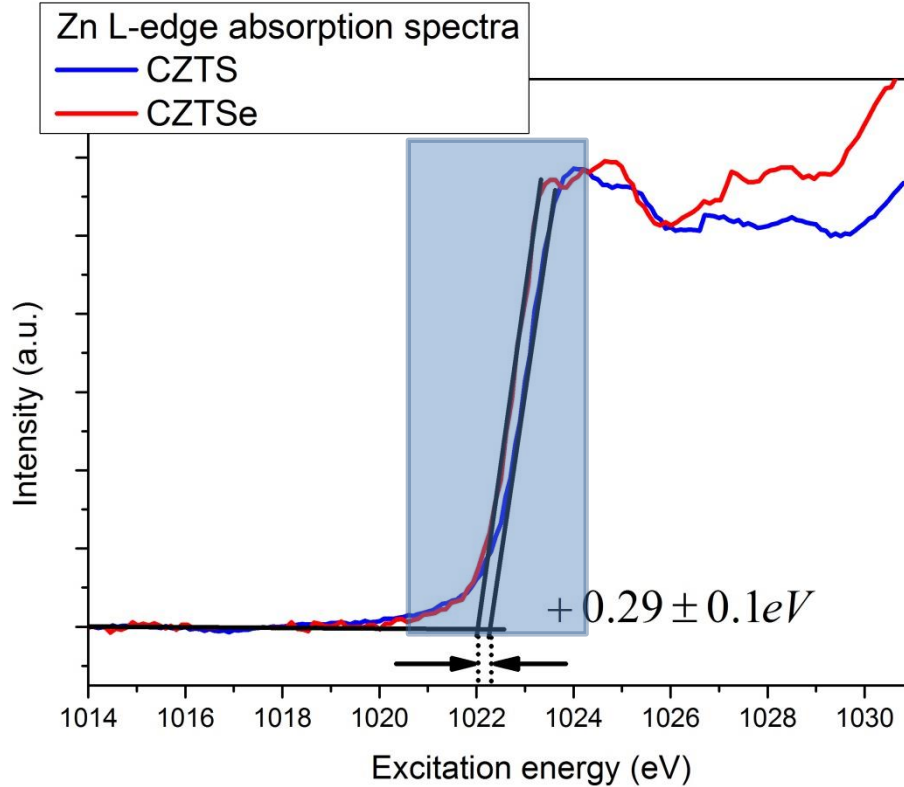


Fig.4.5. A typical absorption spectrum, where the NEXAFS region is marked with a blue box.

When the opening of the band gap is studied, such as in this work, calibrated NEXAFS spectra obtained from different samples can be used to determine a relative CBM shift. For instance, the Zn  $L_3$  edge of CZTS sample is plotted together with the CZTSe Zn  $L_3$  edge in Fig.4.5. The energy of the absorption edge represents the *difference* in the energy distances between the respective core level binding energy (the Zn  $2p_{3/2}$  level in the case of the Zn  $L_3$  edge) and the lowest unoccupied states that form the conduction band minimum. Therefore both, the respective core level binding energy and the absorption edge energy have to be considered. Due to the similar electronegativity of sulfur and selenium, the position of the initial states, i.e. the binding energies of the cation core level from which electron will be excited, are constant for both pure sulfide and pure selenide kesterite. Thus the comparison of the two similar absorption edges obtained independently for CZTS and CZTSe with the further determination of the meaningful shift between them can be justified. The tangent lines in Fig.4.5. are used for the shift determination between the spectra and the detailed procedure is discussed in the experimental section Chapter 6.

### 4.3. Theoretical methods for the conduction band evaluation

In this subchapter the theoretical methods used for the study of the conduction band development are presented. As going from pure sulfide to pure selenide kesterite composition, the shift in CB is  $0.35 \pm 0,1$  eV according to theoretical calculation available in literature. We decided to perform our calculations using density functional theory and a mono-electronic approach. Thus the *exciting* code and FDMNES are described in detail in the following.

### 4.3.1. Ab-initio calculation of the conduction band states using the *exciting* code

Previously we have shown that the relative shift in the conduction band minimum when going from pure sulfide to pure selenide composition can be tackled using NEXAFS spectroscopy. To understand the origin of the shifts between the absorption edges, the density functional theory (DFT) calculations of the electronic states in the conduction band of CZTS and CZTSe were performed.

#### 4.3.1.1. First-principle approach to the X-ray absorption

All calculations presented in this chapter are performed using the *exciting* code [112] provided by the group of Prof. Draxl and performed by Archana Monoharan.

The DFT calculation is an effective tool used to solve the many-body Schrödinger equation, which describes the system of the real solid. The solid consists of the nuclei and electrons that interact with each other. The many-body Schrödinger equation for such a system will be

$$\hat{H} \psi(\vec{r}_1, \dots, \vec{r}_N) = E \psi(\vec{r}_1, \dots, \vec{r}_N) \quad (4.6)$$

where  $\hat{H}$  the Hamiltonian,  $E$  a total energy,  $\psi$  the many body wavefunction for the  $N$  electronic eigenstates,  $\vec{r}_1, \dots, \vec{r}_N$  are the position vectors of the electrons.

The many-body Schrödinger equation is a complex and a difficult task to solve. The DFT can translate the many-body Schrödinger equation into a simpler single-particle Kohn-Sham (KS) equation that is almost trivial to solve [113]:

$$\hat{H}_{KS} \phi(\vec{r}) = E \phi(\vec{r}) \quad (4.7)$$

There are already many numerical methods to solve the KS equation: the linearized augmented plane waves (LAPW) method, the projector augmented wave (PAW) method, grids... These methods are implemented in different codes: VASP, QE, WIEN2k...

Thus, the complex system of the real solid described by the many-body Schrödinger equation can be converted into the more simple KS equation by the DFT almost without information loss. Nearly no information loss will occur when going from the many-body to the single-particle equation if the “tool” of the DFT is chosen properly. This mathematical object is the so-called exchange-correlation functional. There are different exchange-correlation functionals derived for different material systems and the tasks they have to solve.

In the present work, the *exciting* code was used, which is a full-potential all-electron density-functional-theory package. As was mentioned above, the LAPW is one of the numerical methods that can precisely solve the Kohn-Sham equations of the DFT. [114] And in the current work, the exchange-correlation functional that was used to perform the DFT calculations is the generalized gradient approximation (GGA-PBEsol).

The *exciting* code is a very powerful tool and can be applied to different systems, independent of the building atom species. The package allows studying the physics of the core electrons with a particular focus on the many-perturbation theory. [112] As it follows from the name of the code, the *exciting* is not limited only to ground states, but also allows performing calculations for the excited states, including time-dependent DFT. That can be used to in the end obtain the XAS spectra for metals, molecules, and semiconductors with weak electron-hole interaction. Therefore, it can be successfully applied for kesterite systems to obtain information about the unoccupied states in the conduction band.

In order to better understand the evolution of the band edges of the kesterite system seen with experimental methods, the electronic structure simulations were performed using the all electron code *exciting* and the KS equation as the basic approximation tool. The single-particle equation for the electron gas can be solved self-consistently:

$$\left[ -\frac{1}{2}\nabla^2 + V_H + V_{\text{ext}} + V_{\text{xc}} \right] \psi_{\text{nk}}^{\text{KS}} = \epsilon_{\text{nk}}^{\text{KS}} \psi_{\text{nk}}^{\text{KS}} \quad (4.8)$$

where  $V_{\text{xc}}$  represents the GGA-PBEsol exchange-correlation functional,  $V_H$  is the Hartree potential,  $V_{\text{ext}}$  external potential, that approximates the interaction with nuclear,  $\psi_{\text{nk}}^{\text{KS}}$  is the quasi-particle wavefunction,  $\epsilon_{\text{nk}}^{\text{KS}}$  the quasi-particle energy.

#### 4.3.1.2. Calculation of the band gap using GW approximation

Using data available in literature about the crystal geometry of kesterites obtained with wavelength-dispersive X-ray diffraction and neutron diffraction, the input model was essentially improved. More details on the lattice parameter values used for *exciting* simulations are given in the appendix.

With an already optimized crystal structure, the electronic structure calculations are performed on the DFT level first. The band gap values obtained using the DFT method had a big deviation between calculated and experimentally derived data and were not satisfactory. The band gap of pure sulfide composition was found to be 0.45 eV and for pure selenide to be only 0.06 eV.

A better description of the kesterite band structure has been done by performing the GW approximation. The GW derived band gap values coincide with the experimentally derived  $E_g$  within the error, namely 1.34 eV for CZTS and 0.94 eV for CZTSe compared to experimental results of 1.5 and 1.0 eV respectively, i.e. these results were estimated at about 90% (Fig.4.6).

The underestimation of the band gap using DFT vs. GW was already shown in literature. The accuracy of the standard DFT method is lower for the excited state calculations, i.e. for the band gap, absorption and emission spectra. The underestimations of the band gap with the DFT from the experimental results are in the range of 30%-50%. [118] This problem can be overcome by replacing the Local Density Approximation (LDA) with more reliable approximation, in particularly with the GW.

Therefore, GW can correct the DFT derived band gap values, as was shown previously for kesterites of different compositions. A successful application of the GW was shown for such material systems as CdS and CdTe, ZnS and ZnSe and for other II-VI compounds of zinc-blende and wurtzite structure. [119] However, overestimated band gaps were nevertheless obtained as the d electrons were treated as core electrons. Satisfactory results for the GW quasiparticle band structure were obtained for the cubic CdS [120] and  $\text{CdS}_x\text{Te}_{1-x}$  ( $x=0, 0.25, 0.5, 0.75, 1$ ). [121] In the latter, the problem of the low

band gap values were overcome when the semicore electrons were treated together with valence electrons. The results were therefore improved and in a good agreement with experimental and other theoretical results.

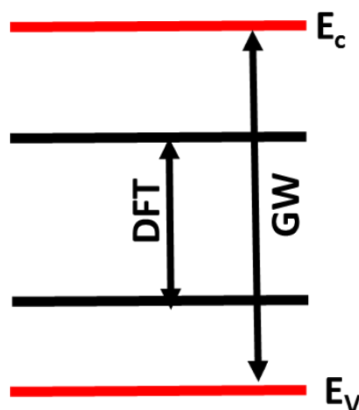


*Fig.4.6. The schematic diagram of the band gap seen by DFT and GW approaches*

Summing up, the GW approximation became recently the novel efficient approach for the first-principles calculation of the band structure of solids. Most of the existing codes use the pseudopotentials of electrons in the valence band only and such an approach can be problematic for the *d* and *f*-electron systems. The GW method can treat core, semicore and valence electrons on the same level, which allows handling a core-valence interaction correctly. Finally, a wide range of materials, irrespective of their composition, can be approximated and a better agreement with experiments can be achieved with the GW method.

#### 4.3.2. FDMNES package

In order to better understand what governs the shape and position of the measured X-ray absorption spectra and how they are expected to change with a change in the anion, simulations of the experimental results can be performed. The K and L absorption spectra of the main kesterite cations can be calculated using the so-called FDMNES software package with certain approximations and simplifications.

We already know that absorption spectroscopy is related to the transition process of a core electron to the final state in the conduction band. Therefore it is necessary to determine the initial state, which is a core level and likely easy to calculate. The main difficulty when calculating the spectra is to evaluate the final state.

For the near edge X-ray fine structure (NEXAFS) spectra there are several methods to calculate the final state. The first group of works in this subject is based on the atomic multiplets for the absorbing atom in the crystal field. [107] The atomic multiplet theory comprises the high-order interactions of the free electrons and determines the non-spherical symmetry of the states, i.e. describes the orbital

polarization and splitting. For example, the core hole and  $3d$  band interaction will be described using high-order terms, which gives rise to a series of the final states of the free electron with different symmetries and energies: the atomic multiplet effect.

The second group uses the local density approximation in the frame of the band structure approach [108] or multiple scattering theory [107], [109]. Typically, the multiple scattering theory uses the muffin tin approximation, which is a widely used approximation for semiconductors and solids in general, but has one disadvantage: it does not work very exact at the interstitial region, i.e. between the atoms.

The finite difference method (FDM) is an alternative way to solve the Schrödinger equation using the local density approximation [110] and allows avoiding the muffin-tin approximation. The FDM is a powerful tool to calculate the NEXFS spectra using different potential descriptions. FDM was used to simulate experimentally obtained absorption spectra (chapter 6). The theory behind is explained in more details in the following.

In the previous subchapter, the *exciting* code was used to calculate the density of states in the conduction band of kesterite with different sulfur and selenium contents. The *exciting* code is the full-potential all-electron density functional-theory package and similarly to FDMNES, implements the LAPW numerical method to solve the Kohn-Sham equation, which is a special case of the Schrödinger equation. Therefore it would be correct to say that FDMNES and *exciting* are related tools to solve the task we are focusing on, i.e. approaches of these two packages are similar and can be used to determine the shift in the conduction and valence bands in kesterite. However, it is important to stress that using the *exciting* code, provided by the group of Prof. Draxl, and calculations performed by A. Monoharan, the density of states in the conduction band of CZTS and CZTSe were obtained, while the FDMNES package has been used to simulate the absorption spectra themselves. Nevertheless, both results are necessary to fully understand the changes in the electronic properties of kesterite.

#### 4.3.2.1. Applying FDMNES to the X-ray absorption spectra

Using NEXAFS as a method to probe the conduction band minimum in semiconductors, the systematic study of the positions of K- and L-absorption edges of all kesterite-related cations was conducted. The absorption edges obtained from the same cation were compared and the observed shift is proportional to the relative shift in the conduction band when going from pure sulfide to pure selenide compositions. In order to better understand what determines the shifts and the slope of the edge of the NEXAFS spectra, the simulations were performed with certain approximations. The main approximation that is traditionally used to calculate absorption spectra are based on the mono-electronic approach, i.e. approximation that involves a single electron excitation. Calculations were performed in the cluster approach in the frame of multiple scattering theory [110], the finite difference method [110] and the linearized augmented planewave (LAPW) method [125].

There are two main challenges when calculating the fine structure of the absorption K-edge using the one-electron approach: first, the calculation of the wave function of electrons in a complex multicenter potential for the polyatomic system and secondly, summing up all final states of photoelectrons in order to define the full ionization cross-section. The second challenge can be solved when using the Green function method.

When talking about the first challenge, this involves solving the three-dimensional Schrödinger equation in a potentially difficult terrain. Although the modern calculating equipment allows solving this challenge straight away (FDMNES code [110], for instance), these massive calculations nevertheless are very time-consuming and not very convenient. Therefore, in order to simplify the task with minimal accuracy losses, the three-dimensional Schrödinger equation or, like in our case, the Dyson equation for the Green function, will be approximated with an equivalent system of algebraic equations. This approximation will be done using the muffin-tin potential.

The muffin-tin approximation is widely used in quantum-mechanic simulations of the electronic band structure in solids and is based on the following principles (Fig.4.7):

- Atoms are surrounded by a spherically-symmetric potential,
- In the interstitial region the potential field is constant.

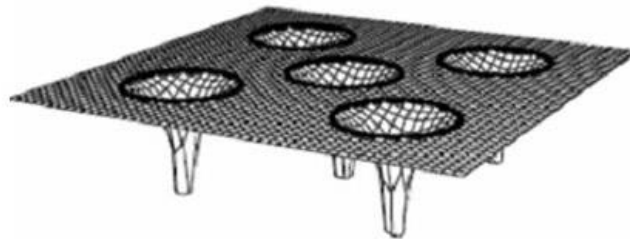


Fig.4.7. Schematic sketch of the potential field used for the muffin-tin approximation [129]

Therefore corresponding *ab initio* calculations using the mono-electronic approach of the FDMNES code were performed. [130], [110] The FDMNES is a user friendly code to simulate X-ray based spectroscopy data, linked to either real absorption (XANES) or resonant scattering (RXD). The FDMNES package uses the functional density theory (DFT) to provide the full relativistic monoelectronic calculations and FDM to solve the Schrödinger equation. However in the frame of this work we decided to limit the real finite difference to multiple scattering calculations. The Green formalism on a muffin tin potential saves computational time and was chosen for efficiency considerations.

#### 4.4. Summary of the chapter

Different experimental techniques were used to characterize chemical and electronic properties of kesterite absorber layers. The surface sensitive XPS and UPS are the main tool to investigate surface of the kesterite absorbers with different  $[S]/([S]+[Se])$  ratio. To look deeper into the material, high energy XPS at the synchrotron was applied. As the excitation energy of the beam is rising, the inelastic mean free path of photoelectrons becomes longer, allowing probing the near-surface region. The conduction band edge was probed using absorption spectroscopy and its special case-NEXAFS. The limitation and sensitivity of the method was discussed.

The effect of the substitution of S with Se atoms was explored using a DFT-based code - *exciting*. The *exciting* code and GW approximation provides the density of states in the conduction band in a good agreement with experimental data.

To better understand what governs the position and shape of the NEXAFS spectra, theoretical methods were used. The simulation package FDMNES –a powerful tool for the absorption edges simulation, allows investigation of the electronic properties of semiconductors.

## 5. Surface electronic and chemical properties of kesterite

In this chapter the surface chemical and electronic properties of kesterite materials with different  $[S]/([S]+[Se])$  ratio will be discussed. We have used laboratory photoelectron spectroscopies as well as synchrotron-based techniques to determine the relative chemical composition of the samples before and after etchings. Also we have studied the changes in the electronic properties of CZTS(e) and compared obtained experimental results with theoretical values available in literature.

### 5.1. Samples with different $[S]/([S]+[Se])$ ratio

Kesterite samples with different anion composition, ranging from pure sulfide to pure selenide, were investigated and described throughout this work. As shown in Chapter 2, absorber layers were made from metallic stack precursors sputtered on soda lime glass with metal ratios of  $[Cu]/([Zn]+[Sn])=0.80$ ,  $[Zn]/[Sn]=1.20$ . After that, the thermal processing of the prepared precursors took place. The reactive thermal annealing was done in the tube furnace in an S and/or Se atmosphere. In addition, elemental Sn was added in to the furnace annealing chamber in order to prevent Sn losses from the precursor. The thermal annealing step is necessary to crystallize the precursors and to form the kesterite phase with the desired  $[S]/([S]+[Se])$  ratios. For more technical details please follow references [31] and [32].

The kesterite absorber layers discussed in this chapter were prepared with different  $[S]/([S]+[Se])$  ratios. Their composition and index numbers are shown in Table 5.1. and will be used in this work to specify a certain sample.

*Table 5.1. Kesterite samples with different  $[S]/([S]+[Se])$  ratios. The number of the sample will be used throughout this document. The precursor cation composition is identical for all samples*

Number	Precursor		Absorber comp. by EDX			Etching
	Cu/(Zn+Sn)	Zn/Sn	Cu/(Zn+Sn)	Zn/Sn	S/(S+Se)	
1	0.8	1.2	0.84	1.18	1	HCl+(NH <sub>4</sub> ) <sub>2</sub> S
2			0.87	1.22	0.95	HCl+(NH <sub>4</sub> ) <sub>2</sub> S
3			0.87	1.27	0.64	HCl+(NH <sub>4</sub> ) <sub>2</sub> S
4			0.89	1.32	0.49	(NH <sub>4</sub> ) <sub>2</sub> S
5			0.85	1.17	0.24	(NH <sub>4</sub> ) <sub>2</sub> S
6			0.82	1.16	0.06	(NH <sub>4</sub> ) <sub>2</sub> S
7			0.81	1.09	0	KMnO <sub>4</sub> /H <sub>2</sub> SO <sub>4</sub> +Na <sub>2</sub> S

It is well known that during the sulfurization/selenization secondary phases can be formed on the surface and deep in the bulk of the absorber layer. The most common unwanted compounds are ZnS, ZnSe,  $\text{Cu}_x\text{S}(\text{Se})$ . They can be rather detrimental for the device performance and it is important to efficiently avoid or remove them. The method for their removal described and studied in this work is the temperature-regulated wet chemical etching. The chemical etching solution dissolves the solid secondary phases from the surface of the sample. In the last column of Table 5.1, the chemical solutions that were used to remove certain secondary phases from the surface of the absorbers, as explained in Chapter 2:

- $\text{HCl} + (\text{NH}_4)_2\text{S}$ .  $\text{HCl}$  removes ZnS secondary phases and  $(\text{NH}_4)_2\text{S}$  removes  $\text{Sn}_x(\text{Se},\text{S})$  [27][28]
- Se-rich CZTSSe:  $(\text{NH}_4)_2\text{S}$  (as above)
- $\text{KMnO}_4/\text{H}_2\text{SO}_4$  oxidises ZnSe secondary phases,  $\text{Na}_2\text{S}$ -solution removes resulting elemental selenium. [29]

To investigate in detail the influence of the chemical etching on the surface chemistry of the kesterite material, absorbers 1 to 7 were examined firstly as-received and secondly after the recommended etching procedures using X-ray based photoelectron spectroscopy. Figures 5.1 and 5.2 shows the set of seven survey spectra obtained from the as-prepared and freshly etched samples.

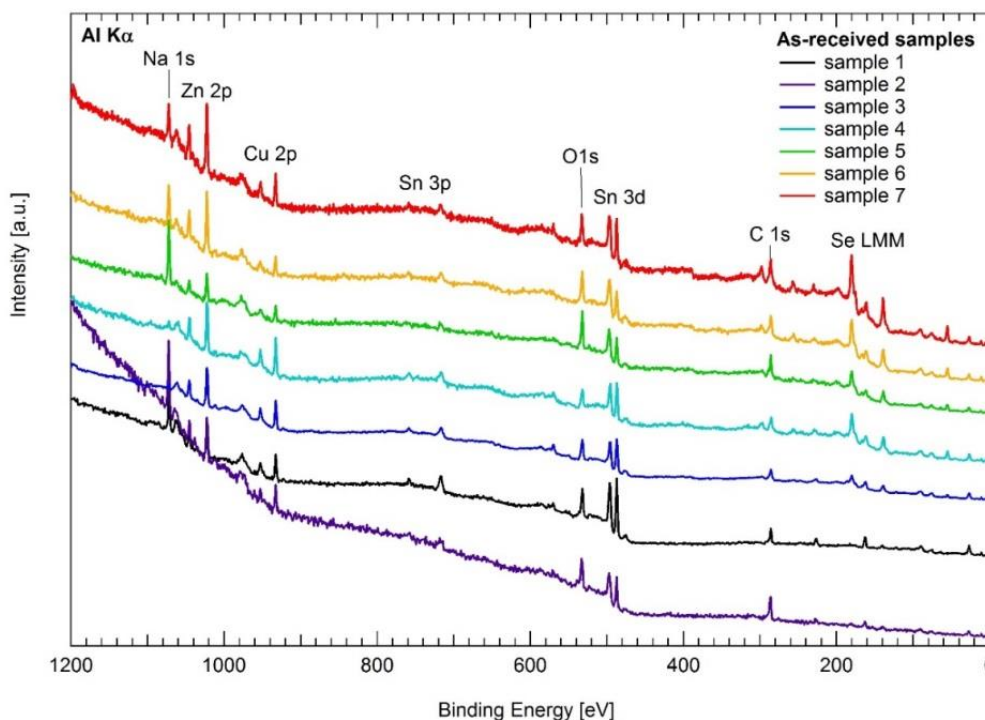


Figure 5.1: XPS overview spectra of the as-received samples (sample 1: pure sulphide, sample 7: pure selenide). Spectra are normalised to the lowest background level and offset on the y-axis. The main photoemission peaks are labelled using the element symbol and energy level of electron origin

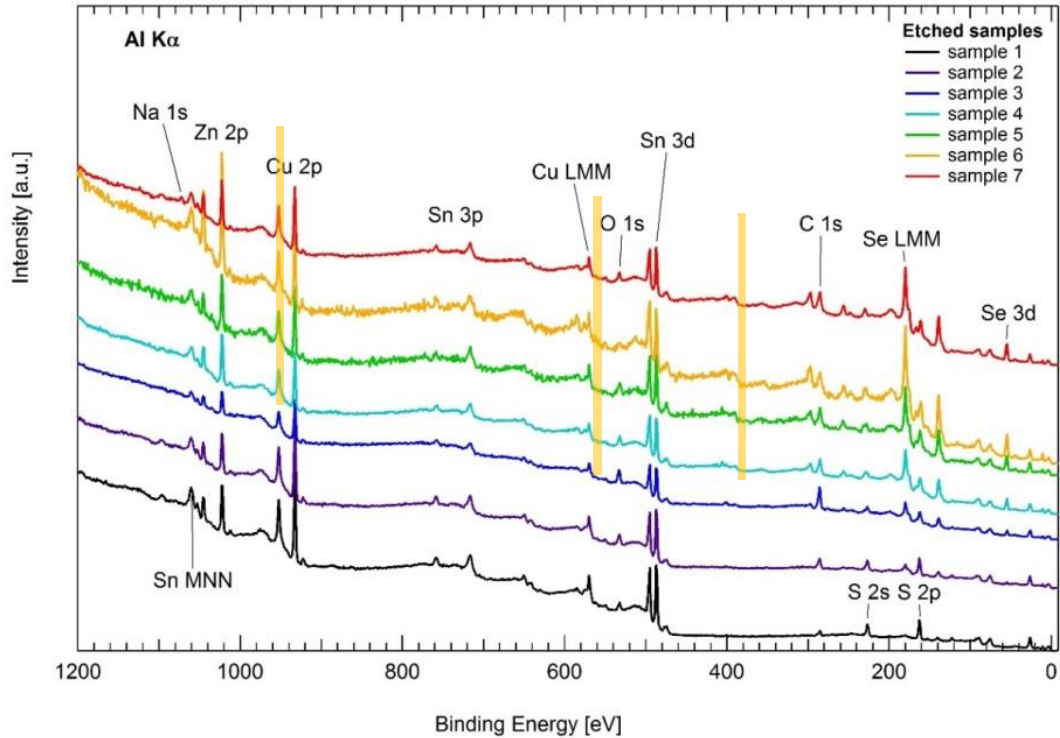


Figure 5.2: XPS overview spectra of the etched samples (sample 1: pure sulphide, sample 7: pure selenide). Spectra are normalised to the lowest background level and offset on the y-axis. The main photoemission peaks are labelled using the element symbol and energy level of electron origin

Spectra are dominated by kesterite related photoelectron peaks which are labeled according to the origin atom and emitting level. All expected elements are identified: Cu, Zn, Sn as well as S and/or S. The pronounced peaks of O, C and Na were also detected and highlighted with the yellow boxes. The intensity of the sodium Na 1s peak varies from sample to sample; it becomes almost invisible for sample 4 and, in contrast, becomes very intense in the spectra of sample 2. Although the preparation of the precursors as well as their thermal annealing and subsequent handling were identical for all samples, the amount of sodium on the surface detected with XPS is different. We know from literature that the sodium is very mobile and diffusive from the soda-containing substrate glass into the absorber of the thin film solar cell. [74], [75] The humidity level inside the storage equipment, the thermal processing conditions of the samples, crystal structure of the absorber layer, and the soda line glass itself influence the diffusion rate of sodium. Details of this process are given in ref. [77]. Results obtained with X-ray based techniques using the CISSY machine are also discussed.

After etching, the intensity of the kesterite-related peaks has grown. Cu- and Sn- peaks become very pronounced, whereas peaks from O and C have drastically dropped, meaning that the surface contamination layer was successfully removed by etching. Sodium peaks are almost invisible or completely gone after dipping samples into the water-based solution that washes Na-containing species away. In the survey spectra, the intensity of Zn has not grown considerably after etching, in comparison to Cu, for instance, although these 2p peaks have very similar kinetic energies and therefore similar mean free path of the emitted photoelectrons in matter. One of the reasons is the removal of unwanted ZnS(e) secondary phases from the surface of the kesterite absorber. The elemental chemical composition of the surface before and after etching is discussed below.

## 5.2. Influence of etching on the surface chemical composition

### 5.2.1. Surface vs bulk $[S]/([S]+[Se])$

The main focus of this work is on the anion variation in the composition of the kesterite absorbers. The  $[S]/([S]+[Se])$  ratio changes from 1 for sample 1 to 0 for sample 7 and was confirmed with the bulk sensitive EDX technique at IREC. In order to study the *surface* anion composition of the absorbers before (Figure 5.3) and after (Figure 5.4) the recommended etchings, the detailed XPS-derived peaks of sulfur and selenium were analyzed. The photoelectron peaks of Se 3p and S 2p are located at the same range of binding energies and both undergo the spin-orbit splitting. The 2p and 3p doublets consist of 1/2 and 3/2 components and therefore at least 4 peaks are visible for the sulfide/selenide mixed samples. The signal/noise ratio also changes before and after etching (Fig.5.4): after etching, the initially noisy spectra are clear and can be used for further quantitative evaluation because an electron attenuating contamination layer was removed.

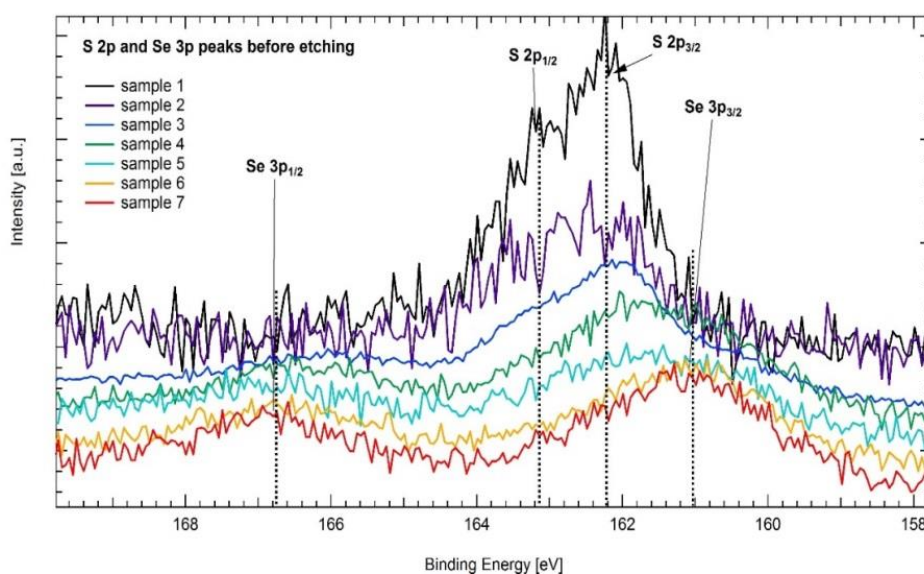


*Figure 5.3: XPS Se 3p and S 2p spectra of the as-received samples (sample 1: pure sulphide, sample 7: pure selenide). Spectra are normalised to the lowest background level and offset on the y-axis. The position of the 4 components is indicated using dashed lines*

The intensity of the S-related peaks grows with the nominal S content in the absorber. The quantitative evaluation of the peaks provides the relative anion composition of the surface. The procedure of the peak evaluation is described in detail in Chapter 4.

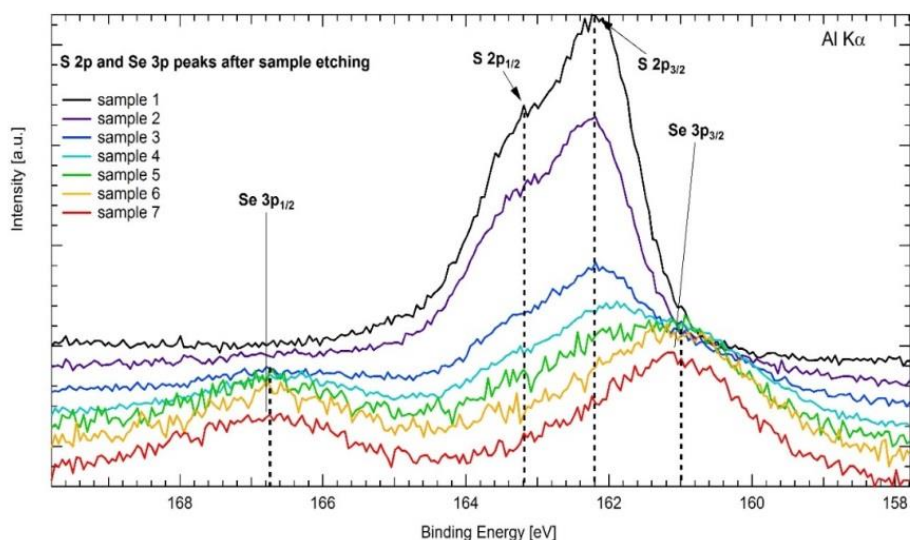


Figure 5.4: XPS Se 3p and S 2p spectra of the etched samples (sample 1: pure sulphide, sample 7: pure selenide). Spectra are normalised to the lowest background level and offset on the y-axis. The position of the 4 components is indicated using dashed lines

Therefore, relative values for the anion compositions of the as-received and etched kesterite surfaces were calculated. Here we have determined a 10% error for the relative composition values obtained with XPS. No error bars are shown for the EDX data because they were not measured by us.

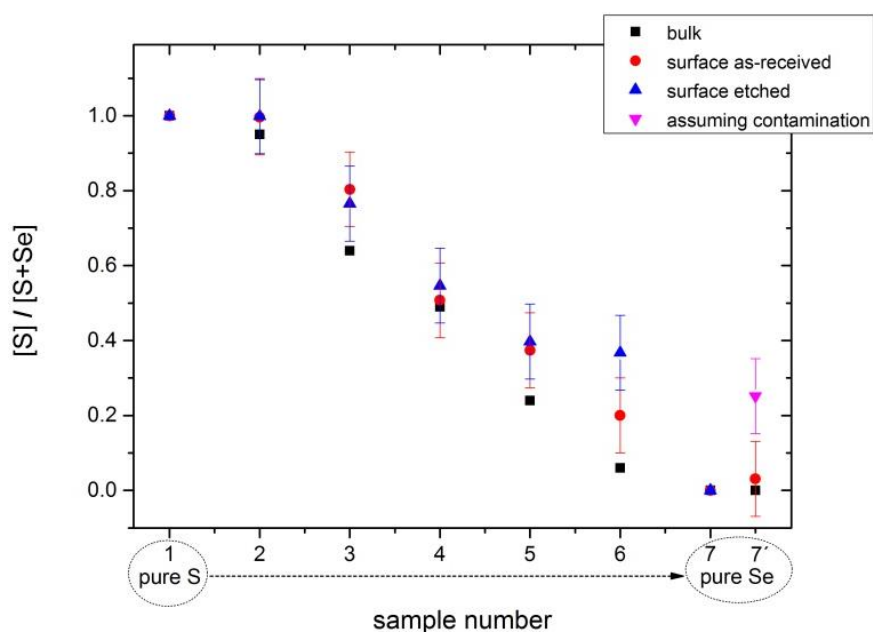


Figure 5.5:  $[S]/([S]+[Se])$  ratios on as-received and etched samples as determined from evaluation of Se 3p and S 2p spectra and EDX of the as-prepared samples. For sample 7, a second fitting procedure was used, assuming a sulfur contamination, resulting in two different results 7 and 7' (see text)

In Figure 5.5 the surface XPS-derived  $[S]/([S]+[Se])$  ratio before and after etching are plotted together with EDX bulk data. The etching procedure alters the few layers of the very surface of the sample; therefore we do not expect the bulk data to change after the applied etchings. And as far as relative  $[S]/([S]+[Se])$  ratios are shown, the samples 1 (pure selenide) and 7 (pure sulfide) are represented in Figure 5.5 with values 1 and 0, respectively.

Sample 2 and 4 show a good agreement between bulk and surface composition before and after etching. However the surface  $[S]/([S]+[Se])$  ratio of samples 3, 5 and 6 before and after etching is considerably higher than the bulk values. This difference in surface and bulk anion composition after etching becomes even more visible for sample 6, probably due to the fact that the  $(NH_4)_2S$  solution has removed  $Sn_xSe$  secondary phases from the surface.

Interestingly, sample 7 seems to have some sulfur on the surface but only after etching. The first attempt to fit the observed Se 3p doublet with one and even with two designed selenium doublets had failed: the residual intensity, where the S 2p peak is normally located, was not covered and the overall fit was not satisfactory (see Figure 5.6, orange boxes highlight the residual intensity that were not fitted with the two Se doublets model). In Figure 5.6 the comparison of the two fitting models is shown. Side *a* shows the results of the Se 3p+ Se 3p doublets model, side *b* Se 3p+S 2p model. The Se 3p+S 2p model successfully fits the experimentally derived peak of samples 7, initially designed as pure selenide one. The relative  $[S]/([S]+[Se])$  ratio of sample 7 was calculated taking some sulfur contamination into account and is shown in figure 5.5 with pink data point “7”.

The origin of the sulfur peak at the surface of the pure selenium sample after etching is not clear yet. It is important to mention that no sulfur was detected with EDX or at the as-received surface with XPS. Therefore, we suggest that the sulfur contamination comes from the etching step itself, namely the last step of the etching procedure for sample 7, which is the dipping it into the  $Na_2S$  solution in order to remove elemental selenium left after the previous oxidation step with  $KMnO_4/H_2SO_4$ . Since the etched sample was rinsed with an ample amount of water, atoms of sulfur left at the surface probably had been incorporated into the surface of the pure-selenide kesterite.

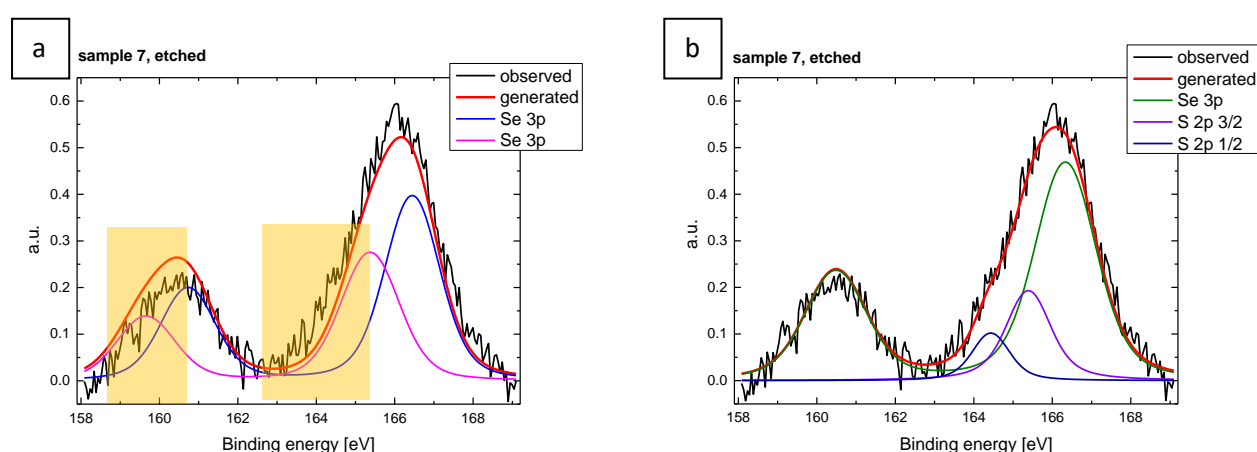


Figure 5.6: fit of the Se 3p spectrum of sample 7 (pure selenide) using a: two Se 3p doublets and b: one Se 3p and an additional S 2p doublet. The areas of poor overlap between data and fit are highlighted orange

## 5.2.2. Cation surface composition

For the further investigation of  $[\text{KMnO}_4/\text{H}_2\text{SO}_4 + \text{Na}_2\text{S}]$  etching of the Se-pure kesterite, we examined the cation composition of the two identical CZTSe samples after two different etching procedures, namely the recommended  $[\text{KMnO}_4/\text{H}_2\text{SO}_4 + \text{Na}_2\text{S}]$  etch and the well-established KCN solution. The influence of the KCN etching step on the Cu-poor and stoichiometric kesterite CZTS surface [78] as well as for the chalcopyrite [79], [80] was already reported. The KCN solution dissolves  $\text{Cu}_{2-x}\text{S}$  secondary phases, and then in addition preferentially removes Cu and to a lesser degree Sn, while the Zn surface content remains unchanged. [78]

In order to better understand the impact of the KCN etching on the surface chemical structure of the pure selenide kesterite, the CZTSe surfaces before and after KCN or  $[\text{KMnO}_4/\text{H}_2\text{SO}_4 + \text{Na}_2\text{S}]$  etchings were examined with XPS. The relative cation ratios were calculated and the obtained results together with EDX derived bulk values are depicted in Figure 5.7.

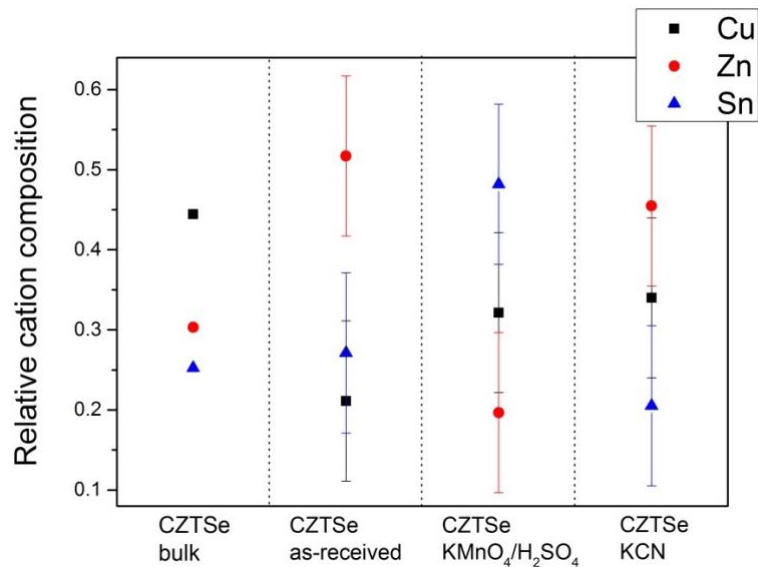


Figure 5.7: relative cation composition of the as-received and etched surfaces of samples 7 as determined from evaluation of XPS-derived spectra and EDX of the as-prepared samples.

The as-received surface of the pure selenium kesterite has shown a higher content of Zn than that of the bulk, probably due to the fact that some ZnSe secondary phases were present on the surface at the first place. After the  $[\text{KMnO}_4/\text{H}_2\text{SO}_4 + \text{Na}_2\text{S}]$  etching the CZTSe sample exhibits a decrease in Zn content, while the Zn content of the KCN etched sample remains almost unchanged in comparison to the as-received surface. Therefore, it was shown that the designed permanganate etching more efficiently removes the ZnSe secondary phase from the surface of Se-pure kesterites than the KCN standard etching step.

The significant difference between surface and bulk *anion* composition of the kesterite absorber layer was already shown, therefore, further investigation of the relative chemical composition of the kesterite samples with different  $[\text{S}]/([\text{S}]+[\text{Se}])$  ratios was driven towards the *metal* surface composition. We calculated the  $[\text{Cu}]/([\text{Zn}+\text{Sn}]$  and  $[\text{Zn}]/[\text{Sn}]$  ratios of seven samples and results are shown in Figures 5.8 and 5.9.

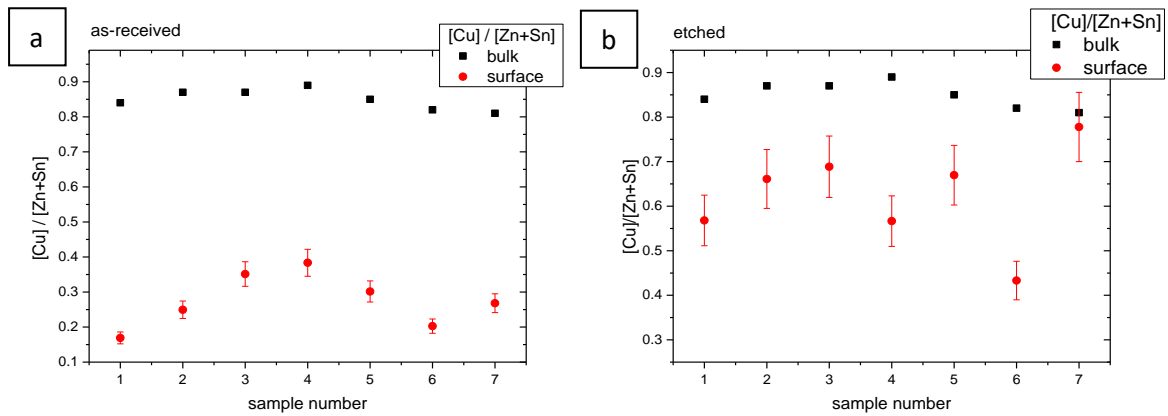


Figure 5.8 a and b:  $[Cu]/([Zn]+[Sn])$  ratios measured on a: as-received and b: etched samples as determined from the evaluation of Cu 2p, Zn 2p and Sn 3d spectra and (both): bulk concentration measured by EDX of the as-prepared samples (sample 1: pure sulphide, sample 7: pure selenide).

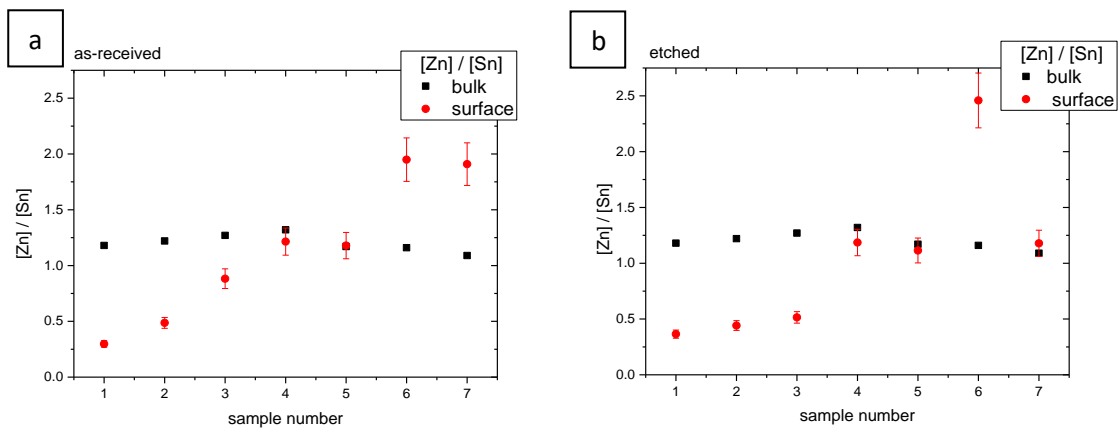


Figure 5.9 a and b:  $[Zn]/[Sn]$  ratios measured on a: as-received and b: etched samples as determined from the evaluation of Zn 2p and Sn 3d spectra and (both): bulk concentration measured by EDX of the as-prepared samples (sample 1: pure sulphide, sample 7: pure selenide).

The seven samples were initially prepared to be Cu-poor; the precursor bulk ratio was chosen as  $[Cu]/[Zn+Sn]=0.8$  (see Table 5.1) as the most favorable cation composition to achieve the highest efficiency (the best kesterite based devices were fabricated in Cu-poor conditions) and to avoid the  $Cu_x(S,Se)$  secondary phase formation. In addition, the XPS study has shown that the kesterite surface is even more Cu-depleted before and after etching. A Cu depleted surface layer was found before for the chalcopyrites [81] and for some kesterite surfaces as well [53]. Moreover, the deviation of the Cu content on the surface from that of the bulk was detected for powder samples grown using a solid-state method.[82] The authors suggest that the Cu poor surface is an intrinsic property of chalcopyrites and kesterites.

The  $[Cu]/[Zn+Sn]$  ratio is shown for each of seven samples before and after etching in Fig. 8 and seems to depend on the sample's number, i.e. the  $[S]/([S]+[Se])$ . The Cu content increases with Se content, reaches its maximum for sample 4, and then decreases back when going towards the pure Se sample. The picture become less clear after the etching was applied. The Cu content in general had relatively increased, probably due to washing away the  $Zn(S,Se)$ ,  $Sn_xSe$  secondary phases from the surface.

The dependence of the [Zn]/[Sn] ratio on the [S]/([S]+[Se]) ratios seems to be more clear (Fig.5.9). The surface Zn content is lower than in bulk for samples 1, 2 and 3 and is reduced even further when etching was applied. This group of samples was etched with HCl that efficiently removes ZnS secondary phases, therefore reducing the amount of Zn on the surface, while keeping Sn unchanged. Samples 4 and 5 were etched with  $(\text{NH}_4)_2\text{S}$  and show good agreement between surface and bulk Zn to Sn ratio. Sample 6 revealed an unusually high Zn content of the surface both before and after etching.

One of the reasons for a such unusually high Zn content on the surface of sample 6 can be the fact that the group of samples 4, 5 and 6 were not etched with HCl and probably because of that do not exhibit Zn depletion on the surface. Meanwhile, sample 7 was already etched with different solutions: potassium permanganate can remove ZnSe compounds and thus reduce the [Zn]/[Sn] ratio, as can be observed in the Figure 5.9b and thus the huge reduction of the Zn content can be explained.

### 5.3. Depth-dependent composition studied by high energy XPS

In order to look deeper into the absorber and better understand the near-surface cation distribution, the samples were examined with different excitation energies in the high energy end-station (HIKE), at KMC-1 beamline at the BESSY II electron storage ring. [83] The excitation energy at HIKE can be tuned from 2.01 keV (close to the energy of a common X-ray laboratory source) up to 12 keV. Therefore the inelastic mean free path (IMFP) of the photoelectrons in matter will be increased from approximately 3 nm to 15nm.

The etched samples 2 and 3 were examined with different excitation energies, the [Zn]/[Sn] ratios were calculated and plotted vs used excitation energies together with bulk EDX-derived values in Fig.5.10. The [Zn]/[Sn] ratio shows a similar behavior for both samples: it increases as the excitation energy increases, becomes highest at 6 keV, drops slightly when  $E_{\text{ex}}=8$  keV. As the excitation energy of the X-rays increases, the IMFP of the photoelectrons also increases, i.e. the information depth of experiment also increases. One could speculate that the near-surface still contains some ZnS secondary phases buried under the very surface and is still visible within the information depth of HIKE. Probably, wet chemical etching can efficiently remove unwanted secondary phases from the superficial layers of the absorber, but not one that lies deeper.

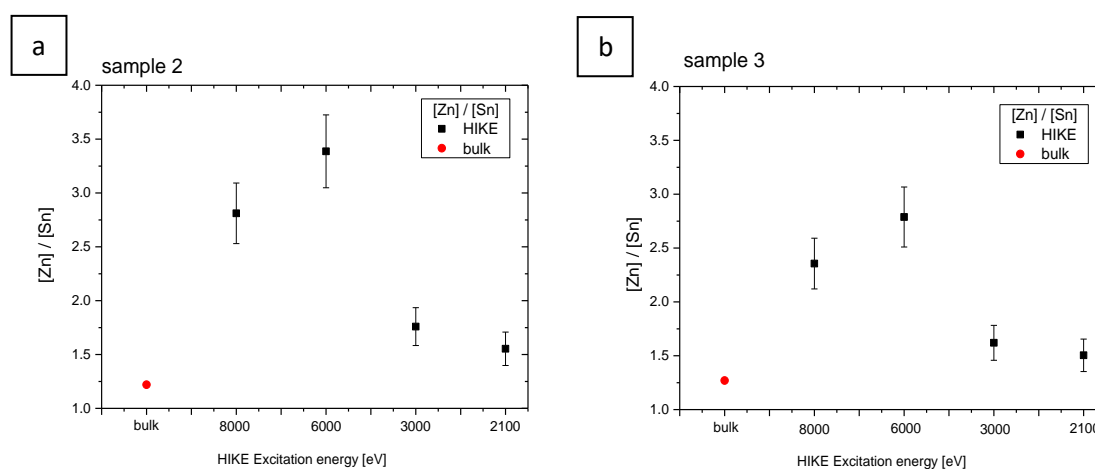


Figure 5.10 a and b: [Zn]/[Sn] ratios measured on a: sample 2 and b: sample 3 as determined from the evaluation of Zn 2p and Sn 3d spectra at different excitation energies from the etched samples and (a and b): bulk concentration of the as-prepared samples measured by EDX

## 5.4. Determination of valence band edges by UPS

The main difference that was stressed in this work is the anion composition of the kesterite samples. As the  $[S]/([S]+[Se])$  ratio changes from 1 to 0, the electrical properties of the respective kesterite compound also changes. Namely the band gap of the absorber layer varies from 1.5 eV for pure sulfide (CZTS) to 1.0 eV for pure selenide (CZTSe). [58], [59] The band alignment of the buffer and respective absorber will also change. However, so far there is still no clear picture how the conduction and valence band change when the  $[S]/([S]+[Se])$  ratio of the kesterite alters. According to theoretical calculation [58] the shift in band gap is due to both conduction and valence bands variations. See chapter 3 for more theoretical details.

The set of seven samples with different  $[S]/([S]+[Se])$  ratios were used to study the dependence of the position of the valence band maximum (VBM) relative to the Fermi level distance on the sulfur content of mixed kesterites. For that, freshly etched kesterite absorbers were measured using UPS with an excitation energy of 21.2 eV of He I radiation. The obtained spectra were referenced to the Fermi level of the clean gold sample and plotted in Fig. 5.11.

In order to find the VBM of the samples, the leading edge of each spectrum was extrapolated linearly to the baseline; the point of intersection determines the VBM position of the respective absorber. Due to the non-linearity of the edges of the valence band spectra, it is often not possible to draw the extrapolating line precisely enough. Using the graphical method of the VBM determination we estimate the error margin for the VBM values of 0.1 eV.

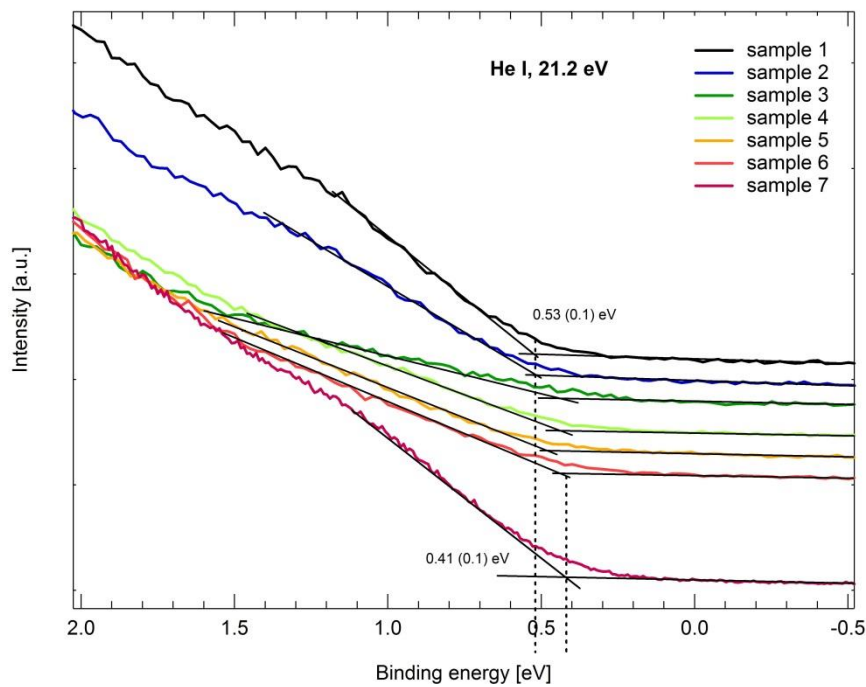


Figure 5.11: Valence band maxima determined for all samples after etching. The leading edges of the valence band curves are extrapolated linearly and the intersection with the base line is taken as the value for the VBM

Only a small change in the VBM to  $E_F$  distance when going from pure sulphide to pure selenide kesterite was found: the  $VBM_{CZTS}$  is  $0.53 \pm 0.1$  eV and  $VBM_{CZTSe}$  is  $0.41 \pm 0.1$  eV, meaning the transition from slightly inversed CZTS surface to a weak p-type CZTSe semiconductor. Therefore, the shift of 0.12 eV in valance band edge was found. These results are consistent with others reported so far in literature, for instance [55].

The difference in band gap  $\Delta E_g = 0.5$  eV, when going from CZTS to CZTSe, is only *partially* covered with a valance band shift of 0.12 eV. There could be several reasons for that. First of all, DFT calculation, mentioned above, has predicted a shift of 0.15 eV in valance band, i.e. only a small part of the band gap change is due to the shift in valance band.

Secondly, the UPS measurements described here are very surface sensitive and therefore depict the electronic properties of the top monolayers of kesterite that can deviate from the bulk. The Cu-depleted surface phase determines the VBM and doesn't represent fully the bulk properties of kesterite material. In addition, the applied etching also changes the surface composition, as was shown earlier, and thus influences the measured VBM values. In addition, recent theoretical DOS calculations have shown that the valance band maximum of the intrinsic CZTS consists of antibonding Cu-d and S-p states. [6] One can speculate that the very Cu-depleted kesterite surface can lack the "necessary" Cu-d related states to form a valance band edge and therefore the shift in the VBM is observed. The complexity of the surface cation composition altered by the chemical etchings has a straightforward correlation with electronic surface properties of kesterite.

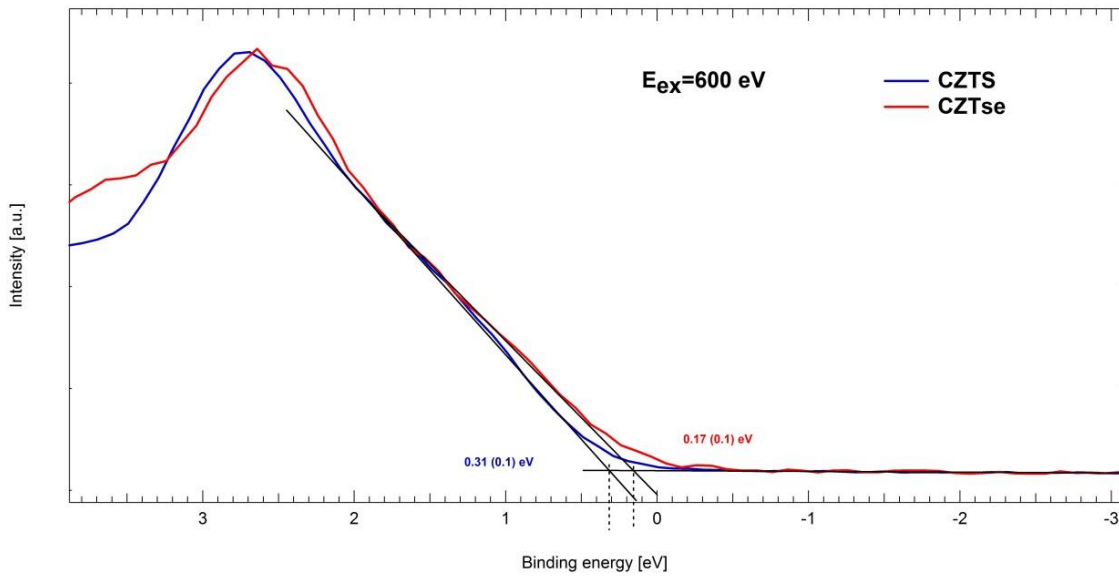
#### 5.4.1. The valance band edge study by high energy synchrotron radiation

So far, we have determined the Fermi level to VBM distance for the seven kesterite samples with the different  $[S]/([S]+[Se])$  ratio using UPS with a laboratory helium lamp as an excitation source with  $E_{ex} = 21.2$  eV. A valance band edge shift of  $0.12 \pm 0.1$  eV was obtained.

Further investigation of the shift of the VBM was conducted using synchrotron radiation at BESSY II. The CISSY machine was moved to the electron storage ring and attached to the beamline with  $E_{ex}$  ranging from 80 up to 2100 eV. That allows obtaining spectra with different information depth in the kesterite absorber. Due to limited time of the experiment at BESSY, we have focused ourselves on two different kesterite samples, namely pure sulfide CZTS and pure selenide CZTSe, assuming that the effect of our interest still would be possible to observed.

Freshly etched CZTS and CZTSe samples were examined and spectra obtained at  $E_{ex} = 600$  eV and 80 eV are plotted in Fig.5.12. The relative shift of the VBM when going from pure sulfide to pure selenide kesterite composition is found  $\Delta = 0.14 \pm 0.1$  eV at  $E_{ex} = 600$  eV and  $0.16 \pm 0.1$  eV at  $E_{ex} = 80$  eV. The wide range of different excitation energies were used to measure the shift in the VBM and obtained results are summarized in the Table 5.2 together with the previously found value using He I lamp. The relative shift of the VBM doesn't show a clear dependence on the excitation energy of the X-ray beam. Thus, the found values deviate from 0.12 up to  $0.16 \pm 0.1$  eV.

a



b

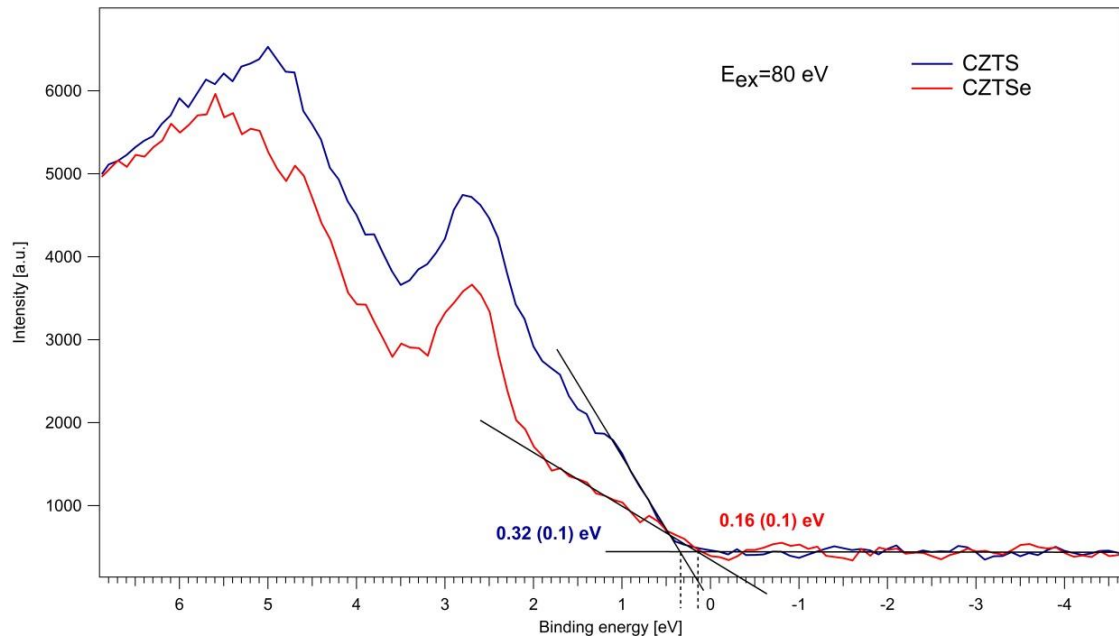


Fig.5.12. Valence band edge spectra of CZTS (blue) and CZTSe (red) samples, measured at (a)  $E_{ex}=600$  eV and (b)  $E_{ex}=80$  eV at synchrotron BESSY II, Adlershof

Table 5.2. The relative shift of the VBM when going from pure sulphide to pure selenide kesterite composition measured at different excitation energies

Excitation energy (eV)	Relative shift, eV
21.2	$0.13 \pm 0.1$
80	$0.16 \pm 0.1$
600	$0.14 \pm 0.1$
1000	$0.12 \pm 0.1$
1300	$0.15 \pm 0.1$
2100	$0.13 \pm 0.1$

As was said, the usage of different excitation energies allows probing the material surface at different penetration depths. The dependence of the inelastic mean free path (IMFP) of the photoelectrons in matter on the excitation energy is known as the universal curve. The excitation energy of the conventional laboratory UPS ( $E_{\text{ex}}=21.2$  eV) is equal to the probing depth of approximately 2-3 monolayers of the studied surface, where 1 monolayer  $\sim 0.3$  nm. The curve has its minimum at around 50-80 eV and at lower excitation energy the mean free path of the excited photoelectrons increases again. The reason for that is the low energy photoelectron has not enough energy to excite the plasmons, which are the main scattering mechanism in solids. In other words, the probability of the inelastic scattering of the photoelectrons decreases with lower excitation energies and therefore the IMFP increases.

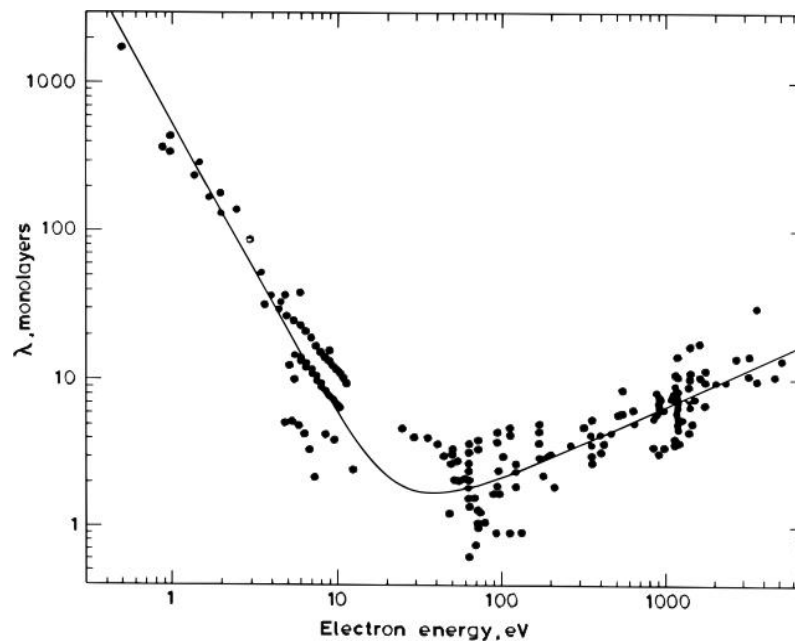


Fig.5.13. The universal curve of the electron mean free path vs its electron kinetic energy [96]

The slight deviation of the  $\Delta$ VBM found using synchrotron radiation, could be due to the fact that different excitation energies result in different penetration depths of the emitted electrons and thus, in different probed sample depths. The  $E_{\text{ex}}=80$  eV will be the most surface-sensitive, while energies of 1300 and 2100 eV will probe already the near-surface region. The differences in the chemical composition of the surface and near-surface regions were already discussed in the previous sub-chapter. The unavoidable contamination of the sample surface with adsorbed molecules of water and  $\text{CO}_2$  can attenuate the signal coming from the surface and alter the final results.

Thus, we have performed several experiment at different end stations at BESSY to probe the edges of the valance band of kesterites and can conclude, that the shift of VBM is reproducible for a wide range of excitation energies. The shift of the VBM due to the changes in the anion composition of the kesterite deviates from  $0.12 \pm 0,1$  up to  $0.16 \pm 0,1$  eV. The usage of different excitation energies allows probing the near surface region of kesterite and avoiding the surface effects, such as dangling bonds and surface charging.

## 5.5. Band line-up with CdS buffer layer

The band alignment between absorber and buffer layer plays an important role and has a big impact on the final device performance. Therefore we have calculated the band offsets with the most common buffer material, CdS. In order to monitor the changes happening during the interface formation, a stepwise deposition of the CdS was performed.

The ultrathin CdS layer sample is very important in these experiments because it allows monitoring the junction formation, differentiating between band bending and chemical shift of photoelectron peaks. Since the ultrathin CdS layer is thin enough still to “see” the absorber, i.e. to detect the emission from the underlying kesterite absorber, photoelectron peaks of Cu and Sn were measured before and after the CdS deposition. If a shift in the binding energies of the core levels was detected and valid for both Cu  $2p_{3/2}$  and Sn  $3d_{5/2}$  peaks, one could distinguish the bend bending at the kesterite/CdS interface from the chemical shift commonly seen during the CBD process. The Sn  $3d_{5/2}$  peak is shown in Fig. 5.12 measured for the etched kesterite CZTS surface 7 (sample 1 from Table 5.1), then with ultrathin and with thick CdS layer deposited on top of etched kesterite layer.

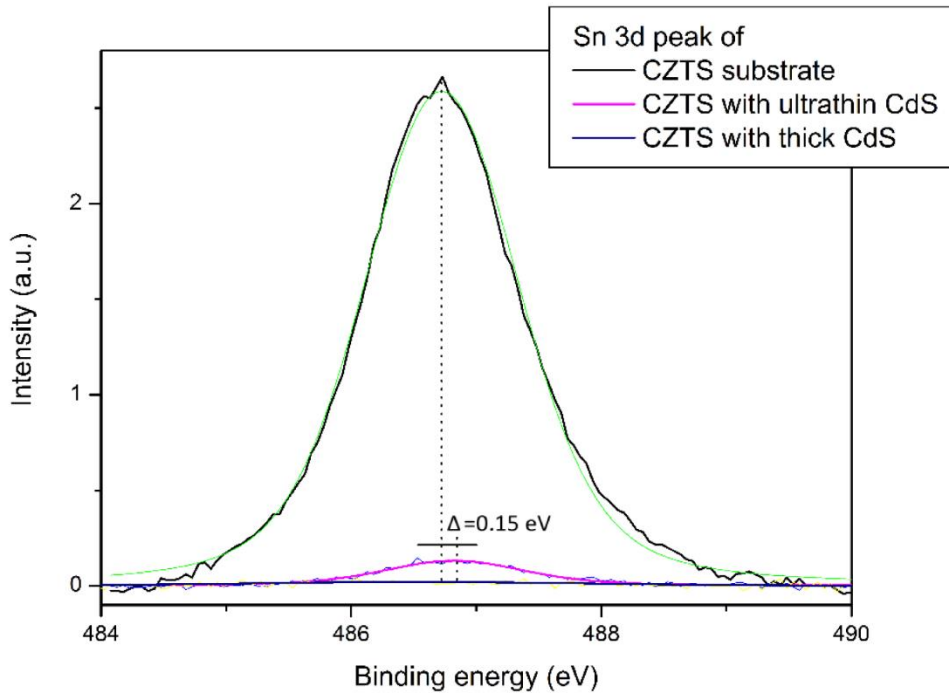


Figure 5.12: Sn  $3d_{5/2}$  peak of the etched kesterite substrate, after deposition of thin and thick CdS layers

A small shift of 0.15 eV in the Sn  $3d_{5/2}$  peak position was found already after the thin buffer layer deposition. The value of the shift was confirmed with other measurements of Cu $2p_{3/2}$  peaks for the same sample. Therefore, the bend bending value of 0.15 eV will be used to calculate the band alignment between CZTS and CdS. A similar procedure was used to probe the CZTSe/CdS interface and to measure the value of bend bending with sample 7.

The valance band spectrum of the thick CdS was measured with UPS (not shown) and, using the graphical method explained above, the VBM for the buffer material was obtained and the CBO for two combinations of kesterite samples (pure sulfide and pure selenide) and CdS buffer was calculated.

The obtained band alignment diagrams are shown in Figure 5.13. The cliff-like offsets are found for both cases: a large offset of  $-0.62\pm 0.1$  eV for CZTS and a smaller cliff of  $-0.34\pm 0.1$  eV for CZTSe.

The cliff-like CBO was found previously by other groups but the value of the offset was smaller ( $-0.32\pm 0.02$  eV) [54].

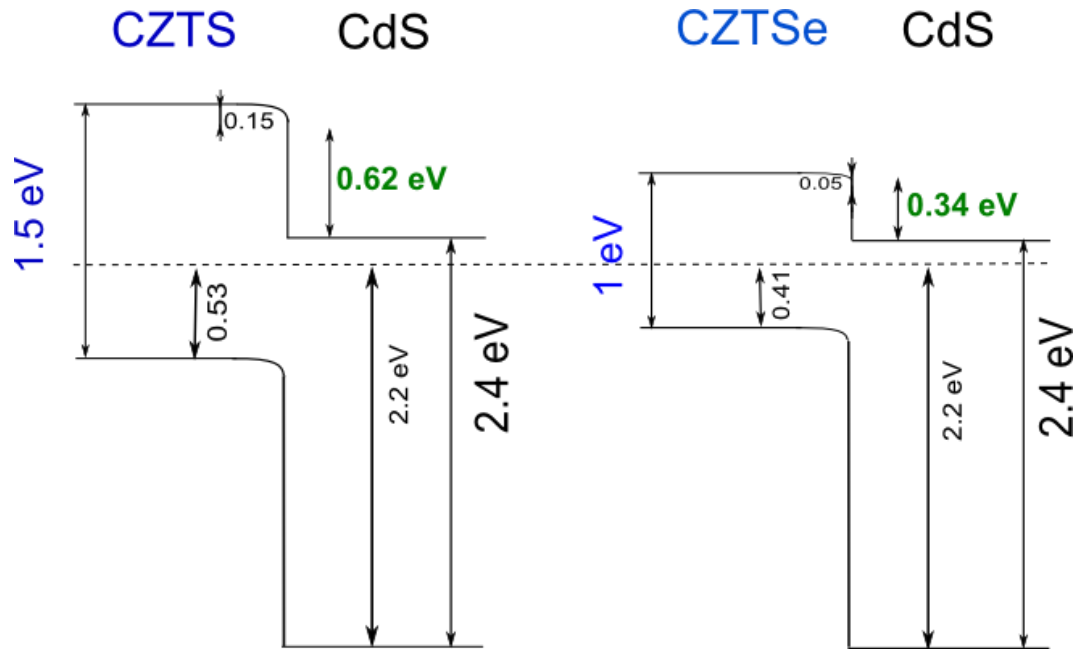


Figure 5.13: band offsets between CZTS and CZTSe and CdS buffer layer calculated using VBM values from UPS measurements shown in figure 11

### 5.5.1. Influence of the CdS deposition method

It has been shown that the band alignment between kesterite and CdS is “cliff”-like (negative  $\Delta E_c$ ) for all  $[S]/([S]+[Se])$ -ratios. That means that the CBM of the absorber lies below the CBM of the buffer, which can cause a loss in open circuit voltage ( $V_{oc}$ ). In contrast, the optimum absorber/buffer alignment would be the so-called “spike”-like alignment. Then the loss in  $V_{oc}$  can be minimized due to reduction of recombination at the interface. However, a too large spike can become a barrier for electrons and cause a drop in the short circuit current ( $J_{sc}$ ) and efficiency. [84]

The band alignments presented in the previous section now can be correlated with the performance of the respective devices, finished and measured at IREC. The efficiency of complete devices was varying with changing  $[S]/([S]+[Se])$ -ratio; the values are presented in detail in Table 5.2 along with other device parameters. Therefore, the idea of tuning the band gap of the absorber via the  $[S]/([S]+[Se])$ -ratio in order to achieve the best line-up with the CdS buffer layer, can be straightforwardly implemented and compared with theoretical and complementary experimental results.

The efficiencies of the devices provided in Table 5.2 steadily grow as the sulfur content in the kesterite absorber increases, and reach a maximum value of  $Eff=3.4\%$  and  $V_{oc}=341$  mV for sample number 5. The band gap of sample 5 was estimated to be  $E_g=1.12$  and the  $[S]/([S]+[Se])=0.24$ .

Interestingly, the record CZTSSe device had an anion ratio  $[S]/([S]+[Se])=0.2\pm 0.1$  and a band gap of 1.13 eV [55]. Samples 1 to 6 were annealed at similar thermal conditions in an atmosphere of elemental S and/or Se, Sn.

*Table 5.2: Kesterite samples with different  $[S]/([S]+[Se])$  ratios: parameters of the device performance*

Number	Name	S/(S+Se)	$E_g$ (eV) From EQE	Jsc (mA/cm <sup>2</sup> )	Voc (mV)	FF (%)	Eff. (%)
1	Dpk240314-2	1	1.61	8.9	201	33.1	0.6
2	Dpk200314-1	0.95	1.53	14.9	359	41.6	2.2
3	Dpk200314-2	0.64	1.36	16.7	330	49.4	2.7
4	Dpk200314-3	0.49	1.26	15.4	298	44.8	2.1
5	Dpk210314-1	0.24	1.12	22.6	341	44.5	3.4
6	Dpk210314-2	0.06	1.05	4.1	156	25.1	0.2
7	Dpk250314-1	0	1.07	27.4	326	45.8	4.1

Sample 7 (pure selenide) has the highest efficiency in the presented set of samples, and there is no obvious explanation for this fact. One of the reasons could be different thermal processing history of the pure selenide sample or the more favourable band alignment between absorber and deposited buffer. So far there is no straight explanation for this finding based only of the concept of the favourable/non-favourable band alignment on the absorber/buffer interface.

According to the literature, the band alignment of the kesterite/buffer junction depends not only on the band gap of the absorber (i.e. sulfur/selenium content) but also on the CdS deposition method [55], [85]. In order to investigate this question, the thick and ultrathin CdS layer samples were prepared at IREC, following the same recipe as the CdS used in solar cells shown in Table 2.

This set of experiments were done using synchrotron radiation from the electron storage ring BESSY II in Berlin, Adlershof with an excitation energy of  $E_{ex}=1300$  eV. The CdS samples, prepared at IREC, together with the freshly etched CZTS and CZTSe absorbers, were measured at identical conditions. The VBM found in this experiment vary from the value found previously in the CISSY laboratory:  $VBM(CdS_{IREC})=1,75$  eV,  $VBM(CZTS)=0,49$  eV and  $VBM(CZTSe)=0,35$  eV. Since the energy distance between core levels and valence band maximum is a material constant, the valence band offset  $\Delta E_V$  can be calculated from the energy difference between the core levels of absorber (CZTS or CZTSe) and buffer material (CdS), which is observed in the course of interface formation. [85] The obtained VBM were used to calculate the conduction band offset and band alignment diagram for pure sulfide and pure selenide samples with CdS buffers prepared at IREC (Fig.5.14).

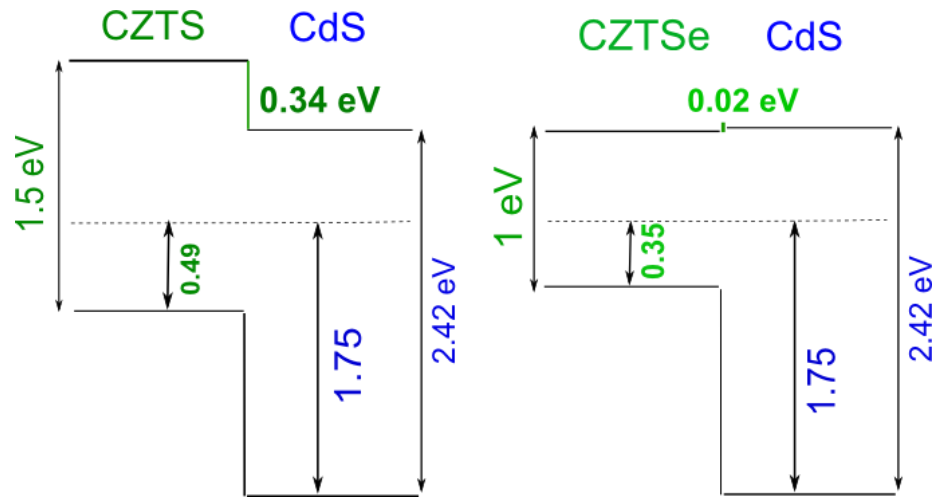


Figure 5.14: band offsets between CZTS , CZTSe and CdS buffer layer, prepared in IREC. The band alignment is calculated using VBM values from synchrotron measurements using 1300 eV excitation energy (spectra are not shown)

These band offsets were obtained using slightly different excitation energies  $E_{ex}=1300\text{eV}$  then those presented in the previous section (Fig.5.13) where an Al  $K\alpha$  laboratory X-ray source was used ( $E_{ex}=1486.6\text{ eV}$ ), yet provide comparable results. The VBM obtained using synchrotron radiation slightly deviates from the results obtained in laboratory for both, kesterite absorbers and CdS layers. Thus, a negative offset of  $-0.34\pm 0.1\text{ eV}$  was found for CZTS and a positive offset of  $0.02\pm 0.1\text{ eV}$  for a CZTSe absorber with differently prepared CdS buffer.

A strong influence of the CdS deposition method on the band absorber/buffer alignment has been observed. The data shown for the VBM and CB offsets can be used to design the junction between kesterite substrate layers with different  $[S]/([S]+[Se])$  ratio and n-type buffer materials like CdS.

### 5.5.2. Post deposition low temperature annealing of kesterite absorbers

The recent studies by Xie et al. as well as Sardashti et.al. of the post low temperature treatment (PLTT) of kesterite absorbers have shown that an annealing step before the CdS buffer deposition can strongly influence the final device performance. [77], [87] It was shown that the PLTT of pure selenide kesterite absorbers results in Cu-poor grain surfaces, beneficially passivated with  $\text{Sn}_x\text{O}$ . [87] Another study confirmed these previously mentioned results. The  $200^\circ\text{C}$  PLTT of CTZSe samples has improved the efficiency of the respective devices and the observed effect was attributed to the Cu-poor, Zn-rich grain surfaces. The low temperature annealing of the complete devices was studied as well: changes at the interface and in the efficiency of the respective devices were observed. [87], [88] The formation of a semi-epitaxial layer at the CdS/CZTS interface and a change of the ITO resistivity was reported.

Lastly, the spatial distribution of Na at the CdS/CZTS interface was studied in detail by Xie et al. [77] Freshly prepared absorbers with Cu/(Zn+Sn) ratios of around 0.75-0.8, Zn/Sn varying from 1.18-1.22, and  $[S]/([S]+[Se])=0.3$  were annealed at a temperature ranging from 150°C to 400°C under 1 bar N<sub>2</sub> atmosphere for 1 h. The mentioned kesterite absorber samples were prepared by IREC following the same procedure as described in chapter 3. To complete the kesterite devices, annealed absorbers were etched with 22% w/w (NH<sub>4</sub>)<sub>2</sub>S solution followed with a chemical bath deposition of 20 nm CdS and DC sputtering (Alliance CT100) of 350 nm i-ZnO/ITO window layer. [77]

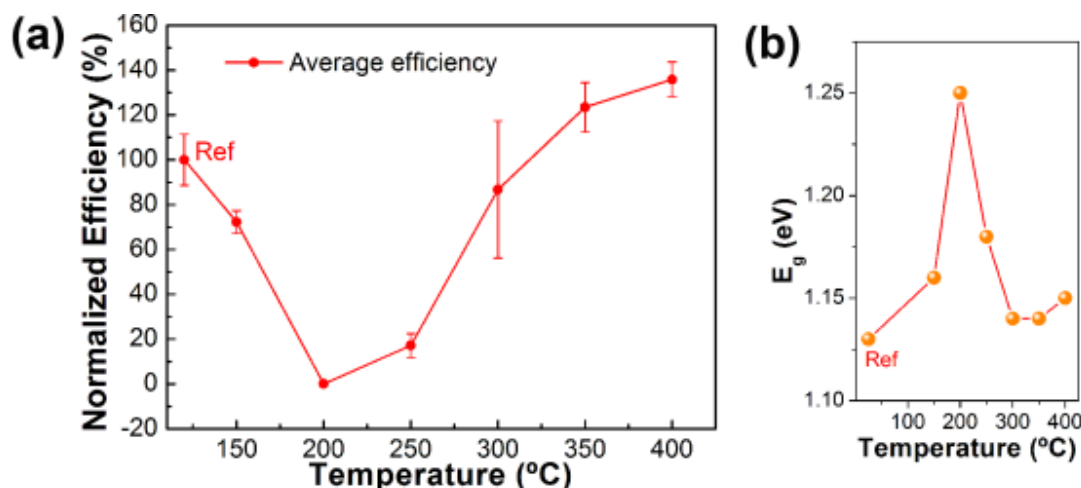


Fig.5.15. The normalized efficiencies (a) and band gap values (b) as a function of the applied temperatures of the PLTT [77]

Fig. 5.15 shows the dependence of the device parameters such as normalized efficiency (a) and band gap values (b) on temperature used in the PLTT process. After the annealing of the CZTSSe absorber at 200°C, the efficiency of the respective device dropped drastically and was fully recovered or even slightly improved after a post treatment at 400°C (Fig. 5.15 a) The evolution of the E<sub>g</sub> value during the low temperature treatment is shown in Fig 15 b: the band gap of the kesterite absorbers grows and reaches its maximum of 1.25 eV at 200°C, and steadily decreases up to 1.15 eV as the temperature value reaches 400°C. Nevertheless, the band gap value remains slightly larger for the high temperatures of 300°C and 400 °C in comparison with E<sub>g</sub>=1.13 eV of the reference sample.

In order to better understand the influence of the PLTT on the final device performance, kesterite samples were studied using photoelectron-based spectroscopy. The influence of the low temperature annealing on the chemical and electronic surface properties of the kesterite absorber itself and, as a consequence, on the band alignment between absorber and CdS, was investigated at the KMC-1 beamline at the electron storage ring BESSY II Berlin (Germany). It is important to stress that only kesterite *absorber* samples were annealed at the elevated temperatures, not the complete p-n junction and therefore Cd inter-diffusion phenomena were out of the experimental focus. In contrast, we have concentrated on the high temperature annealing effect on the electronic properties of the bare CZTSSe, namely the VBM position before and after 1 hour annealing at 200°C or at 400°C.

Samples I and II are CZTSSe absorbers with identical cation and anion compositions. The main difference of these two samples is the thermal treatment applied after the etching step. Sample I was heated up to 400°C for 1h, and sample II up to 200°C 1h independently from each other.

First, freshly etched (see Table 5.1 for etching procedures) CZTSSe absorbers were measured to determine the relative surface cation composition as well as VBM values under the reference conditions using the excitation energy of 3000 eV at the HIKE end station. The high temperature annealing was performed in vacuum ( $10^{-8}$ - $10^{-9}$  mbar), avoiding surface oxidation and contamination. The subsequent measurements of samples I and II were performed without breaking the vacuum. The obtained data were used to calculate the relative surface composition. (Fig.5.16 a and b) and the CBO at the interface with the CdS buffer (Fig.5.17).

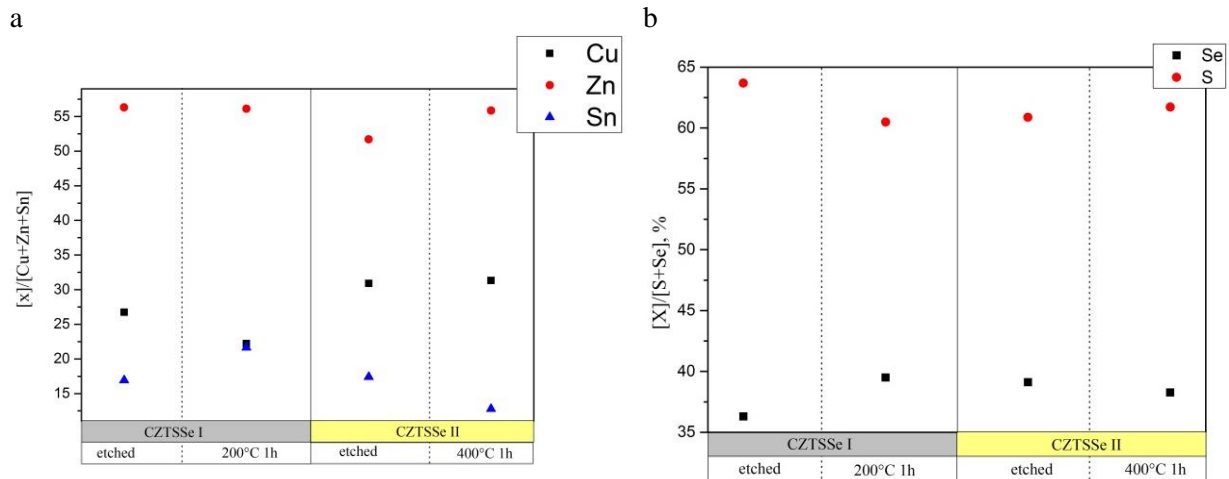


Fig.5.16. The relative cation composition (a) and relative anion composition (b) calculated for samples I and II before (etched) and after LPTT at under 200°C and 400°C

The observed variations in the device performance can be due to different reasons. One of them is the Cu re-distribution, as suggested by Sardashti et.al. [87] As was already mentioned, the Cu-poor grain and absorber surfaces can be beneficial for the cell efficiency. [87] Another effect is the  $E_g$  variation observed from EQE curves by IREC that can be attributed to the Cu-Zn order-disorder. [89] So far there is no agreement in literature on the effect of the order-disorder on optoelectronic properties of kesterite. Rey et al. [91][91] suggest that  $Cu_{Zn}$  and  $Zn_{Cu}$  defects don't limit the cell efficiency. On the other hand, a decrease in disorder can increase the band gap and  $V_{oc}$  values and therefore the efficiency. [92] In the present case, the observed relation between a band gap value of the re-annealed absorber and an efficiency of the respective device is in contrast harmful, i.e the increase in a band gap leads to decline in performance.

The variations in the surface cation and anion composition are shown in Fig.5.16 a and b. During the annealing process at 200°C, the Zn content of sample I remains almost unchanged, while Cu concentrations go down and Sn, in contrast, rises. The surface composition of sample II, annealed at 400°C, is initially slightly Zn poorer than sample I. After the thermal treatment is applied, the Zn concentration of sample II reaches the same value as detected for sample I. Meanwhile, the Cu concentration of sample II remains the same and the Sn concentration decreases after annealing. Only minor deviations in the anion composition of the studied absorbers were observed (Fig.5.16 b). The surface of sample I undergoes a bigger change than sample I: the surface becomes Se-rich and S-

poorer after annealing, and in contrast, the anion surface composition of sample II remains almost unchanged, a small increase in S and drop in Se contents are detected.

The observed deviations in the cation and anion concentrations might not fully describe a strong drop in the efficiency after the 200°C step. The Cu-poor and Sn-rich surface of sample I after annealing might be beneficial for the device performance, according to [87] and kesterite absorbers with composition ratios ranging from Zn/Sn=0,6-3,3 and Cu/Sn=0,7-1,9 were reported to result in highly efficient kesterite solar cells. [93][94]

Another reason for the drop in the efficiency of 200°C annealed sample can be the changes in the electronic surface properties of the kesterite absorbers. The VBM measured before and after the annealing step, together with band gap values (measured at IREC) were used to calculate the CBO (Fig.5.17). The VBM of CdS was taken from the previous experiment, mentioned in the preceding section, due to the fact that no changes in the CdS deposition method were made since that time.

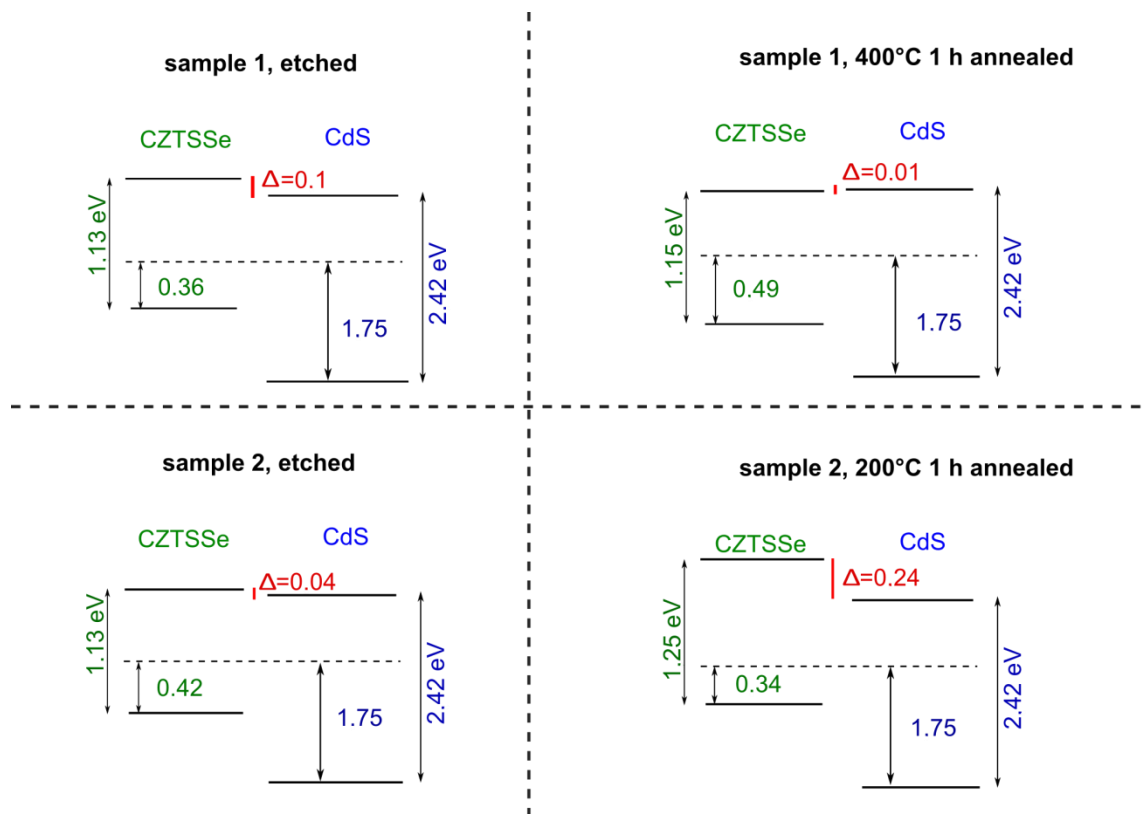


Figure 5.17: band offsets between CZTSSe and CdS buffer layer. High temperature annealing of the bare CZTSSe absorbers was done at 200°C and 400°C, respectively, without CdS deposited on top, following the cell preparation procedure

The sample I was annealed at under 400°C and the VBM to  $E_F$  distance had increased from 0.36 to 0.49 eV, as well as  $E_g$  from 1.13 to 1.15 eV. Therefore, the CBO has changed from -0.1 eV to almost flat band conditions after the annealing step. The electronic properties of sample II after the lower temperature treatment (namely 200°C) had also undergone several changes: the VBM position shifted from 0.42 to 0.34 eV and  $E_g$  increased from 1.13 to 1.25 eV before and after annealing respectively. The CBO of sample II evolved from -0.04 eV to -0.24 eV negative offsets.

Interestingly, there is an obvious influence of the PLTT on the  $E_g$  value - the difference of 0.12 eV can be significant for the interface diagram. Furthermore, the UPS measurements had shown that the valance band edge was influenced by the PLTT too: the trend towards smaller values was observed for the lower temperature, while higher temperature brought the  $E_F$  closer to the CBM. On the whole, taking into account both, VBM and  $E_g$  alterations, the CBO was *improved* from a small cliff of -0.1 eV to a tiny spike of +0.01 eV in case of the 400 °C annealing step. And in contrast - setting a temperature to a lower value of 200°C had a *detrimental* effect on the band alignment: the small cliff of -0.04 eV increased to a bigger one of -0.24 eV.

With a full picture of the calculated band line-up on the absorber/buffer interface, the influence of the temperature treatment of the absorber on the final device performance can be explained. The drop in the efficiency of the device based on the kesterite absorber annealed at 200°C can be correlated with an worsened negative offset from -0.04 to -0.24 eV. The recovery of the efficiency after increasing the annealing temperature to 400°C can be due to the band line-up development at the interface: a cliff of -0.1 eV was turned in to a positive spike of +0.01 eV.

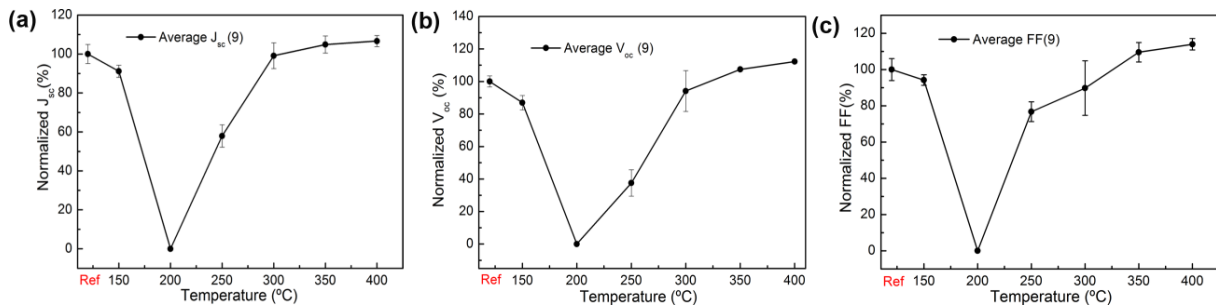


Fig 5.18. The normalised  $J_{sc}$  (a),  $V_{oc}$  (b), FF (c) values as a function of used temperature of the PLTT process. [22]

In addition to the data shown in Fig.5.18, the dependence of different optoelectronic parameters on temperature used for the post treatment is presented. The clear drop at 200°C in the intensity of all presented characteristics are visible: normalized  $J_{sc}$ ,  $V_{oc}$  and FF undergo a drastic decline and were recovered by about 110% for  $J_{sc}$  and about 120% for  $V_{oc}$  and FF in comparison to the reference sample.

Summing up, so far we can only speculate about the reasons that limit the kesterite-based devices. According to theoretical calculations performed by [95], the favourable band alignment at the kesterite/CdS interface can vary significantly. The influence of the CBO on the device output was studied and it was shown that the  $\Delta E_c$  can vary from 0.0 up to 0.5 eV spike and surprisingly no negative influence on the carrier transport was found. Nevertheless, we would like to conclude that the device performance can be limited not only by the band alignment at the buffer/absorber interface, but also by other factors such recombination in the deep bulk of kesterite absorber and/or presence of secondary phases at the Mo back contact/absorber interface. Therefore, the detailed insight on the deep defects in the bulk may be valuable.

## 5.6. Summary of the chapter

In chapter 5 the surface chemical and electronic properties of kesterite absorbers with different  $[S]/([S]+[Se])$  ratio were studied using XPS and UPS as well as high energy XPS. Depending on the anion composition, specific etching procedures were applied to remove secondary phases. The quantitative elemental analysis has shown that the as-received surface composition of samples deviates from the bulk and from the nominal composition of the precursor. The surface composition deviates even more after the etching due to selective removal of the segregated secondary phases from the surface. For instance, the  $[S]/([S]+[Se])$  ratio increased after etching was applied in comparison to the as-received surfaces, especially for Se-rich samples, probably due to selective removal of  $Sn_xSe$  with  $(NH_4)_2S$ . Thus the ratio of  $[S]/([S]+[Se])$  changed from approximately 22% up to 40% for a sample with a bulk composition of 6%. Moreover on the surface of the initially Se-pure sample a low S signal was detected that can originate from the S atoms incorporated in to the kesterite surface after the final etching step in  $Na_2S$  solution. The deviation in the cation composition before and after etching was also observed. A Cu-poor surface was found for all samples in addition to the fact that sample were grown under Cu-poor conditions to avoid formation of the detrimental  $Cu_x(S,Se)$  secondary phases. Efficient removal of ZnS by  $(NH_4)_2S$  and ZnSe by complex oxidizing etching with  $KMnO_4/H_2SO_4$  followed by a  $Na_2S$ -solution from the surface of kesterite samples was proven.

It is known that the changes in the anion composition cause the changes in the electronic properties of kesterite material, namely the band gap of sulfur pure kesterite is 1.5 eV while selenium pure material  $E_g=1$  eV. But what is the exact change of the band position upon change of the anion composition? According to the theoretical calculations, the difference of 0.5 eV is not evenly distributed between the conduction and valence bands shifts. To shed light on this phenomenon, the detailed investigation of the relative positions of the VBM to  $E_F$  was done using UPS and the results are shown in Chapter 5. Seven samples with  $[S]/([S]+[Se])$  ratio ranging from 1 to 0 were analysed and a shift of  $-0.12\pm 0.1$  eV was found which is in a good agreement with theoretical values reported previously. Further investigations of the VBM shift have been done at the synchrotron BESSY II using different excitation energies allowing probing the near-surface region of kesterite samples. The shift of around  $-0.12\pm 0.1$  eV was reproduced at a wide range of  $E_{ex}$ , supporting the found values under laboratory conditions.

In the second part of the Chapter 5, the band alignment with cadmium sulphide-one of the most common buffer layer materials-has been studied. For long time there was no agreement on the band alignment in system kesterite/CdS. Some authors had reported cliff-like alignment of  $-0.3\pm 0.1$  eV at the CdS/CZTS interface [54], while other group of researcher had published a cliff-like offset for all kesterite samples with  $[S]/([S]+[Se])=1; 0.45; 0$ . The CBO they found were  $+0.41; +0.48; +0.48$  eV, respectively. [55] Therefore we decided to hunt down this question and investigate ourselves the band alignment on kesterite/ CdS interface. For that proposes, CBD CdS was deposited on the top of kesterite sample and the electronic properties of the buffer layer were investigated with UPS. The found  $VBM_{CdS}=2.2\pm 0.1$  eV indicates an n-type, high doping level of the semiconductor. Using the found VBM for CdS, the band alignments with CZTS and CZTSe were calculated. *Cliff-like offsets* were observed with both CZTS and CZTSe-based junctions:  $-0.62$  and  $-0.34\pm 0.1$  eV respectively. Interestingly, the CBD CdS prepared by IREC and measured at synchrotron BESSY II revealed a

different VBM to  $E_F$  distance, namely  $1.75 \pm 0.1$  eV. Here the offsets with kesterite absorbers were more favourable:  $-0.34$  *cliff* with CZTS, and  $+0.02 \pm 0.1$  eV *spike* with CZTSe.

Band alignments derived with a purely experimental approach can be correlated with the known efficiencies and other cell parameters of the completed devices provided by IREC. The efficiencies of the cells steadily increase as the content of Se increases and reach 3.4% for sample number 5 with  $[S]/([S]+[Se])=0.24$ . The band gap of the absorber was estimated to be  $E_g=1.12$ , which is in a good agreement with the band gap of the record devices reported in literature.

It is interesting to note that the efficiency of the devices can be influenced by the thermal treatment of the absorbers prior to the buffer deposition. [77],[87]As absorber layers were annealed at  $200^\circ\text{C}$  the efficiency of devices dropped to nearly 0% along with a huge decrease of the other cell parameters. Surprisingly, the efficiency were recovered or even slightly improved after annealing at  $400^\circ\text{C}$ . The temperature ranging between  $150^\circ\text{C}$  up to  $400^\circ\text{C}$  were discussed in literature, therefore we examined the effect of low temperature annealing on the electronic and chemical surface properties of kesterite?

To investigate this problem, the CZTSSe samples with  $[S]/([S]+[Se])=0.3$  were annealed at  $200^\circ\text{C}$  and  $400^\circ\text{C}$ . The relative surface composition and the VBM to  $E_F$  distance were measured before and after thermal treatment and the modifications were observed after usage of both temperatures. Slight changes in chemical cation and anion composition were observed that don't fully explain the huge drop in the efficiency after annealing at  $200^\circ\text{C}$ . To illustrate the effect of annealing on the electronic properties of kesterite, we have calculated the band offsets at the CZTSSe/CdS interface. We have seen negative  $-0.24$  eV cliff offset at CZTSSe annealed at  $200^\circ\text{C}$  and CdS interface and in contrary a  $+0.01$  positive spike in case of CZTSSe annealed at  $400^\circ\text{C}$ . Therefore, a drop in efficiency can be explained due to an unfavourable cliff-like alignment at the absorber/buffer interface after annealing at  $200^\circ\text{C}$ , and a recovery of the efficiency after usage of higher temperature owing now to better alignment –a small cliff of  $+0.01$  eV. However, a drop to almost 0 can't be explained by any of the observed changes in the kesterite properties.



## 6. Conduction band edges of kesterite absorbers with different $[S]/([S]+[Se])$ ratios

In this chapter the development of the conduction band edge due to the changes in the chemical composition will be discussed. As going from pure sulfide to pure selenide composition, a shift in CBM of  $0.35\pm 0.1$  eV is predicted by theoretical calculations. We decided to probe the CB edge using experimental approach first. Results of absorption spectroscopy will be further on compared with calculated values using simulation software.

### 6.1. NEXAFS experiments of CZTS and CZTSe absorbers

The information about the band offsets between the absorber and buffer layer is crucial for the understanding of their influence on the output of the final cell. While the VB offsets were already determined with such established methods as UPS and XPS, the position of the CB is more difficult to obtain. The usual approximation is based on the assumption that the CBM is the VBM plus the band gap energy  $E_g$ . However, as was already discussed in the previous chapter, the surface differs a lot from the bulk in its chemical and electronic properties and therefore the determination of the surface band gap can be more challenging, since  $E_g$  is determined using optical methods that are bulk sensitive.

We focused on probing the position of the conduction band and its relative shift when going from CZTS to CZTSe composition using NEXAFS. For that, bare absorbers of  $\text{Cu}_2\text{ZnSnS}_4$  (sample 1) and  $\text{Cu}_2\text{ZnSnSe}_4$  (sample 7) were etched with respective solutions (see Table 2.1.) to remove unwanted ZnS(e) and SnS(e) secondary phases. After that, samples were loaded into the vacuum chamber ( $\sim 10^{-9}$  mbar) shortly after etching and no subsequent sputtering or other surface treatments were applied to clean them.

Since kesterite thin films often contain secondary phases, single-phase reference materials were measured to confirm the obtained results.

#### 6.1.1. Off-stoichiometric kesterite powder samples

Off-stoichiometric kesterite powder samples with different anion composition were used as references for the NEXAFS experiments. Since the composition of the powdered samples as well as secondary phase impurities were precisely identified, together with the crystal structure and defect types – such samples can be used as a reference for the NEXAFS experiments. The powder samples were provided by the group of Prof. Schorr, HZB, prepared by PhD students Laura Elisa Valle Rios and Kai Neldner

via a solid state reaction process and all technical details are given in the reference. [97] The list of the used powder samples is given in Table 6.1. No secondary phases were detected in the CZTSe samples, while CZTS powder samples contain some  $\text{Cu}_x\text{S}$ . The compositions of the powder samples are given by the formulae in the second column of Table 6.1. and were obtained by measuring wavelength-dispersive X-ray spectroscopy (WDX). The composition of the kesterite type phase can be therefore independently identified from the composition of the secondary phases, i.e. differentiating between kesterite and  $\text{Cu}_x\text{S}$  phase. In case of thin film absorbers, the overall composition of the sample is obtained with XRF and in this case the kesterite and secondary phases are measured together and an average composition of the thin film will be given.

*Table 6.1. Stoichiometric powder samples used as references for the NEXAFS measurements (data provided via personal communications)*

Sample number	Composition (WDX)	Comments
1	$\text{Cu}_{1.985}\text{Zn}_{1.053}\text{Sn}_{0.978}\text{Se}_4$	No secondary phases detected
2	$\text{Cu}_{2.307}\text{Zn}_{0.705}\text{Sn}_{1.071}\text{S}_4$	$\text{Cu}_{0.92}\text{S}$ (2.95%), $\text{Cu}_{2-x}\text{S}$ (1.16%)

### 6.1.2. NEXAFS spectra at BESSY II

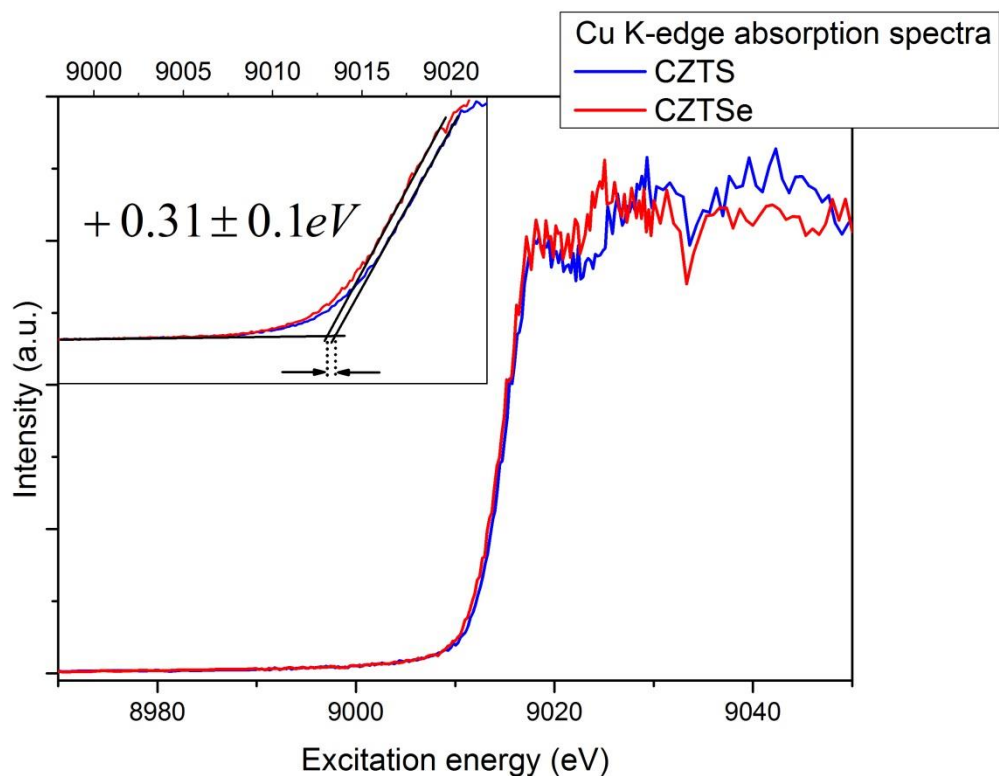
NEXAFS-spectra were measured at the BESSY II synchrotron in Berlin, Adlershof. The absorption at the Cu and Zn L-edges was measured using soft X-rays (900-1500 eV) at the Russian-German beam line (RGLB) and detected using sample current (total electron yield). The sample current detection mode is surface sensitive, similarly to XPS, where the information depth depends on the kinetic energy of electrons emitted from the sample surface.

The hard X-rays (3000-10,000 eV) were used to obtain the Cu and Zn K-edges as well as the Sn L-edge at the KMC-1 beam line with the HIKE end station with a Bruker fluorescence detector. The fluorescence mode is considered as a bulk sensitive detection mode (information depth of several micrometers). It requires sophisticated detectors and has a limited count rate. However, in fluorescence mode different samples can be probed- diluted, thin ( $\leq 2 \mu\text{m}$ ) or non-uniform samples. The thin film solar cell absorbers and powder samples on the carbon tape substrate are suitable for this experiment.

In Fig.6.1 the obtained absorption spectra for Cu K (a) and Zn L-edges (b) are shown. Additionally, Zn K-, Cu and Sn L-edges are shown in the appendix. The excitation energy scale has an error up to several eV depending on the energy, but the positions of the absorption spectra are correct relative to each other with a very small error. That is possible due to the fact that the set of experiments for the each of absorption spectrum have been done under similar conditions for both samples: CZTS and CZTSe. Thus, the experimental setting of the Russian-German beam line and on the total electron yield recording system was the same for each set of edges, namely Cu, Zn and Sn-L<sub>3</sub>. K-edges of Cu and Zn were measured at the HIKE endstation in the fluorescence mode and in this case the absorption losses at the KMC-1 beam line and the backlash of the monochromator were taken into account. Therefore, we can talk about the *relative* shifts between the respective absorption edges measured for CZTS and CZTSe.

Thus we can correlate shifts between the edges as a shift in the CBM when changing the kesterite composition. [73] In addition, the detailed XPS spectra of Cu  $2p_{3/2}$  didn't reveal a shift of binding energies when going from CZTS to CZTSe (not shown), thus the corresponding Cu  $L_3$  absorption edge positions represent the real energy difference between the core levels and the final states of electrons in the conduction band.

a



b

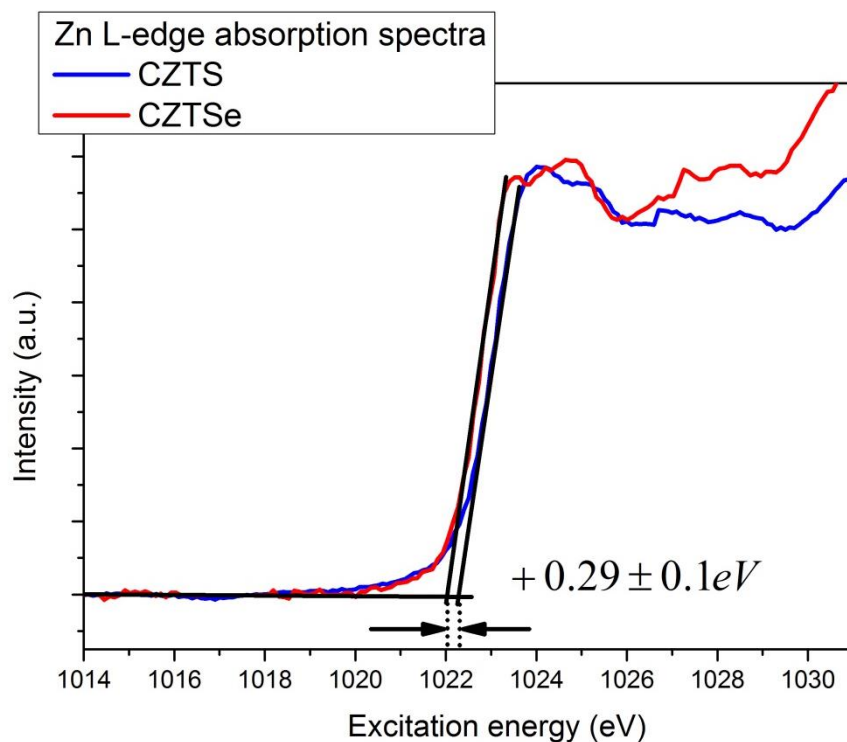


*Fig.6.1. Absorption edges of a) Cu K, b) Zn L from CZTS and CZTSe. The position of the absorption edges is correct relative to each other; therefore the shifts in the spectra correspond to the relative real energy shifts in the conduction band edge (see the text for details).*

There are different methods in literature for the determination of the absorption edge position on the energy scale. First, one can fit the position of the crest of the curve just after the edge [98], second, extrapolation of the edge to the base line [99], [100], third, the first derivative method. [101][101] In the present study, the energetic position of the absorption edge is determined as the point of intersection of the linear extrapolation of the leading edge of the absorption edge and the baseline, similarly to the method of VBM determination.

The statistical error of our experiments is defined by the reproducibility of the excitation energy provided by the monochromator. To ensure that the observed shifts between the absorption spectra is due to the effect of the changing the anion composition of the kesterite, the non-reproducibility of the monochromator has to be excluded.

B.Johnson [6] has shown that the mirror current measured together with the respective absorption edge can be used to relatively calibrate the measured absorption edge. The shifts in the mirror current curves matched the shifts in the respective absorption spectra, thus ensuring an energy scale to be true for all spectra of the specific edge. [6] Based on the several measurements of the same edge, the error bars were set at  $\pm 0.1$  eV for the accuracy of the energy scale determination.

In the experiments presented here, the statistical error was set to  $\pm 0.1$  eV due to the observed reproducibility of the measured spectra. In addition, our observations were confirmed by the known accuracy of the monochromator at the used beam line. For example, using the Si 111 monochromator crystal at the KMC-1 beam line the results measured at high energies of 8-9 keV were obtained with a statistical error of 0.1-0.2 eV. The resolution at such high energies is usually quite low:  $\pm 0.8$ -2.5 eV for HIKE using the Si 111 crystal. Nevertheless, such a poor resolution causes only a broadening of the spectral features, but not a shift, which is crucial for our experiments. Thus, due to a high reproducibility of the excitation energies, we fixed the statistical error to  $\pm 0.1$  eV for the determined shifts of the absorption spectra at the relative scale of the energies.

All spectra measured for CZTS and CZTSe, coupled respectively, display a shift between them. The value of the shift deviates slightly from  $0.29 \pm 0.1$  eV for the Zn K and L-edges up to  $+0.32 \pm 0.1$  eV for the Sn L-edge when going from selenide to sulfide. All obtained spectra and shifts between the spectra for polycrystalline and powder samples are shown in the Table 6.2.

*Table 6.2. Relative shifts between the absorption edges measured for CZTS and CZTSe thin film polycrystalline samples (positive shifts mean higher photon energy). Results of this work*

<b>Absorption edge</b>	<b>Relative shift (eV)</b>
Cu K-edge	$+0.31 \pm 0.1$
Zn K-edge	$+0.29 \pm 0.1$
Cu L-edge	$+0.30 \pm 0.1$
Zn L-edge	$+0.29 \pm 0.1$
Sn L-edge	$+0.32 \pm 0.1$

*Table 6.3. Relative shift between the absorption edges measured for CZTS and CZTSe stoichiometric powdered reference samples. Results of this work*

Absorption edge	Relative shift (eV)
Cu K-edge	+0.29±0.1
Zn K-edge	+0.28±0.1
Sn L-edge	+0.30±0.1

The observed shifts were preliminarily attributed to the shifts in the probed states in the conduction band due to replacing S with Se.

However, the shift in the absorption edge itself doesn't contain information about which level undergo the shifts when the anion composition of kesterite is changed. The shift can be due to both, the core level or the conduction band state. The true meaning of the shift in the absorption edge became clear after the corresponding core levels for the CZTS and CZTSe samples were obtained and compared in couples. The Cu 2p<sub>3/2</sub> and 1s, Zn 2p<sub>3/2</sub> and 1s, Sn 2p<sub>3/2</sub> core levels were obtained for two different samples, CZTS and CZTSe. After the calibration, each type of the core level peaks was coupled in pairs so that the position of the peak maximum can be compared. No shift between the mentioned core levels measured for pure selenide and sulfide samples was noticed. Therefore, we conclude that the shifts seen in the position of the NEXAFS spectra measured for pure sulfide and selenide samples are due to shifts in the LDOS in the conduction band, and not due to the chemical shift of the core levels, which might have been caused by the changes in the anion composition of the kesterite.

Therefore, we conclude that the exchange of S by Se in the kesterite structure influences the electronic levels of the material. The changes at the atomic level when going from S to Se cause the changes in the macroscopic material properties, such as electronic and crystal structure. The evidence for these changes is the shift in the absorption spectra. According to B. Johnson et al [73], it became clear that in order to understand the evolution of electronic structure of kesterites several absorption edges need to be measured. Therefore, changes in the density of states in the conduction band of selenide and sulfide kesterites have been investigated in detail using the DFT approach and the results will be shown in the following sub-chapter.

For the present, we can deduce that the exchange of S with bigger Se atoms causes the expansion of the bond lengths in the crystal structure resulting in a material with different electronic properties. [102] The stretching of the bonds lengths unavoidably influences the local density of the nearest neighbor atoms. This atomic-scale change of the electronic properties leads to global changes in the electronic properties of the kesterite: the band structure of kesterite changes, namely the conduction and valence band edges shifts and thus resulting in a selenide kesterite with a lower band gap than that of sulfide.[102] This difference is also represented in the shift between the absorption spectra measured for CZTS and CZTSe and have been correlated with shift in CBM.

### 6.1.3. Fine structure of the Cu L<sub>3</sub> absorption edge

Among the measured absorption edges, the shape of the Cu L-edge needs to be discussed in detail due to the occurrence of pre-edge features (Fig. 6.2).The Cu L-edge can be separated in two parts: the onset of the edge in the energy window of 931-934 eV and the fine structure after the absorption edge itself at energies of 934-940 eV. In some literature sources the pre-edge features on the Cu L<sub>3</sub> spectra are attributed to Cu species like CuO or CuS on the sample surface. [103] These phases contain Cu<sup>2+</sup> instead of Cu<sup>+</sup> with a partially unfilled 3d band that will bring pre-edge features to the resulting spectra. The energy necessary to excite an electron to the unfilled 3d orbitals is slightly lower than the

energy gap to the conduction band edge and therefore the resulting spectra will have a peak before the actual absorption edge. Even a small amount of this phase on the surface of the probed samples or maybe in between the grain boundaries will contribute to the spectrum, according to M. Grioni et al [103] and R. Bacewicz et al. [103]

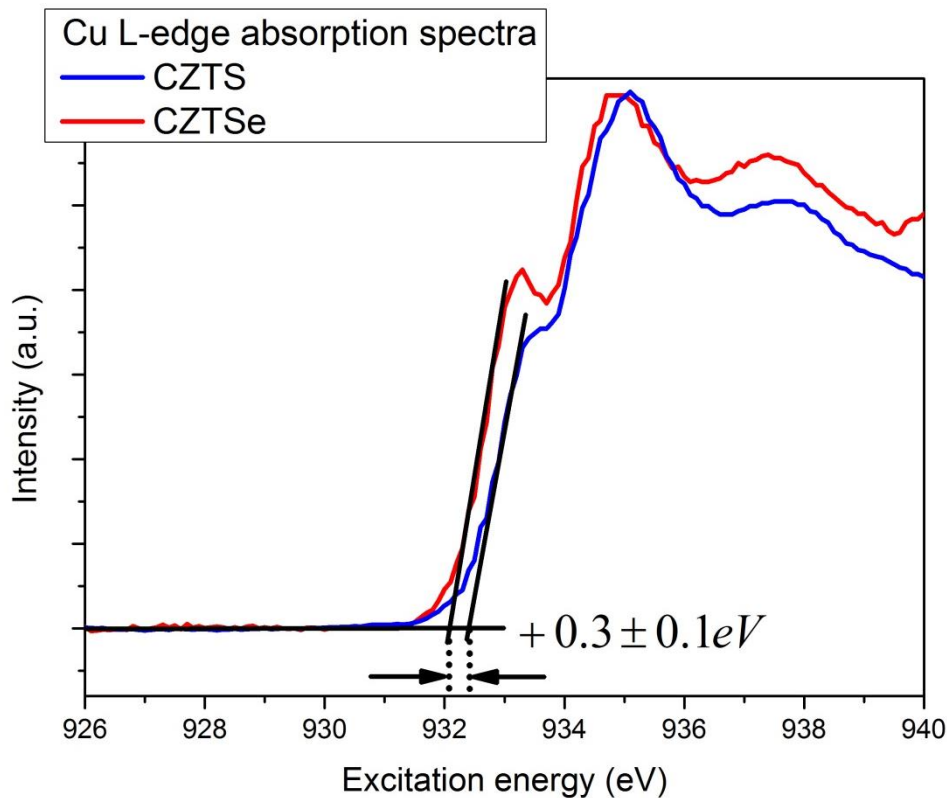


Fig.6.2. Absorption edges of Cu  $L_3$  obtained for CZTS (blue) and CZTSe (red).

In the present work, the Cu L-edge seems to have such a pre-peak structure at 931-934 eV and one can attribute it to the oxide layer containing CuO on the top of the probed sample. Nevertheless, we have assigned this structure as an absorption edge itself due to its high intensity, relatively high energy range and its shape. We have compared obtained spectra with absorption edges of Cu-containing material presented in literature. Some of these spectra indeed contain the pre-edge peaks that in the end were attributed to the CuO species on the surface. But the intensities of all CuO-pre-peaks are considerably lower than the actual absorption edge. [6]

Interestingly, that CuO-pre-structure is separated from the absorption edge by several eV. This pre-edge structure appears at energies 930-932 eV with different intensity, i.e. essentially lower than the absorption edge itself, which is not the case for the Cu  $L_3$  edge measured in CZTS and CZTSe systems. The measured spectra have a continuous, non-interrupted shape without distinct peaks at excitation energies lower than absorption edge.

And lastly, references [103] and [102] suggest that the observed shape of the Cu  $L_3$  edge is original for the chalcopyrites  $\text{CuFeS}_2$ ,  $\text{Cu}_5\text{FeS}_4$  and other Cu-containing material such as  $\text{Cu}_{1.8}\text{S}$ ,  $\text{CuS}$ .

Thus the relative shift between Cu L<sub>3</sub> absorption edge spectra measure for CZTS and CZTSe systems was calculated using the onset at 932-933 eV and attributed as the absorption edge of the kesterite material.

#### 6.1.4. Discussion of the NEXAFS spectra. Limitations of the method

As was mentioned previously, the main task of the NEXAFS measurements is to determine the energy of the CBM.

$$E_{\text{edge}} - E_B = E_C - E_F$$

where  $E_{\text{edge}}$  is the energy of the absorption edge,  $E_B$ - binding energy of the excited core electron, core level to Fermi level,  $E_C$ - CBM to Fermi level distance,  $E_F$ - Fermi level.

In reality NEXAFS contains information about the partial density of states in the conduction band seen by the already excited electron. The energy of the measured absorption edge corresponds to the energy difference between the excited core level and the first unoccupied allowed states in the conduction band. However, we don't know for sure if this state is the conduction band edge as "seen" by the electron in a solar cell.

In PV devices, the electrons are being excited from the valance into the conduction band. In contrast, probing kesterite samples with a high-energy X-ray beam causes excitation of the deep core electrons. Therefore, the absorption spectroscopy results should be carefully interpreted and compared with data obtained with other experimental techniques. The NEXAFS derived data can underestimate the core level to CBM distance due to the possible exciton formation, which can shift the onset of the absorption edge to lower energies. An absorption edge shows the energy difference between the initial state (core level) and the final state in the conduction band in the excited state of the material. Thus, after the photon absorption, the attraction between the core hole and excited electron in CB can contract this energetic distance and it will appear smaller than in the ground state of the material. [73]

The photoelectron spectroscopies, such as XPS and UPS don't prompt the creation of the exciton. Here, the excited photoelectron is expected to be in the vacuum level, and considered as "free electron". Similarly inverse photoelectron spectroscopy (IPES) is also usually applied to probe the CBM with electrons with well-defined energies which do not interact with core levels.

Therefore, the NEXAFS data can be interpreted in a meaningful way, taking into account the limitations of the method. The shifts in the obtained Cu and Zn K- and L-edges, as well as Sn L-edges will be discussed in following section.

Firstly, a NEXAFS spectrum contains information about the partial density of states (pDOS) seen by the excited atom. The local density of states (LDOS) of each of the studied groups of atoms may contribute differently to the conduction band minimum; therefore, the transition studied with NEXAFS also would be different for each atom, due to the dipole selection rule. The measured energy distance between the core level and the final state in the CB is element-specific and can vary or not within the given stoichiometry of the sample. The local electronic environment of each atom of the material with a fixed composition and the measurable optical band gap becomes finally evident at the

macroscopic level. [73] Theoretical modelling of the unoccupied states in the CB is required to gain more insight into this problem.

Secondly, another uncertainty that possibly influences the results of the experiment is that the laboratory XPS is a surface sensitive technique, with the information depth of 3-5 nm, as well as UPS, used to determine VBM, while NEXAFS detected in a fluorescence mode is considered to be a more bulk sensitive method (300-400 nm). Nevertheless, the NEXAFS results obtained with fluorescence and total electron yield are very similar and lie in the same range of values, thus proving that the observed effects of the shift in the absorption spectra position when going from CZTS to CZTSe are true and independent from the detection mode used.

Indeed, the found shifts between the Cu K, L<sub>3</sub>, Zn K, L<sub>3</sub> and Sn L edges are in good agreement with theoretically predicted shifts of the conduction band minimum. The shift found for the polycrystalline thin film samples when going from pure sulfide to pure selenide composition is about 0.30±0.1 eV. The calculations of Repins et al. [58] result in changes in the CBM of kesterites when going from pure selenide to pure sulfide of about 0.35 eV. In addition to the polycrystalline film results, the shift in the absorption spectra found for the powdered samples are in the same range of values. However, a slight deviation of the powdered samples results from those for the thin films is noticed. The average shift between the NEXAFS spectra for the powdered samples is about 0.29±0.1 eV. The slightly lower shifts of the powdered samples can be due to the fact that the CZTS powder samples contain some of the secondary phases. The CZTS sample contains 2.95% of Cu<sub>0.92</sub>S that could influence the results of the absorption experiments.

### 6.1.5. Tetragonal distortion and the atomic-scale properties

Although the shifts obtained for the powder sample (Table 6.2) are in a good agreement with thin film results (Table 6.2), we propose here an explanation for the small, but systematic deviation of the results for powder samples from those for thin films.

It was already shown that the presence of a secondary phase in kesterite material can cause the deformation of its crystal structure. [9] The foreign phase usually has a different crystal structure, than the main one. The incorporation of the secondary phase material can locally influence the crystal structure of the main phase and thus cause a tetragonal distortion of the crystal structure and strain in the bulk. The structural distortions lead to changes in the electronic structure of the main phase.

The tetragonal distortion was already studied in detail in chalcopyrites and its strong influence on the electronic structure of CIGS was shown. [105] As a reminder, the deviation of the ratio of the lattice parameters  $a$  and  $c$  ratio from 1 is discussed, i.e.  $c/2a \neq 1$ . The deviation of the  $c/2a$  ratio can lead to a crystal field and in its turn can influence the valence band maximum. [9]

It was shown that there is a strong dependence between crystal and electronic structures of the II-IV-V<sub>2</sub> compound materials, such as chalcopyrite and kesterite. It was shown that the tetragonal distortion is determined by charge redistribution of the hybridized bonds, especially of the group IV atoms. Atoms B and C gain charge, while atom A loses charge.

In addition, it was already shown for kesterites using X-ray and neutron power diffraction that powder and thin films samples of the same chemical bulk composition nevertheless have different tetragonal

distortion values. [105] One of the reasons for that is the different preparation conditions of the samples, particularly a different cooling rate after the selenisation/sulfurization step. It was shown for CZTS samples that at a cooling rate of 1 K/h up to 10 K/h, the tetragonal distortion of the synthesized powdered samples deviates from 1 and leads to a strain in the bulk of material. The studied thin film samples revealed a tetragonal distortion value below 1. In general, powdered samples are expected to be more stoichiometric in comparison to thin film due to slower cooling rate and less amount of secondary phases.

In the present work, the studied powdered samples were prepared via a solid state reaction process using 50 K/h to cool the samples to 250°C and naturally cooled to room temperature after the furnace was switched off. In case of thin film samples the cooling rate was much faster- the cooling was allowed naturally, meaning the temperature was reduced to below 100°C in 1.5 h, i.e 300 K/h.

To our knowledge, no literature data is available on the influence of the preparation method together with the compositional changes in kesterites on its electronic properties, i.e. shift of the conduction and valance band edges, in terms of structural distortions in the crystal structure. So far, the speculation that the crystal structure of the material correlates with its electronic properties have been shown in work by W.G. Zeier et al. [106] Here, the composition of the chalcopyrite-type compounds were varied from  $\text{Cu}_2\text{ZnGeSe}_4$  to  $\text{Cu}_2\text{FeGeSe}_4$  and the changes of the chemical composition were correlated with the structural and electronic properties of the materials. It was shown that at a certain critical value of the  $c/2a$  ratio a full valance band convergence takes place.

Nevertheless, it is possible to claim that the strain in the material will influence the bond hybridization and charge distribution in kesterite when the anion composition is changed. The different tetragonal distortion values can lead to the different electronic properties which in turn will cause a shift in the absorption spectra. The difference in the NEXAFS results between powdered and thin film samples can therefore be attributed to the difference in their local electronic properties governed by the crystal structure. This assumption can also be studied in detail with X-ray diffraction in the future.

### 6.1.6. Summing up the NEXAFS results

When going from pure sulfide to pure selenide composition, the band gap changes and thus the relative position of the CBM also changes. NEXAFS was used to probe this shift in CBM. We have measured all cation-related absorption edges, namely Cu, Zn K- and L-edges and also the Sn L-edge. We observed a well-reproduced shift of  $0.30 \pm 0.1$  eV for polycrystalline samples. The result was confirmed using powder samples with well characterized composition used as references. The justification of application of NEXAFS as method for probing shift in CBM is also given.

## 6.2. Theoretical approaches for the conduction band assessment

In this subchapter the results of theoretical calculation used to study the shift in the conduction band are discussed. First, the results of the DFT calculation together with the GW approximation were used to

obtain VB and CB shifts when going from pure sulfide to pure selenide composition. Then DFT-derived states in CB were obtained to observe what governs shifts in the CB and consequently in the absorption spectra. Secondly, the results of the absorption spectra simulation using FDMNES code are presented. The shifts between the simulation spectra are discussed as well.

### 6.2.1.1 GW approximation calculations of the VBM and CBM relative positions

As it was shown in Chapter 4, the usage of the GW gives the best band gap values, which are very close to the experimental values (see Table 6.4). Therefore, it appears reasonable to use GW to obtain the relative shifts of the VBM and CBM. The results of the GW calculations were obtained by Archana Monoharan, PhD student, HU Berlin.

*Table.6.4. Comparison of the calculated and experimentally derived shifts of the conduction and valence edges when going from pure sulfide to pure selenide kesterite compositions.*

	Relative shift (eV)	
	Valence band	Conduction band
GW calculations [A. Monoharan, HU Berlin]	0.10	0.31
Experimental results [this work]	0.12	0.30
Theoretical reference [58]	0.15	0.35

An excellent agreement between experimentally derived relative shifts in the valence and in the conduction bands with calculated values using GW approximation is observed. The relative shift in the VBM of 0.13 eV was found using UPS and 0.10 eV using the theoretical approach. The conduction band shift of 0.30 eV was obtained with NEXAFS (here an average shift value is indicated), while the shift in the CBM calculated with GW is 0.31 eV. Thus the purely experimentally derived values found a very good agreement with theoretically obtained data. A deviation of about 0.05 eV for the VBM shift and 0.01 eV for the CBM shift is observed.

### 6.2.1.2. Density of states in the conduction band

In order to better understand the effect of the shifts of the absorption edges measured for pure sulfide and pure selenide samples, the total density of states (TDOS) and partial density of states (pDOS) of the conduction band of the kesterites with respective compositions were calculated. The shift in the DOS is proportional to the shifts in the NEXAFS spectra and can be explained with the calculated density of states. All results of DFT calculation of DOS are obtained by Archana Monoharan, HU Berlin.

The pDOS exhibit the same dependence (or independence) on the anion composition as the NEXAFS spectra. The DFT calculated DOS can explain the behavior of the NEXAFS spectra in terms of

element-specific atomic-scale structure that determines the density of states itself and therefore the electronic properties of the material. [111] The carefully chosen functionals can probably not give the exact value of the shift of the CBM, but the trend can be trustworthy. In addition to the DOS, the band gap values and relative shifts of valance and conduction bands were calculated.

The kesterite material was studied using DFT calculations with a focus on the dependence of the pDOS on compositional variations. The strong influence of the electronic states on the internal structural parameters, such as anion displacement, is known for CIGS compounds. [122] In the present work, the crystal structure of kesterite was considered to be ideal, i.e. no defects were included in to the input data. The GGA PBEsol exchange-correlation potentials were used to calculate the pDOS.

Thus, the TDOS and pDOS were obtained for two kesterite compositions: pure sulfide and pure selenide. (A figure of the TDOS and pDOS of CZTSe can be found in the Appendix).

A closer look to the states of the CB edge has revealed that the main contribution to the TDOS is given by Sn and Cu electronic states and to less degree by those of Zn. Following the dipole selection rule that governs the allowed transitions from the core levels into the unoccupied states in the conduction band, the Sn s-states, Cu p- and d-states and Zn p- states were calculated separately. The relative shift in CBM when going from pure S to pure Se can be obtained when partial DOS are compared in respective couples. The linear extrapolation of the leading edge of the DOS (black solid lines) to its intersection with the base line, was applied, similarly to the VB edge photoelectron spectra, to obtain a relative shift of the pDOS CZTS and CZTSe respectively. Clearly, the shift of the Cu pDOS is visible when going from pure sulfide to pure selenide composition. Moreover, the edge of the calculated states moves towards higher energies when changing the kesterite composition, which gives an excellent match with NEXAFS data. Shifts were observed also between other pDOS of CZTS and CZTSe. The obtained values are shown in Table 6.5:

*Table 6.5. The relative shifts between the edges of p-DOS calculated by A. Monoharan, HU Berlin for the CZTS and CZTSe compositions respectively*

<b>pDOS</b>	<b>Relative shift</b>
Cu-d	0.40±0.1
Sn-s	0.37±0.1
Cu-p	0.50±0.1
Zn-p	0.50±0.1

The trend towards a higher energetic distance of CBM to  $E_f$  when going towards a S-rich composition was thus confirmed for other pDOS using the full-potential all- electron DFT calculations. Larger shifts were found for Cu-p and Zn-p pDOS, namely 0.50±0.1 eV and slightly smaller values for Cu-d and Sn-s sates. Nevertheless, a very good qualitative agreement of the calculated pDOS with experimental results was found.

Therefore, we would like to stress, that the reproducible shift in the calculated pDOS is clear and valid for *all* pDOS that were allowed by the dipole transition rule. Moreover, these values are in *good* agreement with experimentally obtained values, i.e. all empirical shifts were reproduced with DFT calculations.

### 6.2.1.3. Local electronic properties of CZTS and CZTSe

The explanation for the observed changes in the position of the absorption edges and further obtained shifts of the pDOS of kesterites with different  $[S]/([S]+[Se])$  ratios is possible after a deeper insight into the crystal structure of the studied material. It is known, that the crystal structure of kesterites is significantly different after the selenium introduction, due to the larger size of the selenium atom [11]:

$$R_S^{empirical} = 100 \text{ pm}, R_S^{calculated} = 88 \text{ pm},$$

$$R_{Se}^{empirical} = 115 \text{ pm}, R_{Se}^{calculated} = 103 \text{ pm}.$$

where  $R_{S(e)}^{empirical}$   $R_{S(e)}^{calculated}$  are the radii of S or Se atoms, obtained experimentally and theoretically

The changes of the crystal structure of kesterite when going from CZTS to CZTSe, can be investigated using a 3D visualization program for structural models ‘‘Vesta’’. [126][125] The element-specific bond lengths  $d_{Cu-S}$ ,  $d_{Sn-S}$  and  $d_{Zn-S}$  were obtained for the pure sulfide and pure selenide kesterite compositions and listed in Table 6.6. Using the program the bond lengths between sulfur (selenium) atom to the first neighboring cations (two copper atoms, one zinc and one tin) were obtained.

Table.6.6. Element-specific bond lengths derived for CZTS and CZTSe materials

element-specific bond length (Å)	CZTS	element-specific bond length (Å)	CZTSe	$\Delta$ (Å)
$d_{Cu-S}$	2.3329(10)	$d_{Cu-Se}$	2.46(3)	0.127
$d_{Sn-S}$	2.4120(10)	$d_{Sn-Se}$	2.52(3)	0.111
$d_{Zn-S}$	2.3311(10)	$d_{Zn-Se}$	2.41(3)	0.082

The found data suggest that *all* specific bond lengths change after the replacement of the S with Se. The average deviation of the bond length in kesterite when going from CZTS to CZTSe is  $\Delta \sim 0.11 \pm 0.02 \text{ \AA}$ . The bond lengths shown in the Table 6.6 are results of the calculations and to our knowledge no real experimental data is available so far for kesterites. For comparison, the deviation of the bond-lengths in chalcopyrites when the *cation* composition is changed from  $CuInS_2$  to  $CuGaS_2$  is only about  $\Delta \sim 0.01 \text{ \AA}$ . ( See chapter 3 for more details)

Now, the shifts in the NEXAFS spectra and also in the calculated pDOS can be explained from the atomic-scale perspectives. The first nearest neighbor environment of cations in kesterites is very different in the CZTS and CZTSe systems. Initially, the nearest neighbors of any of the cations would be the four S atoms. If we replace them all with much bigger Se atoms, the structural environment of cation will change drastically. We already know that NEXAFS can provide precise information about the chemical environment of the probed atom. In addition, the absorption of the photon and subsequent exciting of the electron into unoccupied states in the conduction band highly likely will happened within the system of the absorbing atom itself. [111] Thus, after the anion replacement, the local electronic states of the cations will be strongly influenced by the new chemical environment.

As all bond lengths had undergone changes, the electronic states of all building atoms will be influenced. As a result, all cation absorption edges had revealed shifts with changing the anion composition of the kesterite.

As a remark, the NEXAFS experiment results described by Johnson et al. [73] for chalcopyrites supports the presented above hypotheses of the atom-scale structure. The changes in the cation composition of chalcopyrites barely change the local chemical environment of the other cations themselves, but that of the anions. And therefore, the local electronic environment of cations is not changed, but that of sulfur is. As the cation composition of samples was varied from CIS to CGS, the chemical environment of sulfur underwent changes, which were reflected as shifts in the S K and L<sub>3</sub> absorption edges. The stable first-neighbor surrounding of cations therefore brings us to the fact, that no shifts were observed in the Cu and Ga K- and L<sub>3</sub>, In L<sub>3</sub>- and M<sub>4,5</sub> edges.

#### 6.2.1.4. Summing up the results of ab-initio calculations

Summing up, the theoretical investigation of the electronic properties of the kesterite material was done using an all-electron code *exciting*. The structural parameters were obtained for both pure sulfide and pure selenide compositions. The good agreement with experimental data obtained using neutron powder diffraction was observed, as well as with other theoretical works available in literature. In order to determine the band gap of the CZTS and CZTSe, two theoretical approaches were used, and the GW approximation has provided the results very close to the experimental values. Further on, the GW approach was used to calculate the valence and conduction band offsets and it was shown that GW can provide reliable results. The values of the shifts in the VBM and CBM are in excellent agreement with experiment and other theoretical references.

In order to explain the observed results obtained using the absorption spectroscopy, DFT calculations of the electronic states of CZTS and CZTSe systems were performed by Archana Monoharan, HU Berlin. The experimental and calculated results are in very good agreement. All calculated pDOS of cations have revealed a shift that within the error matches the experimental data. The shifts in the absorption edge positions and in the calculated partial density of states have been correlated with the atomic-scale structure of the kesterite samples. The element-specific bond-length varies for each pair of atoms and thus determines the atomic-scale crystal structure of the material, which in its turn governs the element-specific density of states and thus finally, the electronic properties of the material. It was shown that each of the atom-specific bond lengths  $d_{Cu-S}$ ,  $d_{Sn-S}$  and  $d_{Zn-S}$  is different in CZTS and in CZTSe crystals. The introduction of the bigger selenium atom causes tangible changes in the structural environment of the surrounding atoms. That means that the electronic states of the cations will be influenced, leading to shifts in their X-ray absorption spectra.

### 6.2.2. FDMNES simulations of the kesterite absorption spectra

#### 6.2.2.1. Important computational parameters

The FDMNES simulation package described in chapter 4 was used to obtain absorption spectra of constituent cations of the kesterite material with different anion composition. Simulation of the NEXAFS spectra was performed using the same cluster potentials, implemented in the package and

the Green formalism was used for all calculations. Systematic analyses of the dependence of the input parameters and the electronic/structural characteristics of the studied crystal on the calculated absorption spectra were done, which allows understanding the formation mechanism of the absorption edge fine structure. A good agreement of the simulated and experimentally derived spectra is observed.

An important parameter that governs the simulations of the NEXAFS spectra is the cluster radius that can be chosen by the user in order to reproduce the fine structure of the absorption edges. To define the convergence conditions of the spectra, the simulations were performed with different cluster radii  $R$  ranging from 2 up to 7.5 Å. The Cu K-edges for the CZTS composition were obtained for  $R = 2 - 5$  Å and presented in Fig.6.3 (a) and for  $R = 5 - 7.5$  Å in Fig.6.3 (b).

Our simulations have shown that in order to sufficiently reproduce the NEXAFS spectrum, a radius of at least 7 Å should be used. The shape and the onset of the absorption spectra undergo visible changes when the cluster radius varies from 2 up to 3.75 Å. The further stepwise increase of the radius brings us to a more stable spectral picture: the edges of the simulated spectra undergo no changes, only slight changes in the wiggles, propagating after the edge were observed when going from 5 Å up to 6 Å of cluster radius. No changes were observed after  $R \geq 7$  Å: the fine structure of the NEXAFS spectra doesn't change any more.

Therefore, the proper environment for the resonant atoms is built when the cluster radius is approximately 7 Å and the influence of the neighboring atoms is properly represented in simulations. The kesterite unit cell consists of 31 atoms and has the following size:  $a \times b \times c = 5.4 \text{ Å} \times 5.4 \text{ Å} \times 10.84 \text{ Å}$ . The simulated cluster volume contains approximately 4,5 kesterite unit cells, which is 139 atoms. In addition, the bigger cluster radius will lead to a longer computational time without reasonable improvements of the simulated results.

Thus, all following simulations were performed with the cluster radius of 7 Å in order to properly reconstruct all relevant structural details of the absorption spectrum

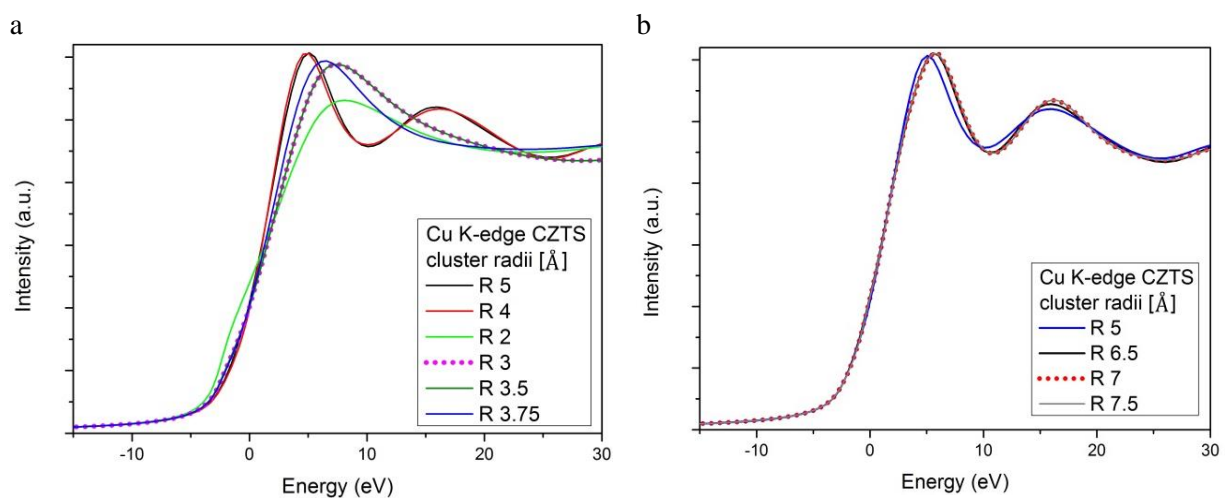


Fig.6.3. a and b. FDMNES calculated Cu K-edge absorption spectra with different cluster radii.

a: cluster radii  $R$  from 2 to 5 Å; b: cluster radii  $R$  from 5 to 7.5 Å.

There are other input parameters that govern the results of the simulations. One of them is the  $E_{\text{cut}}$  that has a strong influence on the calculated absorption spectra. Below this energy value lie occupied states, above – only unoccupied. However in the code this energy, defined as “*Efermi*”, has a different physical meaning, than the actual Fermi energy. In a real semiconductor, the Fermi level is used in the Fermi-Dirac statistics to describe the top of the collection of electron energy levels at absolute zero temperature. [131] Electrons are fermions, so they cannot occupy the same energy levels. At zero temperature they fill the lowest available energy states and form a “Fermi sea”. The Fermi level is a surface of that sea at absolute zero and no electron can rise above this surface. In a semiconductor, the Fermi level lies within the band gap energy and in a doped semiconductor it can be shifted towards the valance or conduction band edges, depending on the type of doping impurities.

On the other hand, the *Efermi* in the FDMNES package has a different concept. The states beneath *Efermi* level are still occupied, however, the actual value of the *Efermi* can be bigger or lower than the band gap energy of the studied semiconductor, so that the user can chose the value relative for the specific calculations. For instance by default, when the *No\_Fermi* keyword was used in the previous step, this energy level will be set to -5 eV.

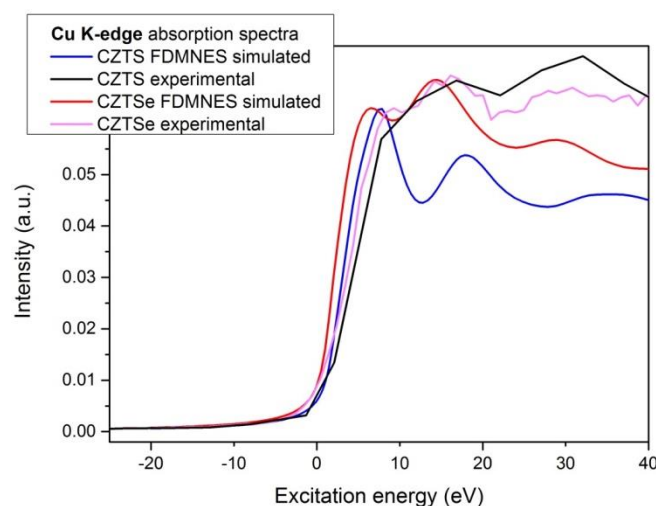
Therefore, in the following we will use  $E_{\text{cut}}$  to refer to the value of the *Efermi* parameter used in the code for a certain simulation.

Other convolution parameters such as energy range, the convolution broadening width, and the calculation step size can be varied depending on the task. The cross section before the convolution by default is set to zero. After several simulation series, the energy range for all calculated spectra was set from -20 eV up to 40 eV, in order to reproduce and depict the propagating after the NEXAFS edge wiggles, characteristic for the absorption spectroscopy.

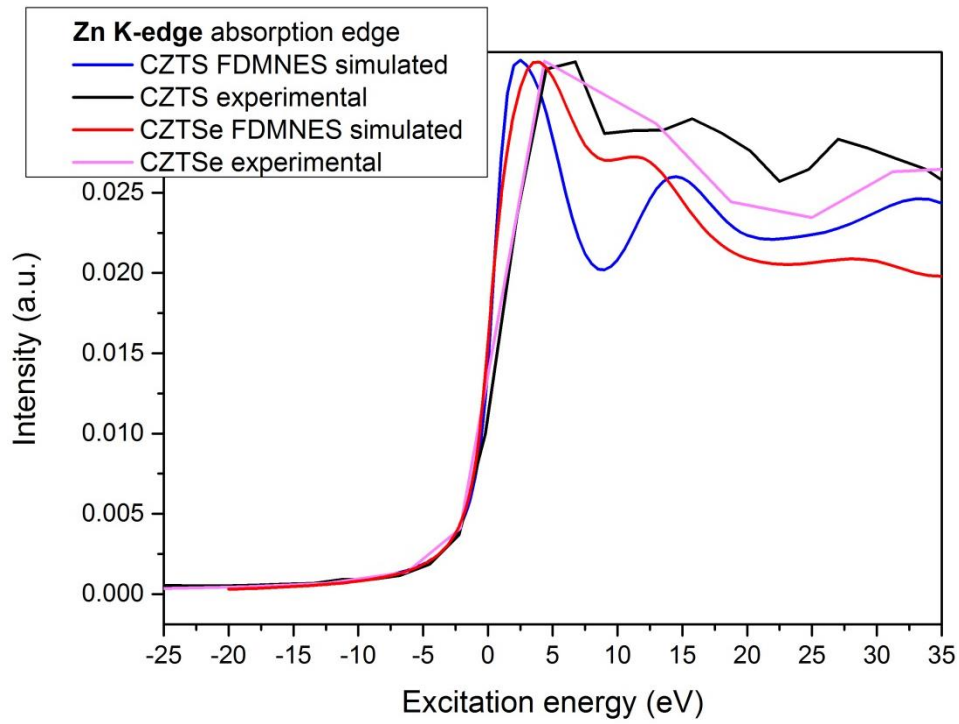
### 6.2.2.2. Simulated vs experimental spectra

In Fig. 6.4.the Cu K-, Zn K- and Sn L absorption spectra obtained by the FDMNES simulation package are compared with the respective edges received experimentally. Measured NEXAFS spectra, presented in the previous chapter, were normalized and plotted together with the simulated graphs for pure sulfide and pure selenide composition.

a



b



c

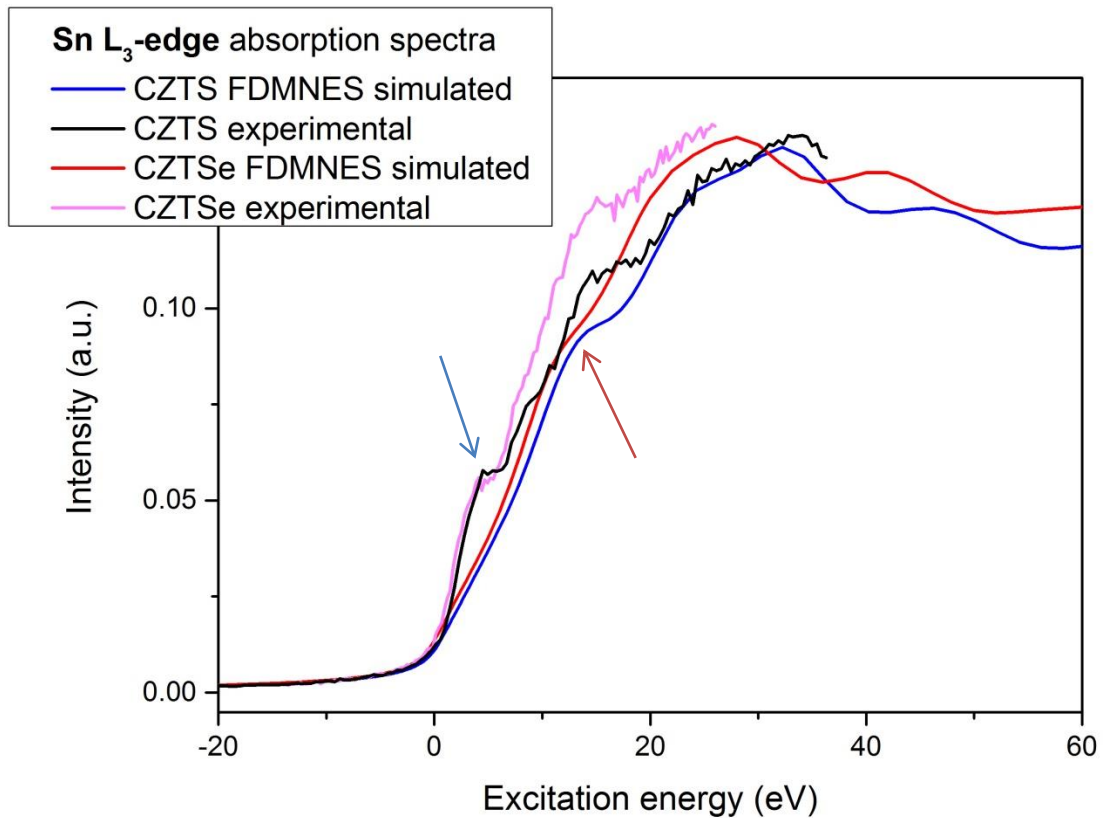


Fig.6.4. Absorption Cu (a) and Zn (b) K-, Sn L<sub>3</sub>-edges (c). FDMNES simulated spectra compared with experimentally derived data

On the whole, the simulated and experimental curves had shown a good match, however certain deviations between theoretical and experimental spectra are visible.

Firstly, the wiggles of the simulated Cu K-edge CZTS spectra start to propagate after an initial significant drop in the intensity, whereas the wiggles of the experimental curves are almost at the same intensity as the top of the absorption edge. The curves obtained for the pure selenide composition have revealed a better consistency. The position of the propagating wiggles is similar for both experimental and simulated CZTSe spectra.

The EXAFS area of the Zn K-edge (Fig.6.3, b) is very similar for both, experimental and simulated spectra- wiggles after the absorption edge have a very similar shape and relative position. The NEXAFS area, i.e. the slope of the edges, was also well reproduced by the simulations.

The FDMNES-derived Sn L<sub>3</sub>-edge seems to be different from the experimental edge, however, a closer look reveals, that a fine structure of the absorption edge was well reproduced. The simulated spectra have a small pre-structure approximately at the mid-half of the edge (in Fig.6.3, c, small pre-structure marked with a blue and red arrow for the simulated and experimental spectra couples respectively). The same features are visible at the experimental spectra. This finding is valid for edges obtained for both CZTS and CZTSe. A certain difference is noticed in the incline of the two types of spectra: experimental spectra are steeper; simulated are more tilted to the higher excitation energies.

We could only speculate about the reasons of the deviations seen between experimental and simulated spectra. However, it could be that the input file of the FDMNES package contains the information about the crystal structure of kesterite as a pure and ideal crystal, designed using a single crystal mesh. Yet, the experimental curves were obtained using thin film samples where, along with the main kesterite phase, other secondary phases (ZnS(e), CuSnS(e) etc.) were possibly present. They could have an impact on the shape and the position of the experimental absorption spectra and result in slight differences between simulated and non-theoretical curves.

### 6.2.2.3. Determination of the shifts between the simulated spectra

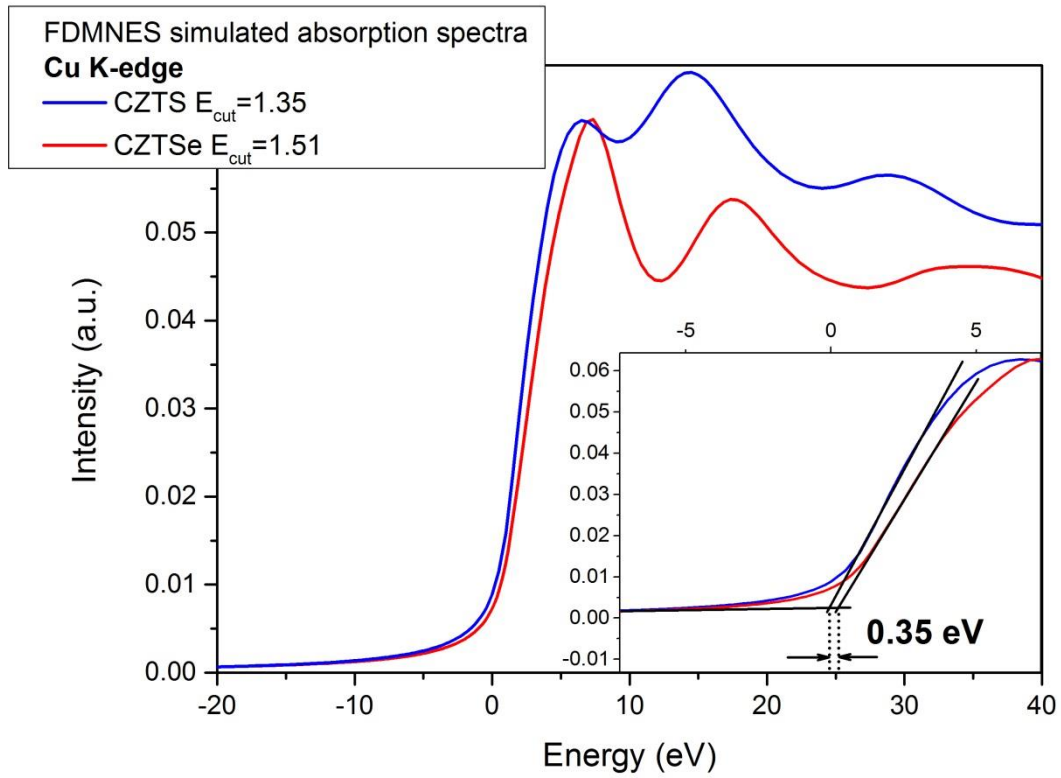
In Figure 6.5a and b, the FDMNES simulated absorption spectra of Cu and Zn K-edges are shown together with the inset. In addition, NEXAFS spectra of Cu, Zn and Sn L<sub>3</sub>-edges were obtained. (Not shown) The obtained spectra are coupled in pairs for the CZTS and CZTSe composition, respectively, in order to determine the shift between the spectra and compare it with the shifts seen in the experimentally derived ones.

The relative shifts of the calculated spectra are in a good agreement with experimentally derived data. The observed shifts between spectra obtained for pure sulfide and pure selenide composition were measured using the method described previously for UPS- and NEXAFS-derived data.

The linear extrapolation of the absorption edge itself till the intersection with the linear background will provide the relative position value of the each of the spectra (see the inset of the Fig.6.5. a, b). The obtained value can be compared to get the equivalent of the shift.

We have summarized the obtained shift values between the FDMNES calculated spectra and compared them with the experimental data in Table 6.7.

a



b

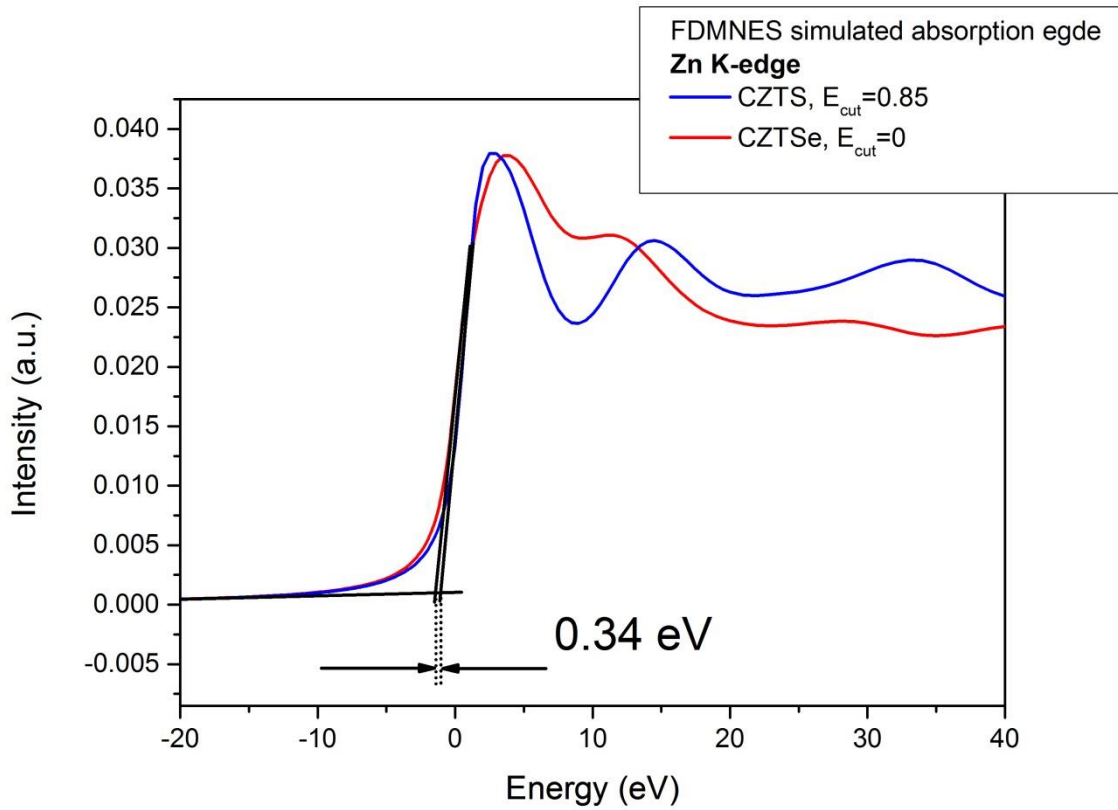


Fig.6.5 a and b. FDMNES calculated K-edge absorption spectra of a: Cu and b: Zn atoms. Insets:

Table 6.7. Relative shift between the CZTS and CZTSe FDMNES calculated and experimentally derived absorption spectra

Edge	Relative shift (eV)			
	FDMNES	$E_{\text{cut}}$		experiment
		CZTS	CZTSe	
Cu K-edge	+0.35±0.1	1.35	1.51	+0.31±0.1
Zn K-edge	+0.34±0.1	0.85	0	+0.29±0.1
Cu L-edge	+0.30±0.1	0.65	0.65	+0.30±0.1
Zn L-edge	+0.33±0.1	0.30	0	+0.29±0.1
Sn L-edge	+0.32±0.1	0.30	0	+0.32±0.1

The shift between simulated spectra agrees within the error with experimental data: shifts between FDMENS spectra are ranging from 0.30±0.1 eV up to 0.36±0.1 eV, while the experimentally derived shifts are between 0.29±0.1 eV and 0.32±0.1 eV for different cation absorption edges.

As far as  $E_{\text{cut}}$  was specified for the each set of simulations,  $E_{\text{cut}}$  values were given in Table 6.7.  $E_{\text{cut}}$  was chosen so that occupied states will be separated from the unoccupied and only the latter will contribute to the simulated edge after the convolution. If a too low  $E_{\text{cut}}$  was chosen, an unnatural pre-shoulder was visible before the edge after the convolution- a sign that a higher value of  $E_{\text{cut}}$  parameter should have been taken. In this way, a critical value of the  $E_{\text{cut}}$  was chosen for each set of simulations, so none of the occupied states will be involved into convolution, but yet all of the unoccupied states.

We haven't observed any dependence of  $E_{\text{cut}}$  on other input parameters or physical properties of kesterites. Detailed investigations can be done in the future to unravel the relation between  $E_{\text{cut}}$  with known electrical or chemical properties of the studied semiconductor.

#### 6.2.2.4. Summing up the results of FDMNES simulations

Summing up, we have used the FDMNES software package to reproduce the experimentally observed shifts in the absorption spectra when going from pure sulfide to pure selenide kesterite composition. The package allows implementing the crystal structure of the studied material, controlling the simulated cluster radius and other computational parameters. We obtained all relevant absorption spectra for CZTS and CZTSe systems: Cu and Zn K-edges, Cu, Zn and Sn L<sub>3</sub>-edges. A visual graphical comparison of the FDMNES simulated and experimental absorption spectra has brought us to the conclusion that the possible presence of secondary phases in the bulk of the thin film kesterite absorber could influence the fine structure and propagating wiggles of the experimentally derived absorption spectra. The perfect crystal of the kesterite material, implemented into the simulation input files, provides slightly different spectral curves than that measured using thin film samples. Nevertheless, we would like to stress that all important spectral features were reproduced by the

FDMNES package and simulated absorption edges can be further used for analyses of the CBM shift when going from pure sulfide to pure selenide kesterite composition.

Thus, the shifts between FDMNES-derived spectra were obtained and found values are in a very good agreement with the previously found shifts between spectra measured for thin film samples. The theoretical values are in the range of  $0.3-0.35\pm 0.1$  eV, whereas experimental values were found to be  $+0.29\pm 0.1$  eV for the Zn K- and L-edges and up to  $+0.32\pm 0.1$  eV for the Sn L-edge. The value of the theoretical shift strongly depends on the input  $E_{\text{cut}}$  parameter, which sets apart the occupied and unoccupied states of the simulated system. Further investigations are necessary to define the relation between  $E_{\text{cut}}$  and Fermi energy of the CZTS and CZTSe.

On the whole, a good match between calculated and measured spectra is sufficient to suggest the FDMNES package for future studies of NEXAFS spectra.

## 7. Conclusions

The goal of this work was to investigate surfaces and interfaces of kesterite-based thin film solar cell in order to optimize their performance. Aiming to obtain the optimum composition of the kesterite layer, the anion composition was changed, ranging from pure sulfide to pure selenide. The surface chemical and electronic properties of respective samples were investigated in detail using X-ray based spectroscopies.

Prior to our investigation, we had the following questions in our focus:

- How does the surface composition of kesterite change upon etching?
- What is the band line-up of these kesterites with CdS?
- What is the effect of annealing on the electronic and chemical surface properties of kesterite?
- What is the change of the band position upon change of the anion composition?
- How can the conduction band edge be measured?
- How can band position and absorption edge be calculated using simulation software?

Answering these questions helps to understand the nature of the kesterite material and establish rules of its interaction with other functional layers.

First, the chemical and electronic surface properties of kesterite absorber layers with anion composition ranging from pure sulfide to pure selenide were investigated using photoelectron spectroscopies. Depending on the anion composition, specific etching procedures were applied to remove secondary phases and the effect of the applied etchings is described in Chapter 5. The quantitative elemental analysis has shown that the as-received surface composition of samples deviates from the bulk and from the nominal composition of the precursor. The surface composition deviates even more after the etching due to selective removal of the segregated secondary phases from the surface. The found deviation in the composition of bulk and surfaces can be used for the future precise engineering of the kesterite absorbers.

Secondly, the detailed investigation of the relative positions of the valence band edge was done using UPS and the results are shown in Chapter 5. Seven samples with  $[S]/([S]+[Se])$  ratio ranging from 1 to 0 were analysed and a shift of  $-0.12\pm 0.1$  eV was found, which is in a good agreement with theoretical values reported previously. Further investigations of the VBM shift have been done at the synchrotron BESSY II using different excitation energies, allowing probing the near-surface region of kesterite samples. The shift of around  $-0.12\pm 0.1$  eV was reproduced using a wide range of  $E_{ex}$ , supporting the found values in laboratory conditions.

In the second part of the Chapter 5, the band alignment with cadmium sulphide-one of the most common buffer layer materials-has been studied. For a long time there was no agreement on the band alignment in system kesterite/CdS. Therefore we decided to hunt down this question and investigate ourselves the band alignment at the kesterite/ CdS interface. For that propose, CBD CdS was deposited on kesterite films and the electronic properties of the buffer layer were investigated with UPS. The observed  $VBM_{CdS}=2.2\pm 0.1$  eV indicates an n-type doping. Using the found VBM for CdS, the band alignments with CZTS and CZTSe were calculated. *Cliff-like offsets* were observed with both CZTS and CZTSe-based junctions:  $-0.62$  and  $-0.34\pm 0.1$  eV respectively. Interestingly, the CBD CdS prepared by IREC and measured at the synchrotron BESSY II revealed a different VBM to  $E_F$

distance, namely  $1.75 \pm 0.1$  eV. Here the offsets with kesterite absorbers were more favourable for a solar cell:  $-0.34$  cliff with CZTS, and  $+0.02 \pm 0.1$  eV spike with CZTSe.

Measured band alignments were correlated with the known efficiencies and other cell parameters of the completed devices provided by IREC. The efficiencies of the cell steadily increase as the content of Se increases and reach 3.4% for sample number 5 with  $[S]/([S]+[Se])=0.24$ . The band gap of the absorber was estimated to be  $E_g=1.12$ , which is in a good agreement with the band gap of the record devices reported in literature.

It is interesting to note that the efficiency of the devices can be influenced by a thermal treatment of the absorbers prior to the buffer deposition. [77][87]As absorber layers were annealed at  $200^\circ\text{C}$ , the efficiency of devices dropped to nearly 0% along with a huge decrease of the other cell parameters. Surprisingly, the efficiency was recovered or even slightly improved after annealing at  $400^\circ\text{C}$ . To investigate this problem, the CZTSSe samples with  $[S]/([S]+[Se])=0.3$  were annealed at  $200^\circ\text{C}$  and  $400^\circ\text{C}$ . The surface relative composition and the VBM to  $E_F$  distance were measured before and after thermal treatment and the modifications were observed after usage of both temperatures. To illustrate the effect of annealing on the electronic properties of kesterite, we have calculated a band offsets at the CZTSSe/CdS interface. We saw a negative  $-0.24$  eV cliff offset at CZTSSe annealed at  $200^\circ\text{C}$  at the interface to CdS and, in contrary, a  $+0.01$  positive spike in case of CZTSSe annealed at  $400^\circ\text{C}$ . Therefore, part of the drop in efficiency can be explained due to an unfavourable cliff-like alignment at the absorber/buffer interface after annealing at  $200^\circ\text{C}$ , and a recovery of the efficiency after usage of higher temperature owing now to a better alignment –a small cliff of  $+0.01$  eV.

Thus, a comprehensive study of the band alignment between kesterite absorbers with different sulfur to selenium ratios and CdS buffer layers were done. There are several factors that have their impact on the band alignment between kesterite absorber and buffer layer. First, the deposition method of the buffer layer, i.e. solution concentrations, temperature and duration of the CBD. A strong deviation of the electronic properties of the supposedly same CdS was seen and this challenges a purely theoretical approach of band alignment prediction, such as Anderson rule etc. Apparently there are other mechanisms that govern the formation of the interface apart from the work function of the pure materials. Secondly, the low temperature annealing step used for the kesterite absorbers change their electronic properties as well as relative chemical composition.

In general, the main limitation for the performance of kesterite cells- the low  $V_{oc}$  is discussed throughout in literature. Several reasons are mentioned such as secondary phases, Cu/Zn disorder and recombination and the kesterite /CdS interface. According to our investigations of the band alignment at the kesterite /CdS interface, we tend to speculate that the relatively low  $V_{oc}$  in the kesterite devices is due to the bulk of the kesterite absorbers, rather than the surface. The poor bulk quality with a high recombination velocity at the grain boundaries has its drastic impact on the device performance. The carriers are “lost” much earlier than they reach the charge separation region. A deeper insight in to the bulk properties of kesterite is necessary.

Thirdly, the shift in CBM was in the focus of this work and Chapter 6 is devoted to this challenge. We have used an indirect method to probe the CB edge – X-ray absorption spectroscopy. A set of Cu, Zn K- and L- and Sn L-edges were measured and compared in respective pairs for CZTS and CZTSe samples. The relative shift between the spectra corresponds to the shift in the CBM when S is replaced with Se. The detailed investigation of the corresponding core levels by XPS has shown that no measurable chemical shift is induced by the changes in the anion composition of the kesterite and therefore the observed shift in the NEXAFS spectra is attributed to the shift in the LDOS in the conduction band. Thus an average shift of  $+0.30 \pm 0.1$  eV was found, which is in good agreement with

the shifts predicted by the theoretical calculations. The shifts found for the thin film absorbers are also in a good agreement with shifts found for the powdered samples used as references, due to their well-defined composition and the single phase nature. The shift observed for the powder samples was on average  $+0.29\pm 0.1$  eV, which agrees well with the polycrystalline samples results.

As reproducible experimental results were obtained, we have looked at the shift in CBM using a theoretical approach- Density Functional Theory Calculations. In Chapter 6 the DFT-derived TDOS and pDOS for pure sulfide and pure selenide kesterites obtained by PhD student A. Monoharan are shown. The *exciting* code developed by the group of Prof. Draxl was used to calculate the relative shift of VBM and CBM when going from CZTS to CZTSe. The theoretical values obtained with the GW approximation are in excellent agreement with the experimental values found by us using UPS and NEXAFS, namely 0.1 and 0.30 eV for valance and conduction band edges shifts respectively.

Further studies of the conduction band minimum were done through DFT calculations of the element-specific unoccupied states of CZTS and CZTSe, and comparison of those in corresponding pairs. Relative shifts between the states are within the range of 0.37 to  $0.50\pm 0.1$  eV. Although some of the observed shifts of the theoretically calculated pDOS cover the whole difference in the kesterite band gap, i.e. 0.50 eV, the trend in the positioning of the selenium-related states closer to  $E_F$  than that of the sulfur is the same as observed by the experimental methods. Therefore, the positive shift of the valence band and the negative shift for the conduction band when going from pure sulfide to pure selenide was confirmed by the DFT calculations.

The observed shifts in the absorption spectra and in the calculated states have been correlated with the atomic-scale structure of the kesterite samples. As far as absorption spectroscopy is an element-specific technique, i.e. atoms of one kind are excited at once, the waves propagation in the crystal structure is determined by the first nearest neighbors and by the distance between excited and neighboring atoms. It was shown that the atom-specific bond length between anions and cations will change when the S atom is exchanged by Se. That also means that the electronic states of the atoms will be influenced by changes in the local environment. The absorption process will happen differently in CZTS and CZTSe systems and will be reflected as a shift between the absorption spectra of the same atom.

Further theoretical modeling of the effect done by changes in the anion composition of the kesterite absorbers was made using the simulation package FDMNES. This package allows simulation of absorption edges of different materials including kesterite. The input file contains information about the crystal structure of pure sulfide and pure selenide kesterite, size of the simulation cluster, a computation step and a so called  $E_{cut}$  parameter.  $E_{cut}$  is used to separate the occupied and unoccupied states in the CB and is defined for each atom separately. Cu, Zn K- and L- edges and Sn L-edge were calculated and all essential spectral features were well reproduced together with the shifts between the CZTS- and CZTSe-related spectra. The values of the shifts between simulated spectra are in the same range as the experimental values:  $0.30-0.35\pm 0.1$  eV.

Summing up, a detailed study of the electronic and chemical surface properties of the kesterite material in frame of the anion composition changes was done. The experimental work was conducted using different photoelectron spectroscopies in the laboratory as well as at the synchrotron, such as XPS, UPS, HAXPES and absorption spectroscopy. Experimental results were correlated with the theoretical DFT and one-electron approach calculations and a good agreement between them was found. Our task within the KESTCELL project was to identify the most favorable band alignment between the kesterite and buffer layer, so that the device efficiency could be increased using our forecasts. Now that these were obtained, we can conclude that despite a comprehensive analysis of the

kesterite and buffer layers electronic and chemical properties, the band alignment at the absorber/buffer interface is not the main limiting factor for the device performance. More likely, recombination at the grain boundaries, the impact of detrimental secondary phases and an overall poor bulk quality of kesterites are primary limiting factors. The highly efficient devices were nevertheless produced by EMPA (Eidgenössische Materialprüfungs- und Forschungsanstalt) using a wet-chemical method, where the cell shunting or bad buffer coverage were the bigger issues than unfavorable band alignment with CdS. In addition, the alkaline-metals doping of absorbers boosted the devices to a great degree. Thus, the knowledge obtained within the study presented in this thesis can be considered as fundamental rather than engineering-wise and helps to better understand the physical properties and a nature of kesterite material in general.

## 8. Outlook

Based on the above conclusions, several directions of the future research can be proposed. First, the study of alternative buffer layers would be interesting for the future development of Cd-free solar cells. So far the kesterite-based solar cells with CdS buffer layer have already proven a high efficiency and stability. However, the *Directive on the Restriction of the Use of certain hazardous Substances in Electrical and Electronic Equipment* (RoHS) and *Waste Electrical and Electronic Equipment Directive* (WEEE) [132] regulate the usage of toxicants and heavy metals such as Hg, Cd, Pb in electronic devices such as thin film solar cells in the EU and no solar cells containing cadmium are allowed to be implemented into the customer products. These types of devices are expected to enter the main waste stream and therefore potentially pollute the environment. [132] So far, the fabrication of the Cd-containing modules is not forbidden yet, and Cd-pollution can be avoided in case of proper recycling, nevertheless, Cd-free devices would be a better option for the future productions.

Secondly, the electronic properties of kesterite, namely the shift in conduction band can be also studied further in detail. Our suggestion is to look at the CB edge using alternative experimental technique such as inverse photoelectron spectroscopy (IPES), where the surface of a sample is bombarded with a beam of well-collimated electrons. Of course, IPES has its limitations and can cause surface charging, still the shift in CBM could be measured independently with a fundamentally different technique and compared with values obtained with NEXAFS.

Finally, a better understanding of mechanisms that govern the position and shape of absorption edges can be done. The simulation of the absorption edges with the FDMNES package has shown the potential of such theoretical root of the data analysis. Different simulation packages are available already in literature: DFT-based Wien2K and QuantumEspresso for K-edges, and CTM4XAS for L-edges.

On the whole, the kesterite material has shown a big progress within the last 10 years and keeps steadily improving. Tandem kesterite-based solar cells are now in focus of the fundamental research. Much work remains yet to be done to understand the fundamental properties of kesterite and to optimize the cell performance. For industrial production, long-term stability and reproducibility studies are required.



## 9. Author's publications

- [1]. T. Olar, I. Lauer mann, H. Xie, M. Neuschitzer, E. Saucedo, W. Calvet, A. Steigert, B. Ümsür, B. Chacko, V. Parvan, M. Gorgoi, B. Senkovskiy and M. Ch. Lux-Steiner "Assessment of chemical and electronic surface properties of the  $\text{Cu}_2\text{ZnSn}(\text{SSe})_4$  after different etching procedures by synchrotronbased spectroscopies." *Energy Procedia* 84, 8 – 16( 2015 ).
- [2]. M.Neuschitzer, Y.Sanchez, T.Olar, T.Thersleff, S.Lopez-Marino, F.Oliva, M.Espindola-Rodriguez, H.Xie, M.Placidi, V.Izquierdo-Roca, I. Lauer mann, K.Leifer, A.Pérez-Rodriguez, E.Saucedo "Complex Surface Chemistry of Kesterites: Cu/Zn Reordering after Low Temperature Postdeposition Annealing and Its Role in High Performance Devices"*Chem. Mater.* 27, 5279-5287 (2015).
- [3]. H. Xie, S. López-Marino, T. Olar, Y. Sánchez, M. Neuschitzer, F. Oliva, S. Giraldo, V. Izquierdo-Roca, I. Lauer mann, A. Pérez-Rodríguez, and E. Saucedo "Impact of Na Dynamics at the  $\text{Cu}_2\text{ZnSn}(\text{S,Se})_4/\text{CdS}$  Interface During Post Low Temperature Treatment of Absorbers" *Appl. Mater. Interfaces* 8, 5017–5024 (2016).
- [4]. T. Olar, I. Lauer mann "Diffusion of indium in kesterite thin film solar cells investigated by hard X-ray photoelectron spectroscopy" The 562nd Wilhelm and Else Heraeus-Seminar "From Sunlight to Fuels" poster session, Bad-Honnef, Germany. (2014).
- [5]. T. Olar, I. Lauer mann, H. Xie, E. Saucedo, W. Calvet, A. Steigert, B. Ümsür "Assessment of the  $\text{Cu}_2\text{ZnSnSSe}_4$  surface properties after different etching procedures by X-ray, ultraviolet and hard X-ray photoelectron spectroscopies" poster session, Kesterite European Meeting, Tallinn, Estonia (2014).
- [6]. T. Olar, I. Lauer mann, H. Xie, E. Saucedo, W. Calvet, A. Steigert, B. Ümsür, B. Chacko, V. Parvan "Assessment of the  $\text{Cu}_2\text{ZnSnSSe}_4$  chemical and electronic surface properties after different etching procedures by synchrotron-based spectroscopies" talk, E-MRS Spring meeting Lille, France (2015).
- [7]. T. Olar, I. Lauer mann, H. Xie, E. Saucedo, W. Calvet, A. Steigert, B. Ümsür "Electronic and chemical surface properties of kesterite with different  $[\text{S}]/([\text{S}]+[\text{Se}])$  ratios tackled by the synchrotron-based spectroscopies" poster session, Kesterite European Meeting, Newcastle, England (2015).



## 10. Appendix

- a) *exciting* code for the simulation of the electronic states in the CB using the GW approximation

The single-particle equation for the electron gas:

$$\left[-\frac{1}{2}\nabla^2 + V_H + V_{\text{ext}} + V_{\text{xc}}\right]\psi_{\mathbf{nk}}^{\text{KS}} = \epsilon_{\mathbf{nk}}^{\text{KS}}\psi_{\mathbf{nk}}^{\text{KS}} \quad (10.1)$$

where  $V_{\text{xc}}$  represents the GGA-PBESol exchange-correlation functional,  $V_H$  is the Hartree potential,  $V_{\text{ext}}$  external potential, that approximates the interaction with nuclear,  $\psi_{\mathbf{nk}}^{\text{KS}}$  is the quasi-particle wavefunction,  $\epsilon_{\mathbf{nk}}^{\text{KS}}$  the quasi-particle energy.

The proper way of calculating the single-particle excitation energies is through the usage of the Green function theory. The quasiparticle energies  $E_i$  can be obtained from the quasiparticle equation:

$$\left[-\frac{1}{2}\nabla^2 + V_{\text{ext}}(\mathbf{r}) + V_H(\mathbf{r})\right]\psi_{\mathbf{nk}}(\mathbf{r}) + \int \Sigma(\mathbf{r}, \mathbf{r}'; E_{\mathbf{nk}}^{\text{qp}})\psi_{\mathbf{nk}}(\mathbf{r}')d\mathbf{r}' = E_{\mathbf{nk}}^{\text{qp}}\psi_{\mathbf{nk}}(\mathbf{r}) \quad (10.2)$$

The non-local and energy-dependent potential  $\Sigma$  contains the effect of exchange and correlation.  $\Sigma$  is the self-energy that contains the electron-electron interaction and it is basically a product of the Green function and the screened Coulomb interaction. But unfortunately it is very difficult to calculate the  $\Sigma$  even for the electron gas. Therefore one has to use the *GW* approximation [116] which is the simplest working approximation that takes screening effects in to account:

$$\Sigma = i\text{GW} \quad (10.3)$$

The *GW* derived from the many-body perturbation theory and the Coulomb interaction is dynamically screened, which is the big advantage of the approximation. The *GW* method is the state-of-the-art approach for the first-principle calculations of the band structures in crystalline solids. [115] The *GW* can be applied to a large class of materials, metals, transition metals and insulators. The method was first time proposed by Hedin. [116], [117]

Motivations for the *GW*:

- In atoms, screening is small and *GW* works well for atoms.
- In electron gas, screening is very important to be taken into account and here *GW* works also well, especially in semiconductors.
- For a core electron excitation, the Coulomb interactions in included into *GW*

The *GW* can be applied to calculate single-particle excitation spectra, the total energy and the expectation value of any single-particle operator in the ground state.

The quasiparticle energy  $\epsilon_{\mathbf{nk}}^{\text{qp}}$  is obtained as first-order correction to the Kohn-Sham eigenvalue  $\epsilon_{\mathbf{nk}}$ .

$$\epsilon_{\mathbf{nk}}^{\text{qp}} = \epsilon_{\mathbf{nk}}^{\text{KS}} + \langle \mathbf{nk} | \Sigma(\epsilon_{\mathbf{nk}}^{\text{qp}}) - V_{\text{xc}}^{\text{DFT}} | \mathbf{nk} \rangle \quad (10.4)$$

b) FDMNES package for absorption spectra simulations. The finite difference method

Here we would like to briefly present a summary of the essential physics important to understand the FDM. The method was discussed in detail in Ref [125] and [128].

The transition amplitude  $M_{gf}$  between the initial core state  $\psi_g$  and final state  $\psi_f$  is given by [110]

$$M_{gf} = \left\langle \psi_f \left| \boldsymbol{\varepsilon} \cdot \mathbf{r} \left( 1 + \frac{i}{2} \mathbf{k} \cdot \mathbf{r} \right) \psi_g \right. \right\rangle, [110] \quad (10.5)$$

with  $\mathbf{k}$ - photon wave vector,  $\boldsymbol{\varepsilon}$ - polarization direction,  $\mathbf{r}$ - the atomic position within the unit cell, or the radial distance to the center of the cluster. The physical meaning of the transition amplitude  $M_{gf}$  is that the squared absolute value of  $M_{gf}$  will give the probability of the system to go from the initial state  $\psi_g$  into final  $\psi_f$ . Here we neglect the spin for simplicity. Then, the photoabsorption cross section  $\sigma$  in XANES is given by [110]:

$$\sigma = 4\pi^2 \alpha \hbar \omega \sum_{f,g} |M_{gf}|^2 \delta(\hbar\omega - E_f + E_g) \quad (10.6)$$

where  $\alpha$  is the fine structure constant,  $\hbar\omega$  the photon energy,  $E_f, E_g$  are the final and initial states energies,  $\delta$  – Dirac delta function, respectively.

One atom will create the emitted amplitude, which is given by:

$$A = (\hbar\omega)^2 \sum_{f,g} \frac{M_{gf}^{i*} M_{gf}^s}{E_f - E_g - \hbar\omega + i\left(\frac{\Gamma}{2}\right)} \quad (10.7)$$

The total amplitude for all considered atoms will be then obtained through the summation over all these atoms, i.e. their positions  $\mathbf{R}_a$  and weighted by the phase factor  $e^{i(\mathbf{k}_i - \mathbf{k}_s)\mathbf{R}_a}$ .

Therefore, using *ab initio* calculations, the initial core level state of photoelectron is possible to calculate as well as the matrices  $M_{gf}$ . The real difficulty is to evaluate the final states, which can then be performed through the *finite difference method*.

FDM is a general method to solve differential equations by *discretization* of those over the whole calculation volume. For XANES that would mean- solving the Schrödinger equation in the spherically symmetric volume with the atom in its center and extend that to sufficiently large clusters (the volume of the cluster can be defined by the user).

After the “discretization”, the unknown sought quantities are the values of the wave function on each grid point “*i*”:  $\psi_i = \psi_i(r_i)$  and should be calculated inside of the defined spherically symmetric volume. [110] The Laplacian is then given by:

$$\Delta\psi_i = \frac{1}{h^2} \left( \frac{4}{3} \sum_{f,\varepsilon} \psi_j^\varepsilon - \frac{1}{12} \sum_{f,\varepsilon} \psi_j^{\varepsilon\varepsilon} - \frac{15}{2} \psi_i \right) \quad (10.8)$$

that can be obtained by approximating  $\psi_i$  by a forth order polynomial.  $\psi_j^\varepsilon$  and  $\psi_j^{\varepsilon\varepsilon}$  ( $\varepsilon = -$  or  $+$ ) are the values of the wave function  $\psi_i = \psi_i(r_i)$  on the positions of the first and second neighboring point “*i*” in

the direction  $\epsilon_j$ ,  $h$  – distance between the points. Let's denote the Laplacian with  $l_{ij}$ , then the Schrödinger equation on point “ $i$ ” will be [110]:

$$(-l_{ij} + V_i - E)\psi_i + \sum_j^{neighbors} -l_{ji}\psi_j = 0 \quad (10.9)$$

Therefore we have obtained a large system of the linear equations for each point “ $i$ ”. FDM allows obtaining rather accurate computational results using a smaller distance between the discretizing points.

Now, we have to calculate the wave function in the area around the absorbing atom. This area should be chosen so that the back scattered wave function doesn't contribute to the scattered wave field. Thus the limiting outer sphere separates the area where the potential is assumed to be constant or at least spherically symmetric. Inside this sphere (up to 0.5-0.7 Å) the FDM equation is applied.

The potential on the node points (i.e. atomic cores) is given by a multipole expansion around the center [110]:

$$V(\mathbf{r}) = \sum_L V_L(r)Y_L(\Omega) \quad (10.10)$$

$r$ - radial distance to the center of the atom,  $\Omega$ - angular position,  $L$  indicates  $(l,m)$ ,  $Y_L(\Omega)$  is defined by [128]. Then the general solution  $\psi(\mathbf{r})$  in the atomic sphere is [110]

$$\psi(\mathbf{r}) = \sum_L a_L \phi_L(\mathbf{r}) \quad (10.11)$$

which is basically the linear combination of the independent solutions of the Schrödinger equation. But as we approach closer to the ion core, the kinetic energy of the electron is getting higher, but still being rather low in between the two ion cores. Therefore, the intermediates in the spherically symmetric volumes are introduced, smaller than usual muffin-tin spheres. However, often the potential is assumed to be completely spherical and the potential (4.16) will be reduced to the first term.

In the interstitial space the potential is constant and the general solution is [110]:

$$\psi^f(r) = J_{L_f}(r) + i \sum_L \tau_L^f H_L^{(1)}(r) \quad (10.12)$$

where  $J_L$  and  $H_L^{(1)}$  are the Bessel and Hankel functions [110], the amplitudes  $\tau_L^f$  are the unknowns.

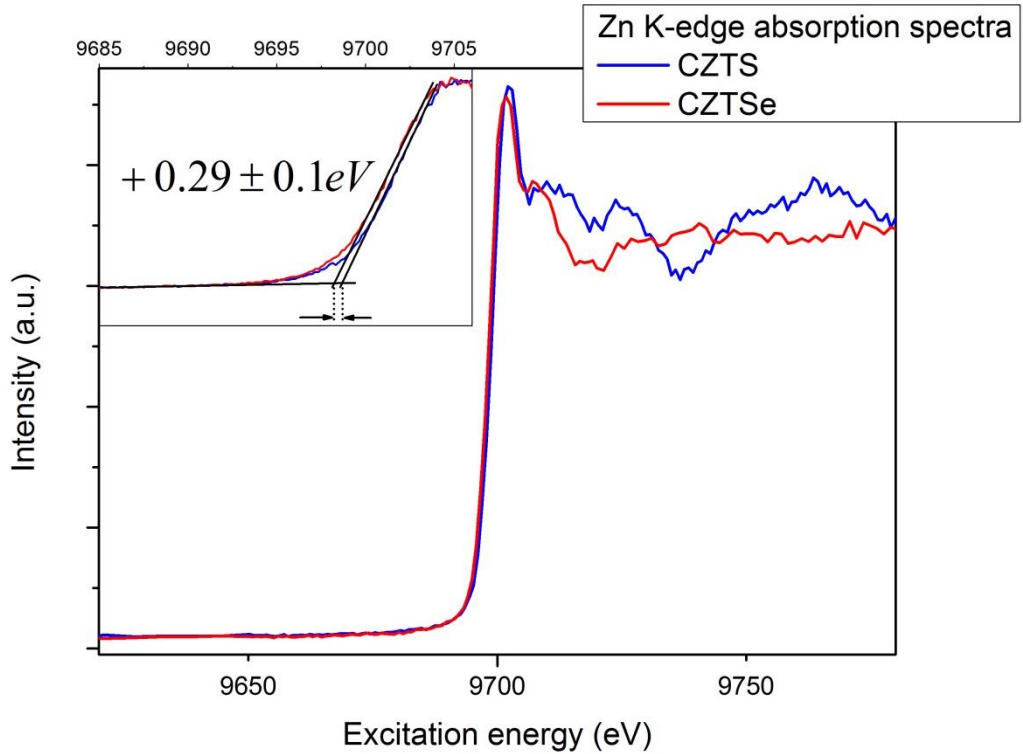
Now, having the Schrödinger equation for all points of the grid, it is necessary to write the general matrix. It consists of  $n_p$  Schrödinger equations on the  $n_p$  grid points. The potential is calculated from the local density approximation. The electronic density can be obtained using the linearized augmented plane wave (LAPW) method. [125]

Typically, in the XANES calculations, atoms are taken as neutral and solving the Poisson equation, the Coulomb potential can be obtained. The FDM allows no potential shape approximation, thus avoiding the problem of the classical muffin-tin approximation. One can perform the calculation with and without the muffin-tin approximation in order to study in detail the effect of the approximation of the shape of the potential. Or to prove the FDM approach for XANES, one can compare the muffin-tin approximation with the multiple-scattering approach.

c) Experimentally derived NEXAFS spectra

In Fig.1 the experientially derived absorption spectra for Zn K (a) and Sn L-edges (b) are shown.

a



b

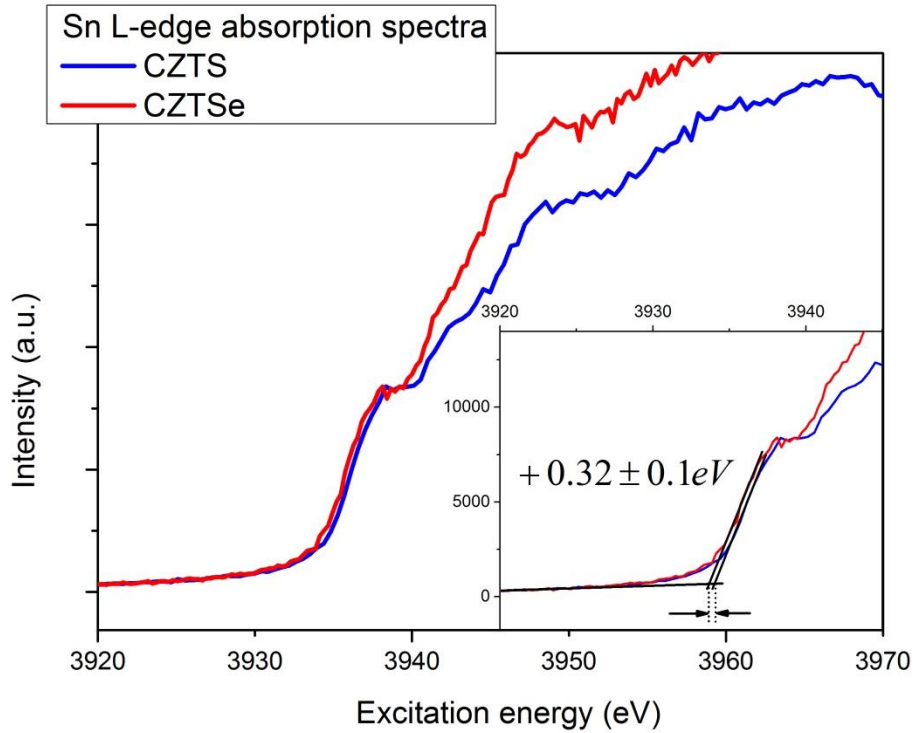


Fig. 1. Absorption edges of a) Zn K, b) Sn L from CZTS and CZTSe. The energy scales of the spectra are relative, thus making the shifts in the spectra correspond to the real energy shifts in the conduction band edge

#### d) Ab-initio calculation of kesterite crystal geometry

The data presented in this section is a part of the PhD thesis of Archana Monoharan. To be submitted to the Humboldt University Berlin. Supervisor: Prof. Draxl.

The crystal structure of kesterite is well studied using different techniques, such as wavelength-dispersive X-ray spectroscopy and neutron diffraction. [11], [9] We used data to perform calculations. The input data include the information about the kesterite crystal structure available in literature: CZTS and CZTSe crystallize in the body-centered tetragonal lattice. The full lattice optimization (namely volume and  $c/a$  ratio) as well as internal atomic relaxation were performed using the GGA PBEsol exchange correlational functional. The *experimental* values of the  $c/a$  ratio and the volume of the unit cell were derived from references [9]; Paier et al. [127] have used similar functionals for their calculations; and lastly, calculated  $c/a$  ratios and  $E_g$  using the *exciting* code together with two reference data are shown in Table 1:

*Table 1. Comparison of the experimentally and theoretically derived lattice parameters  $a$  and  $c$ , and the band gap value  $E_g$*

Calculated parameters	CZTS			CZTSe		
	Experimental reference [9]	Theoretical reference [127]	<i>Exciting</i> code calculations [A.Monoharan HU]	Experimental reference [9]	Theoretical reference [127]	<i>Exciting</i> code calculations [A.Monoharan HU]
$a$ (Å)	5.419	5.46	5.421	5.695	5.61	5.601
$c$ (Å)	10.854	10.929	10.787			
$E_g$ (eV)	1.5	1.487	DFT 0.45	1.0	-	DFT 0.06
			GW 1.34			GW 0.94

A good agreement is found between experimental reference data as well as with theoretical work of Paier et al. [127] and data calculated with *exciting* code. The lattice parameters  $a$  and  $c$  show a very good overlap with presented literature data.

e) pDOS of CZTS and CZTSe calculated using *exciting* code

The Fig.2 presents the TDOS and pDOS of the conduction band obtained for the CZTSe system using *exciting* code. Results obtained by A. Monoharan HU, Berlin.

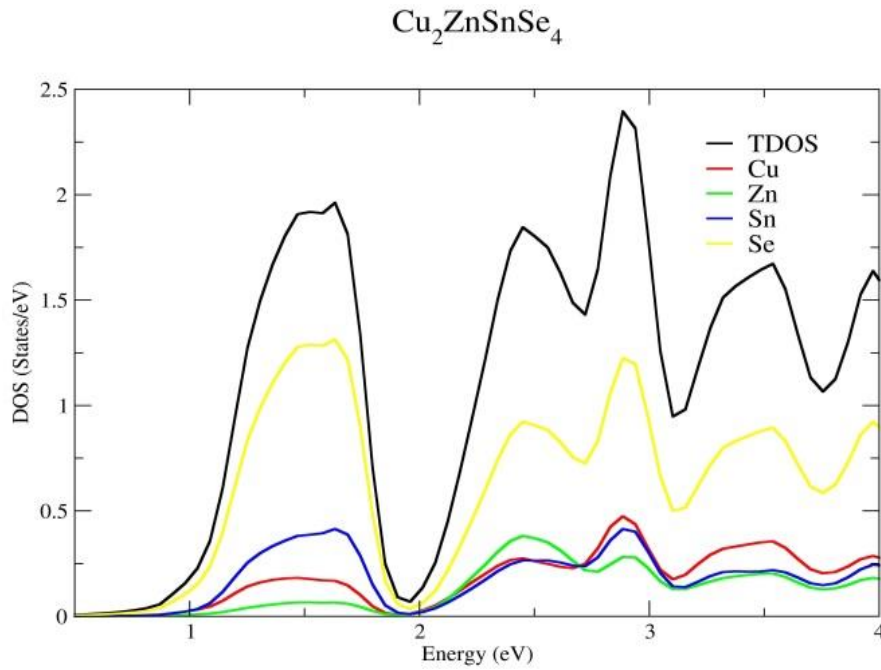


Fig.2. The TDOS and p-DOS of the  $\text{Cu}_2\text{ZnSnSe}_4$  calculated using the *exciting* code

The Cu d-states of the conduction band, which correspond to the Cu K-edge of CZTS and CZTSe, are shown in Fig.3.

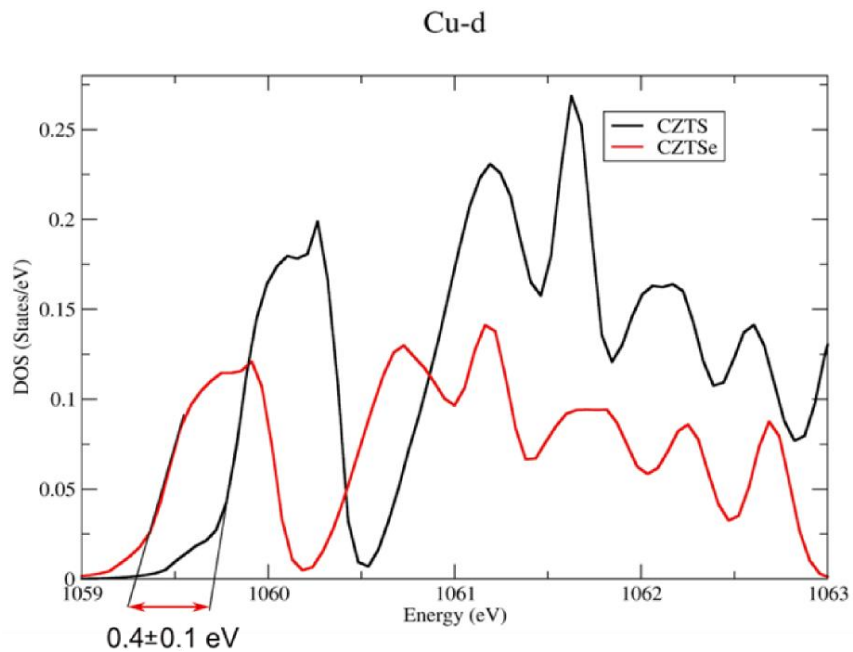


Fig.3. The Cu d-pDOS for the CZTS (black) and CZTSe (red)

## 11. CV

Tetiana Olar

- 1997-2007 secondary and high school №11 in Artemivsk, Ukraine
- 2007-2011 Bachelor degree in Molecular Physics  
Taras Shevchenko National University of Kyiv, Kiev, Ukraine
- 2011-2013 Master degree in Molecular Physics  
Taras Shevchenko National University of Kyiv, Kiev, Ukraine
- 2012-2013 Master degree “Master in Nanoscience”  
University of the Basque Country, San Sebastián- Donostia,  
Spain
- 2013-2017 PhD thesis  
Free University of Berlin/  
Helmholtz-Zentrum Berlin für Materialien und Energie GmbH  
Berlin, Germany



## 12. References

- [1]. W. Wang, M.T. Winkler, O. Gunawan, T. Gokmen, T.K. Todorov, Y. Zhu, D.B. Mitzi, “Device characteristics of CZTSSe thin film solar cells with 12.6% efficiency”, *Adv. Energy Mater.* 4 (2014).
- [2]. W. Shockley, H. J. Queisser, “Detailed Balance Limit of Efficiency of p-n Junction Solar Cells,” *J. Appl. Phys.*, vol. 32, no. 3, p. 510 (1961).
- [3]. M. Arasimowicz, “Phase segregation in  $\text{Cu}_2\text{ZnSnSe}_4$  thin films for photovoltaic applications. The effect of precursor microstructure and selenium activity during selenization of electrodeposited metallic precursors” PhD thesis, Luxembourg 2014.
- [4]. P. Jackson, R. Wuerz, D. Hariskos, E. Lotter, W. Witte, M. Powalla, “Effect of heavy alkali elements in  $\text{Cu}(\text{In,Ga})\text{Se}_2$  solar cells with efficiencies up to 22,6%” *Phys. Status Solidi RRL* **10**, No. 8, 583–586 (2016)
- [5]. J. Scragg, “Studies of  $\text{Cu}_2\text{ZnSnS}_4$  films prepared by sulfurization of electrodeposited precursors” PhD thesis, Bath 2010.
- [6]. Benjamin E. Johnson “The Role of Cd and Ga in the  $\text{Cu}(\text{In,Ga})\text{S}_2/\text{CdS}$  Heterojunction Studied with X-Ray Spectroscopic Methods”, PhD thesis, Berlin 2010
- [7]. Kestcells annex, <http://kestcells.eu/>
- [8]. S.G. Haass, M. Diethelm, M. Werner, B. Bissig, Y.E. Romanyuk, A.N. Tiwari “11.2% Efficient Solution Processed Kesterite Solar Cell with a Low Voltage Deficit” *Adv. Energy Mater.* Volume 5, Issue 18 (2015).
- [9]. S. Siebentritt, S. Schorr, “Kesterite- a challenging material for solar cells” *Prog. Photovolt: Res. Appl.* 20:512–519, (2012).
- [10]. “Copper Zinc Tin Sulfide-Based Thin-Film Solar Cells”, First Edition. Edited by K. Ito. Chapter 3 by S.Schorr. 2015 John Wiley & Sons, Ltd. Published 2015 by John Wiley & Sons, Ltd.
- [11]. Schorr S. “The crystal structure of kesterite type compounds: a neutron and X-ray diffraction study” *Solar Energy Materials and Solar Cells*; 95: 1482 (2011).
- [12]. A. Redinger, D.M. Berg, P.J. Dale, R. Djemour, L. Gütay, T. Eisenbarth, N. Valle, S. Siebentritt. „Route towards high efficiency single phase  $\text{Cu}_2\text{ZnSn}(\text{S,Se})_4$  thin film solar cells: model experiments and literature review” *Journal of Photovoltaics*, VOL. 1, NO. 2. (2011)
- [13]. D. Mitzi, O. Gunawan, T. Todorov, K. Wang, S. Guha. “The path towards a high-performance solution processed kesterite solar cell”. *Solar Energy Materials & Solar Cells*, 95: 1421, (2011).
- [14]. S. Schorr, H.J. Hoebler, M. Tovar. “A neutron diffraction study of the stannite-kesterite solid solution series” *European Journal Of Mineralogy*; 19: 65, (2007).
- [15]. T.M. Friedlmeier, N. Wieser, T. Walter, H. Dittrich, H.W. Schock. In 14th European Photovoltaic Solar Energy Conference (Stephens and Asc., Barcelona, 1997), Vol. 1, p. 1242.
- [16]. S. Ahn, S. Jung, J. Gwak, A. Cho, K. Shin, K. Yoon, D. Park, H. Cheong, J.H. Yun. “Determination of band gap energy (E-g) of  $\text{Cu}_2\text{ZnSnSe}_4$  thin films: on the discrepancies of reported band gap values”. *Applied Physics Letters*; 97: 021905, (2010).
- [17]. J.M. Raulot, C. Domain, J.F. Guillemoles. “Ab initio investigation of potential indium and gallium free chalcopyrite compounds for photovoltaic application” *Journal of Physics and Chemistry of Solids*; 66: 2019, (2005).

- [18]. S. Chen, X.G. Gong, A. Walsh, S-H. Wei. "Crystal and electronic band structure of  $\text{Cu}_2\text{ZnSnX}_4$  (X=S and Se) photovoltaic absorbers: first-principles insights". *Applied Physics Letters*; 94: 041903, (2009).
- [19]. S. Botti, D. Kammerlander, MAL. Marques. "Band structures of  $\text{Cu}_2\text{ZnSnS}_4$  and  $\text{Cu}_2\text{ZnSnSe}_4$  from many-body methods". *Applied Physics Letters*; 98: 241915, (2011).
- [20]. S. Chen, A. Walsh, X.-G. Gong, S.-H. Wei "Classification of Lattice Defects in the Kesterite  $\text{Cu}_2\text{ZnSnS}_4$  and  $\text{Cu}_2\text{ZnSnSe}_4$  Earth- Abundant Solar Cell Absorbers" *Adv. Mater.*, 25, 1522-1539. (2013)
- [21]. S.Chen,X.G. Gong, A. Walsh, S.-H. Wei, "Defect Physics of the Kesterite Thin-Film Solar Cell Absorber  $\text{Cu}_2\text{ZnSnS}_4$ " *Appl. Phys. Lett.*, 96, 021902-021902-3, (2010).
- [22]. I.D. Olekseyuk, I.V. Dudchak, L.V. Piskach, "Phase Equilibria in the  $\text{Cu}_2\text{S-ZnS-SnS}_2$  System" *J. Alloys Compd.*, 368, 135-143, (2004).
- [23]. T. Gödecke, T. Haalboom, F. Ernst. „Phase equilibria of Cu-In-Se I: stable states and nonequilibrium states of the  $\text{In}_2\text{Se}_3\text{-Cu}_2\text{Se}$  subsystem" *Zeitschrift für Metallkunde*; 91: 622, (2000).
- [24]. U. Rau, J. Werner, *Appl. Phys. Lett.* 84, 3735, (2004).
- [25]. J.T. Watjen, J. Engman, M. Edoff, C. Platzer-Bjorkman, *Appl. Phys. Lett.* 100 (17) 173510, (2012).
- [26]. A. Redinger, M. Mousel, M.H. Wolter, N. Valle, S. Siebentritt, *Thin Solid Films* 535291, (2013).
- [27]. A. Fairbrother, E. García-hemme, V. Izquierdo-Roca, X. Fontané, F.A. Pilgarín-Agudelo, O. Vigil-Galán,; A. Pérez-Rodríguez, E. Saucedo "Development of a Selective Chemical Etch to Remove the Conversion Efficiency of Zn-Rich  $\text{Cu}_2\text{ZnSnS}_4$  Solar cells" *J. Am. Chem. Soc.* 134, 8018-8021, (2012).
- [28]. H. Xie, Y. Sánchez, S. López-Marino, M. Espíndola-Rodríguez, M. Neuschitzer, D. Sylla, A. Fairbrother, V. Izquierdo-Roca, A. Pérez-Rodríguez, and E. Saucedo "Impact of Sn(S,Se) Secondary Phases in  $\text{Cu}_2\text{ZnSn(S,Se)}_4$  Solar Cells: a Chemical Route for Their Selective Removal and Absorber Surface Passivation" *Applied Materials and Interfaces* dx.doi.org/10.1021/am502609c, (2014).
- [29]. S. Lopez-Marino, Y. Sanchez, M. Placidi, A. Fairbrother, M. Espindola-Rodriguez, X. Fontane, V. Izquierdo-Roca, J. Lopez-Garcia, L. Calvo-Barrio, A. Perez-Rodriguez, E. Saucedo "ZnSe Etching of Zn-rich  $\text{Cu}_2\text{ZnSnSe}_4$ : an oxidation route for improved solar-cell efficiency" *Chem. A Eur. J.* 19 (44), 14814–14822, (2013)
- [30]. ZSW thin-film solar cell reaches 20.1% efficiency. 4th May 2010 [cited 27th May 2010; Available from: <http://www.renewableenergyfocus.com/view/9182/zsw-thin-film-solar-cell-reaches-201-efficiency/>
- [31]. A. Fairbrother, X. Fontané, V. Izquierdo-Roca, M. Espindola-Rodriguez, S. López-Marino, M. Placidi, Juan López-García, A. Pérez-Rodríguez, E. Saucedo "Single-Step Sulfo-Selenization Method to Synthesize  $\text{Cu}_2\text{ZnSn(S}_y\text{Se}_{1-y})_4$  Absorbers from Metallic Stack Precursors" *ChemPhysChem.* 14, 1836-1843, (2013).
- [32]. H. Xie, M. Dimitrievska, X. Fontané, Y. Sánchez, S. López-Marino, V. Izquierdo-Roca, V. Bermúdez, A. Pérez-Rodríguez, E. Saucedo "Formation and impact of secondary phases in Cu-poor Zn-rich  $\text{Cu}_2\text{ZnSn(S}_{1-y}\text{Se}_y)_4$  ( $0 \leq y \leq 1$ ) based solar cells" *Solar Energy Materials & Solar Cells.* 140, 289–298. (2015).
- [33]. C. Platzer-Björkman, J. Scragg, H. Flammersberger, T. Kubart, M. Edoff "Influence of Precursor Sulfur Content on Film Formation and Compositional Changes in  $\text{Cu}_2\text{ZnSnS}_4$  Films and Solar Cells" *Sol. Energy Mater. Sol. Cells* 98, 110-117 (2012).

- [34]. J. Scragg, P.J. Dale, D. Colombara, L.M. Peter. "Thermodynamic Aspects of the Synthesis of thin-Film Materials for Solar Cells" *ChemPhysChem* 13, 3035-3046, (2012).
- [35]. G. Marcano, C. Rincón, L. M. de Chalraud, D. B. Bracho, G. S. Pérez "Crystal Growth and Structure, Electrical, and Optical Characterization of the Semiconductor  $\text{Cu}_2\text{SnSe}_3$ " *J. Appl. Phys.*, 90, 1847 (2001).
- [36]. <https://en.wikipedia.org/wiki/P%E2%80%93junction>
- [37]. K.F. Brennan "Introduction to Semiconductor Devices: For Computing and Telecommunications Applications" Cambridge University Press 2005.
- [38]. [https://en.wikipedia.org/wiki/Band\\_bending](https://en.wikipedia.org/wiki/Band_bending)
- [39]. [http://www.electronics-tutorials.ws/diode/diode\\_3.html](http://www.electronics-tutorials.ws/diode/diode_3.html)
- [40]. [https://en.wikipedia.org/wiki/Current%E2%80%93voltage\\_characteristic](https://en.wikipedia.org/wiki/Current%E2%80%93voltage_characteristic)
- [41]. U.Mishra, J. Singh "Semiconductor Device Physics and Design", Springer Science & Buisness Media(2007).
- [42]. R. L. Anderson „Germanium-gallium arsenide heterojunction" *IBM J. Res. Dev.* 4(3), pp. 283–287 (1960).
- [43]. R. Dingle, W. Wiegmann, and e. H. Henry, *Phys. Rev. Lett.* 33, 827 (1974).
- [44]. S.H. Wei and Alex Zunger, *Phys. Rev. Lett.* 59. 144 (1987), and references therein.
- [45]. D. G. Kilday and G. Margaritondo "Common-anion rule and its limits: Photoemission studies of  $\text{CuIn}_x\text{Ga}_{1-x}\text{Se}_2$ -Ge and  $\text{Cu}_x\text{Ag}_{1-x}\text{InSe}_2$ -Ge interfaces" *Phys. Rev. B*. Vol 36, N 17 (1987).
- [46]. J. Tersoff, "Theory of semiconductor heterojunctions: The role of quantum dipoles" *Phys. Rev. B*, 30, 4874-4877 (1984).
- [47]. N. Debbar, D. Biswas, P. Bhattacharya "Conduction-band offsets in pseudomorphic  $\text{In}_x\text{Ga}_{1-x}\text{As}/\text{Al}_{0.2}\text{Ga}_{0.8}\text{As}$  quantum wells ( $0.07 \leq x \leq 0.18$ ) measured by deep-level transient spectroscopy". *Physical Review B* 40 (2): 1058. (1989). [Bibcode:1989PhRvB.40.1058D. doi:10.1103/PhysRevB.40.1058.](https://doi.org/10.1103/PhysRevB.40.1058)
- [48]. <http://pveducation.org/pvc/drom/solar-cell-structure>
- [49]. S. Bourdais, C. Choné, B. Delatouche, A. Jacob, G. Larramona, C. Moisan, A. Lafond, F. Donatini, G. Rey, S. Siebentritt, A. Walsh and G. Dennler. "Is the Cu/Zn Disorder the Main Culprit for the Voltage Deficit in Kesterite Solar Cells?" *Adv. Energy Mater.*, 6, 1502276. (2016).
- [50]. L. Risch, L. Vauche, A. Redinger, M. Dimitrievska, Y. Sánchez, E. Saucedo, T. Unold, T. Goislard, C.M. Ruiz, L. Escoubas, J.J. Simon "Overcoming the Voc limitation of CZTSe solar cells", 978-1-5090-2724-8 , IEEE PVSC(2016).
- [51]. [https://en.wikipedia.org/wiki/Air\\_mass\\_coefficient](https://en.wikipedia.org/wiki/Air_mass_coefficient)
- [52]. M. Neuschitzer, Y. Sanchez, S. Lopez-Marino et al. "Optimization of CdS buffer layer for high-performance  $\text{Cu}_2\text{ZnSnSe}_4$  solar cells and the effects of light soaking: elimination of crossover and red kink" *Prog in Phot* Vol: 23 Issue: 11 Pages: 1660-1667 (2015).
- [53]. M. Bär, B.-A. Schubert, B. Marsen, R. G. Wilks, S. Pookpanratana, M. Blum T. Unold, S. Krause, W. Yang, L. Weinhardt, C. Heske, and H.-W. Schock "Cliff-like conduction band offset and KCN-induced recombination barrier enhancement at the  $\text{CdS}/\text{Cu}_2\text{ZnSnS}_4$  thin-film solar cell heterojunction" *Appl. Phys. Lett.* 99, 222105 (2011).
- [54]. A. Santoni, F. Biccari, C. Malerba, M. Valentini, R. Chierchia, and A. Mittiga "Valence band offset at the  $\text{CdS}/\text{Cu}_2\text{ZnSnS}_4$  interface probed by X-ray photoelectron spectroscopy" *J. Phys. D: Appl. Phys.* 46 175101, doi:10.1088/0022-3727/46/17/175101, (2013).

- [55]. R. Haight, A. Barkhouse, O. Gunawan, B. Shin, M. Copel, M. Hopstaken, and D. B. Mitzi “Band alignment at the  $\text{Cu}_2\text{ZnSn}(\text{S}_x\text{Se}_{1-x})_4$  /CdS interface” *APPLIED PHYSICS LETTERS* 98, 253502 (2011).
- [56]. S. Tajima, K. Kataoka, N. Takahashi, Y. Kimoto, T. Fukano, M. Hasegawa, and H. Hazama “Direct measurement of band offset at the interface between CdS and  $\text{Cu}_2\text{ZnSnS}_4$  using hard X-ray photoelectron spectroscopy” *APPLIED PHYSICS LETTERS* 103, 243906 (2013).
- [57]. T. Kato, H. Hiroi, N. Sakai, S. Muraoka, H. Sugimoto “Characterization of Front and Back Interfaces on  $\text{Cu}_2\text{ZnSnS}_4$  Thin-Film Solar Cells” Proc. 27<sup>th</sup> Eur. Photovolt. Sol. Energy Conf. Exhib. 2236-2239 (2012).
- [58]. I. Repins, N. Vora, C. Beall, S. Wei, Y. Yan, M. Romero, G. Teeter, H. Du, B. To, M. Young, and R. Noufi, “Kesterites and Chalcopyrites: A Comparison of Close Cousins” Preprint: Presented at the 2011 Materials Research Society Spring Meeting San Francisco, California (2011).
- [59]. S. Chen, A. Walsh, J.H. Yang, X.G. Gong, L. Sun, P.X. Yang, J.H. Chu, and S.H. Wei “Compositional dependence of structural and electronic properties of  $\text{Cu}_2\text{ZnSn}(\text{S},\text{Se})_4$  alloys for thin film solar cells” *Phys. Rev. B* 83, 125201 (2011).
- [60]. D.S. Su, S.H. Wei, *Appl. Phys. Lett.* 74(17), 2483-2485 (1999).
- [61]. H. Hertz, *Ann. Physik* 31,983 (1887)
- [62]. A. Einstein, *Annalen der Physik* Vol. 17, 132 (1905)
- [63]. V.Parvan, A. Mizrak, B. Ümsur, W. Calvet, A. Steigert, I. Lauer mann, T. Ditrich, D. Greiner, C.A. Kaufmann, and R. Schlattmann „ Impact of post-deposition treatment of CIGSe-absorbers with KF, NaF and Na using SPV and XPS/UPS“ E-MRS Lille, France (2016).
- [64]. C.C.Chusuei, D.W.Goodman “X-ray Photoelectron Spectroscopy“ Encyclopedia of Physical Science and Technology, Third edition, Vol 17, Texas A&M University.
- [65]. Robert Tschöke, Master Thesis
- [66]. J.H. Scofield, “HARTREE-SLATER SUBSHELL PHOTOIONIZATION CROSS-SECTIONS”
- [67]. M.B. Trzhaskovskaya, V.K. Nikulin, V.I. Nefedov, V.G. Yarzhemsky “Non-dipole second order parameters of the photoelectron angular distribution for elements  $Z=1-100$  in the photoelectron energy range 1–10 keV” *Atomic Data and Nuclear Data Tables*; 92:245 (2006).
- [68]. J.J. Yeh et al., *Atomic Data and Nuclear Data Tables*, **32**, 1 (1985)
- [69]. R.F. Reilmann et al., *J. Electron Spectrosc. Relat. Phenom.*, **8**, 389 (1976)
- [70]. <http://www.quases.com/>
- [71]. <http://hyperphysics.phy-astr.gsu.edu/hbase/quantum/fermi.html>
- [72]. P. S. Bechthold „X-ray Absorption Spectroscopy”, Institut für Festkörperforschung Forschungszentrum Jülich GmbH (1998).
- [73]. B. Johnson, J. Klaer, S. Merdes, M. Gorgoi, B. Höpfner, A. Vollmer, I. Lauer mann „Limitations of Near Edge X-ray Absorption Fine Structure as a tool for observing conduction bands in chalcopyrite solar cell heterojunctions” *J. Electron Spectrosc. Relat. Phenom.* 190, 42–46 (2013).
- [74]. S. Calvin “XAFS for Everyone” CRC Press (2013).
- [75]. Granata, J. E.; Sites, J. R.; Asher, S.; Matson, R. [Quantitative Incorporation of Sodium in  \$\text{CuInSe}\_2\$  and  \$\text{Cu}\(\text{In,Ga}\)\text{Se}\_2\$  Photovoltaic Devices](#), IEEE Photovoltaic Spec. Conf., 26th 1997, 387–390.
- [76]. F. Pianezzi, P. Reinhard, A. Chirila, B. Bissig, S. Nishiwaki, S. Buecheler, A. Tiwari, N. Unveiling “The Effects of Post-Deposition Treatment with Different Alkaline Elements on

- the Electronic Properties of CIGS Thin Film Solar Cells”*Phys. Chem. Chem. Phys.* 16, 8843-8851 (2014).
- [77]. H. Xie, S. López-Marino, T. Olar, Y. Sánchez, M. Neuschitzer, F. Oliva, S. Giraldo, V. Izquierdo-Roca, I. Lauermann, A. Pérez-Rodríguez, and E. Saucedo “Impact of Na Dynamics at the  $\text{Cu}_2\text{ZnSn}(\text{S,Se})_4/\text{CdS}$  Interface During Post Low Temperature Treatment of Absorbers”*Appl. Mater. Interfaces* 8, 5017–5024 (2016).
- [78]. M. Baer, B.A. Schubert, B. Marsen, S. Krause, S. Pookpanratana, T. Unold, L. Weinhardt, C. Heske, and H.W. Schock *Appl. Phys. Lett.* 99, 152111 (2011).
- [79]. I. Lauermann, Ch. Loreck, A. Grimm, R. Klenk, H. Mönig, M.Ch. Lux-Steiner, Ch.-H. Fischer, S. Visbeck, T.P. Niesen. “Cu-accumulation at the interface between sputter- $(\text{Zn,Mg})\text{O}$  and  $\text{Cu}(\text{In,Ga})(\text{S,Se})_2$  — A key to understanding the need for buffer layers?”*Thin Solid Films* 515, 6015-6019 (2007).
- [80]. J. Lehmann, S. Lehmann, I. Lauermann, T. Rissom, C. A. Kaufmann, M. Ch. Lux-Steiner, M. Bär, and S. Sadewasser “Reliable wet-chemical cleaning of natively oxidized high-efficiency  $\text{Cu}(\text{In,Ga})\text{Se}_2$  thin-film solar cell absorbers”*Journal of Applied Physics* 116, 233502 (2014).
- [81]. D. Schmid, M. Ruckh, F. Grunwald, H.W. Schock “Chalcopyrite/defect chalcopyrite heterojunctions on the basis of  $\text{CuInSe}_2$ ”*J Appl Phys* 73:2902 (1993).
- [82]. S. Harel, C. Guillot-Deudon, L. Choubac, J. Hamon, A. Lafond “Surface composition deviation of  $\text{Cu}_2\text{ZnSnS}_4$  derivative powdered samples”*Applied Surface Science* 303, 107–110, (2014).
- [83]. F. Schäfers, M. Mertin, M. Gorgoi “KMC-1: A high resolution and high flux soft X-ray beamline at BESSY”*Rev of Sci Instr* 78:123102 (2007).
- [84]. R. Klenk “Characterisation and modelling of chalcopyrite solar cells”*Thin Solid Films* 387, 135\_140 (2001).
- [85]. J. Li, M. Wei, Q. Du, W. Liu, G. Jiang, C. Zhu “The band alignment at  $\text{CdS}/\text{Cu}_2\text{ZnSnSe}_4$  heterojunction interface”*Surface and Interface Analysis* 45:682–684,(2013).
- [86]. S. Siebentritt, U. Rau, “Wide-Gap Chalcopyrites”, Springer-Verlag Berlin Heidelberg (2005).
- [87]. K. Sardashti, R. Haight, T. Gokmen, W. Wang, L.-Y. Chang, D. B. Mitzi, A. C. Kummel “Impact of Nanoscale Elemental Distribution in High-Performance Kesterite Solar Cells”*Adv. Energy Mater.*, 5, 1402180(2015).
- [88]. K. Wang,; O. Gunawan, T. Todorov, B. Shin, S. J. Chey, N. A. Bojarczuk, D. Mitzi, S. Guha “Thermally evaporated  $\text{Cu}_2\text{ZnSnS}_4$  Solar Cells”*Appl. Phys. Lett.* 97, 143508.(2010).
- [89]. S. Tajima, R. Asahi, D. Isheim, D. N. Seidman, T. Itoh, M. Hasegawa, K. Ohishi “Atom-Probe Tomographic Study of Interfaces of  $\text{Cu}_2\text{ZnSnS}_4$  Photovoltaic Cells”*Appl. Phys. Lett.* 105, 093901 (2014).
- [90]. C. Krämmer, C. Huber, C. Zimmermann, M. Lang, T. Schnabel, T. Abzieher, E. Ahlswede, H. Kalt, M. Hetterich “Reversible Order-Disorder Related Band Gap Changes in  $\text{Cu}_2\text{ZnSn}(\text{S,Se})_4$  via Post-Annealing of Solar Cells Measured by Electroreflectance”*Appl. Phys. Lett.* 105, 262104 (2014).
- [91]. G. Rey, A. Redinger, J. Sendler, T. P. Weiss, M. Thevenin, M. Guennou, B. El Adib, S. Siebentritt “The Band Gap of  $\text{Cu}_2\text{ZnSnSe}_4$ : Effect of Order-Disorder”*Appl. Phys. Lett.* 105, 112106 (2014).

- [92]. C. Krämmer, C. Huber, T. Schnabel, C. Zimmermann, M. Lang, E. Ahlswede, H. Kalt, M. Hetterich “Order-Disorder Related Band Gap Changes in  $\text{Cu}_2\text{ZnSn}(\text{S},\text{Se})_4$ : Impact on Solar Cell Performance” presented in 42nd IEEE Photovoltaic Specialists Conference, June 14-19, 2015, New Orleans.
- [93]. M. Neuschitzer, Y. Sanchez, T. Olar, T. Thersleff, S. Lopez-Marino, F. Oliva, M. Espindola-Rodriguez, H. Xie, M. Placidi, V. Izquierdo-Roca, I. Lauer mann, K. Leifer, A. Pérez-Rodriguez, E. Saucedo “Complex Surface Chemistry of Kesterites: Cu/Zn Reordering after Low Temperature Postdeposition Annealing and Its Role in High Performance Devices” *Chem. Mater.* 27, 5279-5287(2015).
- [94]. I. L. Repins, J. V. Li, A. Kanevce, C. L. Perkins, K. X. Steirer, J. Pankow, G. Teeter, D. Kuciauskas, C. Beall, C. Dehart, J. Carapella, B. Bob, J. S. Park, S. H. Wei “Effects of Deposition Termination on  $\text{Cu}_2\text{ZnSnSe}_4$  Device Characteristics” *Thin Solid Films* 582, 184-187 (2015).
- [95]. A. Niemegeers, M. Burgelman, Vos AD. “On the  $\text{CdS}/\text{CuInSe}_2$  conduction band discontinuity” *Applied Physics Letters*; 67: 843–845 (1995).
- [96]. M.P. Seah, W.A. Dench, *Surf. Interface Anal.* 1, 2-11 (1997).
- [97]. L. E. Valle Rios, K. Neldner, G. Gurieva, S. Schorr "Existence of off-stoichiometric single phase kesterite" *Journal of Alloys and Compounds* 657, 408e413 (2016).
- [98]. A. Sandell, B. Sanyal, L.E. Walle, P. Uvdal, A. Borg, *J. Electron Spectrosc. Relat. Phenom.* 183, 1107–1113 (2011).
- [99]. M. Bär, B.-A. Schubert, B. Marsen, S. Schorr, R.G. Wilks, L. Weinhardt, S. Pookpanratana, M. Blum, S. Krause, Y. Zhang, W. Yang, T. Unold, C. Heske, H.-W. Schock, *Phys. Rev. B* 84, 035308 (2011).
- [100]. M. Bär, S. Nishiwaki, L. Weinhardt, S. Pookpanratana, O. Fuchs, M. Blum, W. Yang, J.D. Denlinger, W.N. Schafarman, C. Heske, *Appl. Phys. Lett.* 93, 244103 (2008).
- [101]. A.J. Berry, H.St.C. O’Niel, K.D. Jayasuriya, S.J. Campbell, G.J. Foran, *Am. Miner.* 88, 967–977 (2003).
- [102]. M.P. Paranthaman, W. Wong-Ng, R. N. Bhattacharya „Semiconductor Materials for Solar Photovoltaic Cells“, *Springer Series in Material Science*, 218 (2016).
- [103]. R. Bacewicz, A. Wolska, K. Lawniczak-Jablonska, Ph. Sainctavit, *J. Phys.: Condens.Matter*, 12, 7371-7379 (2000).
- [104]. M. Grioni, J.B. Goedkoop, R. Schoorl, F.M.F. de Groot, J.C. Fuggle, *Phys. Rev. B* 39, 1541-1545 (1989).
- [105]. C. Stephan, S. Schorr, H.W. Schock “New Structural Investigations in the  $\text{Cu}_2\text{Se}(\text{S})$ - $\text{In}_2\text{Se}(\text{S})$ (3)/ $\text{Cu}_2\text{Se}(\text{S})$ - $\text{Ga}_2\text{Se}(\text{S})$ (3) Phase Diagram” Materials Research Society Symposium Proceedings Vol 1165, 411-417(2010).
- [106]. W.G.Zeier, H. Zhu, Z.M.Gibbs, G.Ceder, W. Tremel, G.J.Snyder “Band convergence in the non-cubic chalcopyrite compounds  $\text{Cu}_2\text{MGeSe}_4$ ” *J. Mater. Chem. C*, 2, 10189 (2014).
- [107]. F. M. F. De Groot, *J. Electron Spectrosc. Relat. Phenom.* 62, 111, (1993).
- [108]. L. F. Mattheiss and R. E. Dietz, *Phys. Rev. B* 22, 1663 (1980).
- [109]. T. A. Tyson, K. O. Hodgson, C. R. Natoli, and M. Benfatto, *Phys.Rev. B* 46, 5997 (1992).
- [110]. Y. Joly “X-ray absorption near edge structure calculations beyond the muffin-tin approximation“ *Phys.Rev. B* 63, 125120 (2001).
- [111]. R. Sarmiento-Pérez, S. Botti, C. S. Schnohr, I. Lauer mann, A. Rubio, B. Johnson “Local versus global electronic properties of chalcopyrite alloys: X-ray absorption

- spectroscopy and ab initio calculations” *Journal of Applied Physics* 116, p. 093703/1-5 (2014).
- [112]. <http://exciting-code.org>
- [113]. <https://www.youtube.com/watch?v=jZi2EOrCpY>
- [114]. A. Gulans, S. Kontur, C. Meisenbichler, D. Nabok, P. Pavone, S. Rigamonti, S. Sagmeister, U. Werner and C. Draxl “exciting: a full-potential all-electron package implementing density-functional theory and many-body perturbation theory” *Journal of Physics: Condensed Matter*, Volume 26, Number 36 (2014).
- [115]. H. Jiang et al. *Computer Physics Communications* 184, 348–366 (2013).
- [116]. L. Hedin, *Phys. Rev.* 139, A796 (1965).
- [117]. L. Hedin, B.I. Lundqvist, *Solid State Phys.* 23,1 (1969).
- [118]. C.S. Wang, W.E. Pickett “Density-functional theory of excitation spectra of semiconductors: application to Si” *Phys. Rev. Lett.* 51, 597 600 (1983).
- [119]. O. Zakharov, A. Rubio, X. Blase, M.L. Cohen, S.G. Louie “Quasiparticle band structures of six II-VI compounds: ZnS, ZnSe, ZnTe, CdS, CdSe and CdTe” *Phys. Rev. B* 50 10 780e10 787 (1994).
- [120]. M. Rohlfing, P. Kruger, J. Pollmann “Quasiparticle band structure of CdS” *Phys. Rev. Lett.* 75, 3489e3492 (1995).
- [121]. N. Kheloufi, A. Bouzid *Journal of Alloys and Compounds* 671, 144-149 (2016).
- [122]. J. Vidal, S. Botti, P. Olsson, J.-F. Guillemoles, and L. Reining *Phys. Rev. Lett.* 104, 056401 (2010).
- [123]. S. Eckner, H. Kämmer, T. Steinbach, M. Gnauck, A. Johannes, C. Stephan, S. Schorr and C. S. Schnohr "Atomic-scale structure, cation distribution, and bandgap bowing in Cu(In,Ga)S<sub>2</sub> and Cu(In,Ga)Se<sub>2</sub>” *Appl. Phys. Lett.* 103, 081905 (2013).
- [124]. C. S. Schnohr, H. Kämmer, C. Stephan, S. Schorr, T. Steinbach, and J. Rensberg, *Phys. Rev. B* 85, 245204 (2012).
- [125]. G.K.H. Madsen, P. Blaha, K. Schwarz, E. Sjöstedt, L. Nordström “Efficient linearization of the augmented plane-wave method” *Phys. Rev. B*. Vol. 64, - P. 195134 (2001).
- [126]. <http://jp-minerals.org/vesta/en/>
- [127]. J. Paier, R. Asahi, A. Nagoya, G. Kresse *Phys. Rev. B* 79, 115126 (2009).
- [128]. E. U. Condon and G. H. Shortley “Theory of Atomic Spectra” Cambridge University Press, London, UK (1953).
- [129]. <http://www.intechopen.com/source/html/39068/media/image19.jpeg>
- [130]. <http://neel.cnrs.fr/spip.php?rubrique1007&lang=en>
- [131]. <http://hyperphysics.phy-astr.gsu.edu/hbase/solids/fermi.html>
- [132]. C. Platzer-Björkman “Band alignment between ZnO-based and Cu(In,Ga)Se<sub>2</sub> thin film for high efficiency solar cells” PhD thesis, Uppsala 2006.